Spring 2021

Damage Evolution and High-Rate Response of High-Strength Concrete under Triaxial Loading

Brett Williams
Southern Methodist University, brettanthonywilliams@gmail.com

Recommended Citation

Williams, Brett, "Damage Evolution and High-Rate Response of High-Strength Concrete under Triaxial Loading" (2021). *Mechanical Engineering Research Theses and Dissertations*. 35.
https://scholar.smu.edu/engineering_mechanical_etds/35

DAMAGE EVOLUTION AND HIGH-RATE RESPONSE OF HIGH-STRENGTH CONCRETE UNDER TRIAXIAL LOADING

Approved by:

____
Prof. Xu Nie
Associate Professor

____
Prof. Xin-Lin Gao
Professor

____
Dr. William Heard
U.S. Army ERDC

____
Prof. Brett Story
Associate Professor

____
Prof. Wei Tong
Professor

DAMAGE EVOLUTION AND HIGH-RATE RESPONSE
OF HIGH-STRENGTH CONCETE
UNDER TRIAXIAL LOADING

A Dissertation Presented to the Graduate Faculty of

Bobby B. Lyle School of Engineering

Southern Methodist University

in

Partial Fulfillment of the Requirements

for the degree of

Doctor of Philosophy

with a

Major in Mechanical Engineering

by

Brett Williams

B.S., Mechanical Engineering, Mississippi State University

M.S., Civil Engineering, Mississippi State University

May 15, 2021

ACKNOWLEDGMENTS

I owe a debt of gratitude to my advisor, Prof. Nie, and mentor, Dr. Heard, for their continual support throughout my pursuit of a Ph.D. I would also like to thank Jason Morson for his outstanding technical support throughout the duration of my dissertation research. I am thankful for the faculty in the Department of Mechanical Engineering at SMU and my many coworkers at the U.S. Army ERDC that supported my goals towards education, research, and technical writing. Lastly, I am blessed to have a family that prayed for me and continually made sacrifices so that I could pursue and complete my doctoral degree.

The use of trade, product, or firm names in this document is for descriptive purposes only and does not imply endorsement by the U.S. Government. The tests described and the resulting data presented herein, unless otherwise noted, are based upon work conducted by the U.S. Army ERDC supported under 61102/AB2 "Protection, Maneuver, Geospatial, Natural Sciences/ Fundamental Adaptive Protection and Projection Research." Permission was granted by the Director, Geotechnical and Structures Laboratory to publish this information. The findings of this report are not to be construed as an official Department of the Army position unless so designated by other authorized documents.

Williams, Brett B.S., Mechanical Engineering, Mississippi State University, 2009
M.S., Civil Engineering, Mississippi State University, 2015

Damage Evolution and High-Rate Response
of High-Strength Concrete
Under Triaxial Loading

Advisor: Professor Xu Nie

Doctor of Philosophy conferred May 15, 2021

Dissertation completed January 29, 2021

The research presented in this study focuses on understanding fundamental mechanisms that drive material response under dynamic loading conditions. The objectives of the research were to: (1) to understand damage initiation and propagation in the bulk geomaterial under a variety of loading conditions and (2) to systematically investigate the strain rate effects on the triaxial compressive response of cementitious materials through the development of an innovative, first of its kind large-diameter (50 mm) triaxial Kolsky bar system.

The triaxial compressive response of high-strength concrete is needed to understand pressure-dependent material behavior, which is important for modeling extreme loading events. However, non-destructive damage analysis and dynamic triaxial experiments require specimens that are smaller than those typically used for model calibration. Reducing the specimen diameter from 50 mm to 25 mm showed negligible differences in the material response of a high-strength concrete (no coarse aggregate). However, a scalar correction factor is proposed to account for reductions in length-to-diameter ratio (L/D). By isolating size effects, results from experiments with scaled specimens can be implemented for model calibration efforts.

This study also investigates how cracking and pore collapse in high-strength concrete develops under hydrostatic loading and triaxial loading with confinement pressures up to 200 MPa. The impact of changes in specimen length-to-diameter ratio on damage mode were also evaluated. For brittle failure modes, three-dimensional crack networks were segmented to determine damage distribution and the angles of primary failure planes. High-strength concrete specimens were scanned using X-ray microtomography in both the pristine and damaged conditions to quantify changes in porosity size distributions as a result of pore collapse and crushing. Additionally, damaged specimens were then evaluated for residual compression strength. It was observed that although peak stresses increase with reduced length-to-diameter ratios, the dominant failure modes are not substantially influenced.

Lastly, a triaxial Kolsky bar technique is provided to simultaneously investigate strain rate and pressure dependencies. A cylindrical specimen with diameter and length of 25.4 mm was investigated at quasi-static and dynamic strain rates with confining pressures up to 200 MPa. Annular pulse shapers were incorporated to ensure stress equilibrium under constant strain rate deformations. Furthermore, dynamic pressure variations were theoretically approximated and determined to be negligible. The dynamic increase factor was found to decrease as confining pressures increased. Additionally, a shift in the brittle-to-ductile transition point was also observed to show a more brittle failure mode under dynamic strain rates. Lastly, a dynamic failure surface is presented to illustrate the strain-rate and pressure dependencies of high-strength concrete.

TABLE OF CONTENTS

TABLE OF CONTENTS vii

LIST OF FIGURES xi

LIST OF TABLES xv

NOMENCLATURE xvii

CHAPTER 1: INTRODUCTION 1

1.1 Motivation 1

1.2 Modeling Limitations 2

1.3 Research Objectives 3

1.4 Material Selection 4

1.5 Outline 4

CHAPTER 2: SIZE EFFECTS 6

2.1 Introduction 6

2.2 Material and Methods 8

2.2.1 Material and Specimen Preparation 8

2.2.2 Triaxial Test Equipment and Instrumentation 10

2.2.3 Definitions for Strain and Stress Measurements 12

2.3 Results and Discussion 13
2.3.1 Baseline Triaxial Experiments 13
2.3.2 Effects of Specimen Size 15
2.3.3 Effects of Length-to-Diameter Ratio 18
2.3.4 Limitations of Experimental Setup 22
2.4 Conclusions 25
CHAPTER 3: DAMAGE EVOLUTION 28
3.1 Introduction 28
3.2 Materials and Methods 31
3.2.1 Material and Specimen Preparation 31
3.2.2 Quasi-static Hydrostatic and Triaxial Compression 32
3.2.3 Micro-computed Tomography 33
3.2.4 Image Segmentation 35
3.3 Results and Discussion 37
3.3.1 Triaxial Compression Data 37
3.3.2 Limitations of Volumetric Strain Measurements 40
3.3.3 Visual Observations from Micro-CT 42
3.3.4 Isolation of Crack Patterns for Brittle Failure Modes 47
3.3.5 Quantifying Damage for Ductile Failure Modes 52
3.3.6 Residual Strength Measurements 57

3.4 Conclusions 58

CHAPTER 4: HIGH-RATE RESPONSE 61

4.1 Introduction 61

4.2 Materials and Methods 64

4.2.1 Material 64

4.2.2 Specimen Preparation 64

4.2.3 Quasi-static Triaxial Compression 65

4.2.4 Unconfined Kolsky Bar 66

4.2.5 Triaxial Kolsky bar 67

4.3 Results and Discussion 72

4.3.1 Unconfined Dynamic Response 72

4.3.2 Confined Dynamic Response 73

4.3.2.1 Pulse Shaping 73

4.3.2.2 Triaxial Kolsky Bar Experiments 74

4.3.2.3 Dynamic Pressure Changes 79

4.3.3 Pressure-dependent Dynamic Increase Factor 85

4.3.4 Dynamic Failure Surface 88

4.4 Conclusions 90

CHAPTER 5: CONCLUSIONS 92

5.1 Conclusions 92

5.2 Future Work 94

5.3 Publications 95

BIBLIOGRAPHY 97

LIST OF FIGURES

Fig. 1: Stress-strain responses from quasi-static triaxial compression tests of Cor-Tuf with confining pressures ranging from 10-300 MPa [4] 2

Fig. 2: Cross-sectional image of BBR9 high-strength concrete 9

Fig. 3: Closeup view of sealed triaxial specimen (left) and specimen inside the instrumentation cage (right)...11

Fig. 4: Cross-sectional view of triaxial pressure chamber used to test concrete specimens [41] .11

Fig. 5: Triaxial response of concrete specimens with 50-mm diameter to observe material response in terms of principal stress difference (*q*) and axial strain (ε_a) at confining pressures of 10, 20, 50, 100, 200 and 300 MPa...13

Fig. 6: Triaxial stress paths and failure surface..14

Fig. 7: Triaxial response of concrete specimens with 50-mm and 25-mm diameters to observe size effects in terms of principal stress difference (*q*) and axial strain (ε_a) at confining pressures of 10, 50, 100, and 200 MPa 17

Fig. 8: Triaxial response of concrete specimens with 25-mm diameter and L/D of 2.0 and 0.5 ..18

Fig. 9: Triaxial response of 25-mm-diameter concrete specimens with L/D = 2.0 and 1.0 to observe size effects 20

Fig. 10: Triaxial response of 25-mm-diameter concrete specimens with correction factors from Table 4 applied to L/D = 1 specimens..22

Fig. 11: 25-mm x 50-mm specimens (top) and 25-mm x 25-mm specimens (bottom) under the following conditions (from left to right): pristine, 10 MPa, 50 MPa, 100 MPa, and 200 MPa 23

Fig. 12: Axial strain (ε_a) and radial strain (ε_r) measurements at confining pressures of 100 and 200 MPa....24

Fig. 13: Pristine vs. damaged specimens after 30% axial strain at 100 MPa (left) with corresponding microstructure for the pristine (top right) and damaged (bottom right) conditions 25

Fig. 14. Pristine cylindrical BBR9 high-strength concrete specimens with L/D = 2.0 (left) and L/D = 1.0 (right) 32

Fig. 15. X-ray projection image (left) and reconstructed cross-sectional image (right) 35

Fig. 16. DataViewer registration example for pristine (white) and damaged (brown) micro-CT scan data 36

Fig. 17. Hydrostatic loading and unloading for 25 mm x 50 mm specimens up to 200 MPa mean normal stress 38

Fig. 18. Material response in terms of axial (left) and volumetric (right) strains for 25 mm x 50 mm and 25 mm x 25 mm TXC specimens at 10 and 50 MPa confining pressure 38

Fig. 19. Material response in terms of axial (left) and volumetric (right) strains for 25 mm x 50 mm and 25 mm x 25 mm TXC specimens at 100 and 200 MPa....39

Fig. 20. Gauge indicated material response in terms of axial (left) and volumetric (right) strains for large deformations ($\varepsilon_a \cong 30\%$) 41

Fig. 21. Micro-CT imagery of concrete fracture patterns under unconfined compression....43

Fig. 22. Micro-CT imagery of damaged concrete after multi-axial loading 45

Fig. 23. Comparison of damaged geometry at high confinement pressures with increasing axial deformations 46

Fig. 24. Micro-CT imagery of TXC specimens with L/D = 1.0 47

Fig. 25. Crack segmentation for 10 MPa TXC specimens with L/D = 2.0 (top) and L/D = 1.0 (bottom) 48

Fig. 26. Fracture patterns for 10 MPa TXC specimens with L/D = 2.0 (top) and L/D = 1.0 (bottom 49

Fig. 27. Crack segmentation for 50 MPa TXC specimens with L/D = 2.0 (top) and L/D = 1.0 (bottom) 50

Fig. 28. Fracture patterns for 50 MPa TXC specimens with L/D = 2.0 (top) and L/D = 1.0 (bottom) 51

Fig. 29. Cross-sectional porosity percentages for 2D sections in terms of normalized axial position before and after ~15% (left) and ~30% (right) axial strain deformations 52

Fig. 30. Void analysis in terms of volume-equivalent sphere diameter before and after ~15% (left) and ~30% (right) axial strain deformations 54

Fig. 31. Void structure for pristine and damaged 100 MPa (left) and 200 MPa (right) TXC specimens after ~15% axial strain deformations 55

Fig. 32. Void structure for pristine and damaged 100 MPa (left) and 200 MPa (right) TXC specimens after ~30% axial strain deformations 56

Fig. 33: Schematic of the triaxial Kolsky bar with hydraulic confinement chambers [122]. 63

Fig. 34. Cylindrical BBR9 high-strength concrete specimen. 65

Fig. 35. Confinement chambers for applying fluid pressure in the radial (left) and axial (right) directions. 68

Fig. 36. An installed triaxial test specimen. 69

Fig. 37. Original test signal in the form of bar stress under 50 MPa confining pressure. 70

Fig. 38. Demonstration of stress equilibrium for tests under 10 MPa confining pressure. 71

Fig. 39. Unconfined dynamic compressive response of BBR9 and strain rate history 73

Fig. 40. Pulse shapers for confinement pressures of (left to right) 10 MPa, 50 MPa, 100 MPa, and 200 MPa. 74

Fig. 41. Kolsky bar strain rate histories at each confinement pressure. 77

Fig. 42. Stress-strain behavior at each confinement pressure. 78

Fig. 43. The corrected and uncorrected engineering strain histories from quasi-static triaxial compression (left) and specimen loading and deformation histories from quasi-static triaxial compression at confining pressure of 200 MPa (right). 81

Fig. 44. Volume change of the hydraulic fluid as a function of the specimen axial strain. 83

Fig. 45: The pressure change in the confinement chamber throughout the duration of the specimen deformation. 84

Fig. 46. Quasi-static (dashed lines) and dynamic (solid lines) response of BBR9 concrete under different confining pressure. 85

Fig. 47. Dynamic failure surface in terms of principal stress difference (*q*) and mean normal stress (*p*). 89

LIST OF TABLES

Table 1: Mixture proportions for BBR9 high-strength concrete 9

Table 2: Unconfined compressive strength for BBR9 specimens with varying diameter............16

Table 3: Unconfined compressive strength for BBR9 specimens with varying L/D 19

Table 4: Correction factors to account for changes in L/D..21

Table 5. Mixture proportions for BBR9 high-strength concrete. 31

Table 6. Volumetric strain readings from in situ gauges and ex situ micro-CT measurements for specimens loaded to $\varepsilon_a \cong 30\%$. 42

Table 7. Residual strength measurements...57

Table 8. Mixture proportions for BBR9 high-strength concrete 64

Table 9. Pulse shaper specifications. 74

Table 10. Summary of Kolsky bar experiments. 76

Table 11. The calculation of pressure change under different initial hydrostatic pressures.........84

Table 12. Quasi-static principal stress difference conversion. 86

Table 13. Pressure dependency of the DIF for BBR9. 87

To my wife and best friend, Laura Beth, and our four children:

Shelby, Titus, Jonah, and Bailey.

Proverbs 3:5-6

NOMENCLATURE

A_b	Bar cross-sectional area
A_s	Specimen cross-sectional area
C_b	Elastic wave speed in the bar material
L_s	Initial specimen length
L/D	Length-to-diameter ratio
E_b	Young's modulus of the bar material
$\dot{\varepsilon}$	Specimen strain-rate
ε	Specimen strain
ε_a	Axial strain
ε_I	Reflected strain wave
ε_r	Radial train
ε_R	Reflected strain wave
ε_T	Transmitted strain wave
ε_v	Volumetric strain
p	Mean normal stress
q	Principal stress difference
σ	Specimen stress
σ_1	Stress on the incident bar side of the specimen
σ_2	Stress on the transmission bar side of the specimen
σ_a	Axial stress
σ_r	Radial stress
t	Time
v_1	Incident bar end velocity
v_2	Transmission bar end velocity

CHAPTER 1:

INTRODUCTION

The U. S. Army Engineer Research and Development Center (ERDC) is a leading research and development (R&D) organization in developing, characterizing and predicting the response of geomaterials subjected to weapon's effects [1-4]. The ERDC sponsored this research effort to develop quantitative experiments that will inform both damage and rate parameters that support the modeling and simulation (M&S) community.

1.1 Motivation

The experimental techniques developed through this research provide significant insight into material response and morphology under extreme loading conditions. The aim of this research is to provide the M&S community with an experimental basis for determining rate and damage parameters for use in concrete constitutive models. Although these parameters have been defined under simple loading conditions, damage progression and rate effects are not well understood for materials under triaxial loading conditions that occur during ballistic events. ERDC applied research programs (Integrated Force Protection Against Advanced Threats, Material Modeling for Force Protection, Defeat of Complex Attacks, Hardened Installation Protection for Persistent Operations) have all encountered this same fundamental gap in knowledge for understanding and predicting the physical mechanisms that drive material response and failure under complex stress states. This research intends to narrow this knowledge gap by providing unique experimental data that supports the ERDC's M&S capabilities, enhances the development of new advanced materials, and further establishes the ERDC as a leading authority in the geomaterials community.

1.2 Modeling Limitations

Continuum models for cementitious materials [1-3,5] are extensively used in explicit hydrocodes [6,7] to predict material behavior under penetration events. However, these models are fitted to materials based on limited material property data. As an example, analysts currently rely on "tuning" a specific model for a particular objective. However, in many cases these tuned models often have difficulty in simulating material behaviors that are observed in simple laboratory experiments [8].

To date, the primary experimental technique for providing the properties of geomaterials is the quasi-static triaxial testing apparatus involving a universal testing machine and a confinement pressure chamber. This system has been successfully applied to the testing of Cor-Tuf [4] and many other high-strength concretes. As shown in **Fig. 1**, the stress-strain behavior of cementitious material varies greatly as a function of confining pressure.

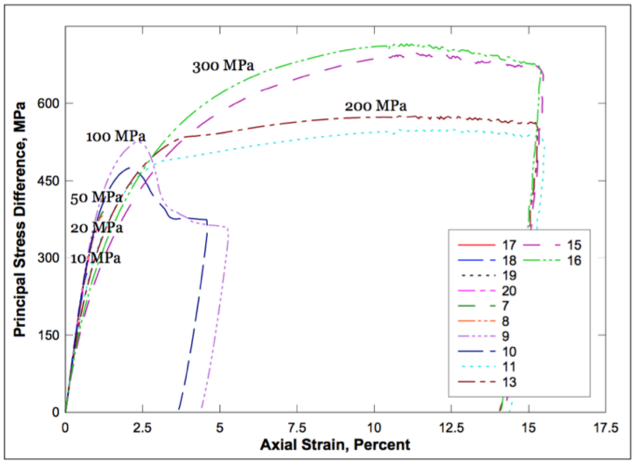

Fig. 1: Stress-strain responses from quasi-static triaxial compression tests of Cor-Tuf with confining pressures ranging from 10-300 MPa [4]

Although baseline triaxial experiments provide a firm foundation for model development, there are additional material behaviors that cannot be solely defined by the quasi-static triaxial technique. Two gaps identified in the current material property dataset include quantification of damage evolution and the dynamic behavior of materials under multiaxial stress states. Further understanding of material behavior under triaxial loading conditions will provide crucial information for the development of constitutive and numerical models used to simulate the response of structures in hostile environments.

1.3 Research Objectives

This research effort focuses on understanding the fundamental mechanisms that drive material response under triaxial loading conditions. The objectives of the proposed study were: (1) to understand the relationship between damage initiation and propagation as compared to constitutive property behavior in the bulk concrete under a variety of loading conditions and (2) to systematically investigate the strain rate effects on the triaxial compressive response of cementitious materials through the development of an innovative, first of its kind large-diameter (50 mm) triaxial Kolsky bar system. This effort developed a novel high-pressure triaxial testing instrument for high-strain-rate experimental studies. Hypotheses included (1) that as lateral confining pressure increases up to a maximum of 200 MPa, material behavior at high strain rates would become more ductile as a result of modification in microstructural damage mechanisms, and (2) that the transition points between brittle and ductile behavior would occur at a lower stress level when tested at high strain rates due to inertial effects and the rate sensitivity of kinematically driven fracture processes. To the best of the author's knowledge, there is no experimental evidence either supporting or denying these hypotheses related to high-strength concrete. The results from this research aimed to provide: (1) high-resolution visualization of damage morphology of cementitious materials at different levels of triaxial compression (TXC) under quasi-static (QS) conditions, and (2) the quantification of strain rate effects at different levels of triaxial loading under dynamic conditions.

1.4 Material Selection

Although the experimental techniques in this research could be applied to many brittle materials, the development of these techniques required the selection of one material that would be of particular interest to the Department of Defense and the ERDC. The ERDC's expertise in brittle geomaterials has a strong focus on high-strength and ultra-high-performance concretes (HSC and UHPC). The author recently co-developed an HSC known as BBR9, which stands for Baseline Basic Research – Mixture 9. Experimental data for this particular material can be openly published (not the case for many DoD materials), and the results provide insight to support ERDC's direct and reimbursable research programs. Additional details on the development and mixture proportioning for BBR9 are provided in section **2.2.1**.

1.5 Outline

The first chapter is devoted to providing background information describing the motivation and potential impact of the intended research area. Further background information for each specific research area is included as an introduction section in Chapters 2-4.

The focus of Chapter 2 is to determine the size effects associated with triaxial testing. In order to adequately characterize triaxial damage mechanisms and dynamic triaxial material properties, non-standard specimen geometries were required. As a foundational step, the influence of changes in diameter and aspect ratio must be understood before proceeding with the use of non-standard specimen geometries.

In Chapter 3, triaxial damage mechanisms are investigated using micro-CT to non-destructively record three-dimensional changes in morphology by comparing pristine and damaged specimens exposed to a variety of complex stress states. Crack isolations techniques were utilized for brittle failure modes while pore collapse was quantified for ductile failure modes.

The fourth chapter is focused on measuring dynamic triaxial properties. A large-diameter triaxial Kolsky bar was utilize to provide a hydrostatic preload of up to 200 MPa prior to sending a dynamic stress wave to record high-rate material properties under triaxial loads. Dynamic increase factors were calculated as a function of confining pressure to provide insight toward the development of a dynamic failure surface.

Finally, Chapter 5 provides an overarching summary related to the content discussed in Chapters 1-4. Additionally, a list of published, submitted, and planned publications are provided.

CHAPTER 2:

SIZE EFFECTS

2.1 Introduction

Worldwide, concrete is the second most consumed material after water with nearly 25 billion tons produced annually [9]. The American Concrete Institute (ACI) recently published an emerging technology report [10] defining Ultra-High-Performance Concrete (UHPC) as a cementitious material with a minimum unconfined compressive strength of 150 MPa, according to ASTM C39 [11]. The material in this study will be referred to as high-strength concrete even though it falls slightly below the 150 MPa threshold. However, it should be noted that concrete strength is not an absolute property but is dependent on the specimen shape, size, end preparation, and loading methods [12].

Although unconfined compressive strength has been well documented for specimen diameters of 46-144 mm and length-to-diameter ratios (L/Ds) ranging from 0.5 to 2.0 [13-16], it remains questionable that these strength correction factors will be valid under complex stress states. The effects of changes in specimen diameter and L/D have not been thoroughly investigated for concretes subjected to triaxial compressive loads. Under hydrostatic pressure and subsequent triaxial loading, concrete behavior deviates from a brittle failure mode and transitions to quasi-brittle and ductile failure regimes as a function of the applied confining pressure [4].

Quasi-static triaxial experiments on concrete are similar to those that have been documented for soils [17] but with substantially higher confining pressures . Initial triaxial experiments on concretes were pioneered by Balmer [18]. Over the years, extensive work has been conducted to determine the triaxial properties of concrete [19-27] . Some alternative methods utilize cubes that can be loaded independently in the three principal directions [28]. Others have induced complex stress states using a rigid ring to conduct quasi-oedometric compression tests that reveal the evolution of strength for concretes undergoing a complex loading path [29]. However, the most common method for model calibration uses a sealed specimen within a steel chamber that provides active confinement controls using fluid pressure. In this method, a cylindrical specimen is sealed with a membrane (butyl, latex, and/or neoprene) to prevent leakage. Then, a hydraulic fluid fills the chamber and is pressurized to apply the desired hydrostatic loading phase. While confining pressure is maintained ($\sigma_1 = \sigma_2$), the loading piston is activated to apply a deviatoric stress in the axial direction (σ_3). By using fluid pressure, frictional effects are eliminated in the radial direction.

Most model calibration efforts have utilized specimen sizes with a diameter of 50 mm or greater and L/D of ~2. Triaxial testing has been conducted at the U.S. Army Engineer Research and Development Center (ERDC) for decades [30] on concrete materials, primarily using a cored specimen with a diameter of 50 mm and a height of 100-115 mm at confining pressures up to 400 MPa [4,31,32]. Many previous studies have also been published using the GIGA facility in France to test concrete specimens that are 70 mm in diameter and 140 mm in height with confining pressures up to 850 MPa [27]. Sandia's Geomechanics department also houses triaxial testing capabilities for testing specimens with a diameter of 38 mm and a height of 76 mm at confining pressures up to 600 MPa and specimens with a diameter of 25 mm and a height of 50 mm at confining pressures up to 1 GPa [33]. However, most of the experimental data from Sandia have focused on rock specimens rather than concrete. Although larger specimens are considered to be more representative of the bulk material, dynamic triaxial tests often require specimens to be on the order of 19 mm in diameter with L/D = 1 [34]. Thus, a knowledge gap exists to correlate data recorded from quasi-static and dynamic triaxial experiments where diameter and L/D may vary substantially.

The objectives of this study are (1) to determine the suitability of reduced diameter (25-mm) specimens for observing bulk triaxial properties of high-strength concrete and (2) to determine the effects of changing length-to-diameter ratio (L/D). Triaxial responses varying by less than 5% can be attributed to typical scatter in triaxial experiments performed on heterogenous materials such as concrete [[4,31]]. The experimental approach uses a sealed specimen with fluid pressure applying confinement. Several specimen geometries are considered, including multiple diameters (50 mm and 25 mm) and multiple values of L/D (0.5, 1.0, and 2.0). Novel insights are presented for interpreting experimental data from non-standard specimen geometries subjected to triaxial loading conditions.

2.2 Material and Methods

2.2.1 Material and Specimen Preparation

The high-strength concrete investigated during this study is referred to in the literature as BBR9 [35,36] and has a maximum aggregate size of 4.75 mm. BBR9 is a self-consolidating concrete (SCC) that contains the following constituent materials: manufactured limestone sand, type I/II portland cement, grade 100 ground granulated blast-furnace slag (GGBFS), undensified microsilica (silica fume), polycarboxylate-ether-based high-range water reducing admixture (HRWRA), and tap water. Mixture proportions for this concrete are presented in **Table 1**. The development of BBR9 utilized central composite design (CCD) of experiments methodology while focusing on dense particle packing, minimization of flaws, and maximum calcium silicate hydrate (CSH), as described in prior publications [37,38]. Rheological property measurements included fresh properties per ASTM C 230 [39] (without drops) to obtain a spread value (flow). All hardened concrete specimens were obtained using the coring process as defined in ASTM C 42 [40]. After retrieving cores with the desired diameter, specimens were cut with a precision diamond blade and finished on a double-sided planetary lapping machine to achieve parallelism and flatness within 25 μm. Unconfined compressive strengths were determined as prescribed by ASTM C 39 [11], although some values for specimen diameter and L/D fall outside of the recommended ranges. A representative cross section of BBR9 is shown in **Fig. 2**.

Table 1: Mixture proportions for BBR9 high-strength concrete

Constituent	Mixture proportions, by weight	Specific gravity
Cement (Type I-II)	1.00	3.15
Manufactured limestone sand	2.25	2.57
Slag	0.60	2.95
Microsilica (silica fume)	0.26	2.20
Tap water	0.37	1.00
High-range water-reducing admixture	0.03	1.20

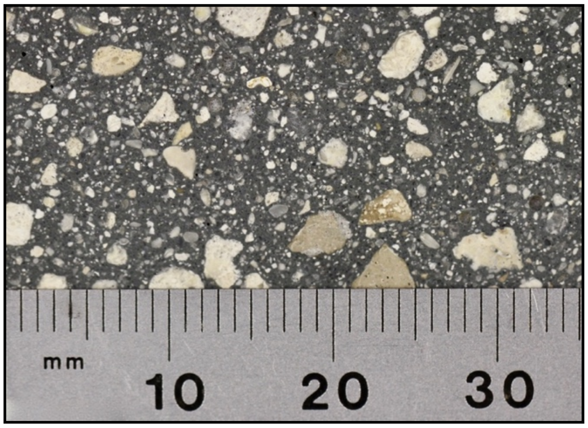

Fig. 2: Cross-sectional image of BBR9 high-strength concrete

2.2.2 Triaxial Test Equipment and Instrumentation

Triaxial compression experiments were conducted using a 600-MPa-capacity pressure vessel paired with an 8.9-MN universal testing machine to provide axial loads. Radial confinement was applied using a 50/50 mixture of hydraulic oil and kerosene as the confining fluid. Test specimens were placed between hardened steel caps, and then two 0.6-mm-thick latex membranes and an Aquaseal® membrane were installed around the specimen. An additional latex membrane was then installed with the outside of the assembly being sealed with a liquid nitrile rubber. The purpose of this extra precaution was to secure the membrane to the caps and prevent deterioration by the confining fluid. Pictures of sealed triaxial test specimens are shown in **Fig. 3**. A cross-sectional view of the pressure vessel is shown in **Fig. 4**. An MTS FlexTest controller and data acquisition system were adopted for servo-controlled test conditions based on displacement, load, and/or pressure to achieve the desired stress or strain path.

Axial deformation measurements were made with two linear variable differential transformers (LVDTs) located 180 degrees apart. For 25-mm-diameter specimens, radial deformation measurements were acquired using an LVDT-type lateral deformeter mounted to the vertical centerline of the specimen using footings that were glued to the specimen surface and located 180 degrees apart. Specimens with a 50-mm diameter experienced higher radial strains, requiring the use of strain-gaged spring-steel arms allowing for larger deformations.

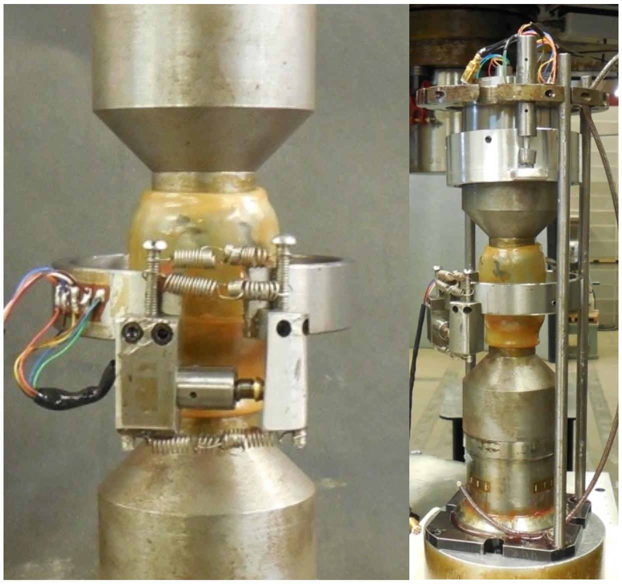

Fig. 3: Closeup view of sealed triaxial specimen (left) and specimen inside the instrumentation cage (right)

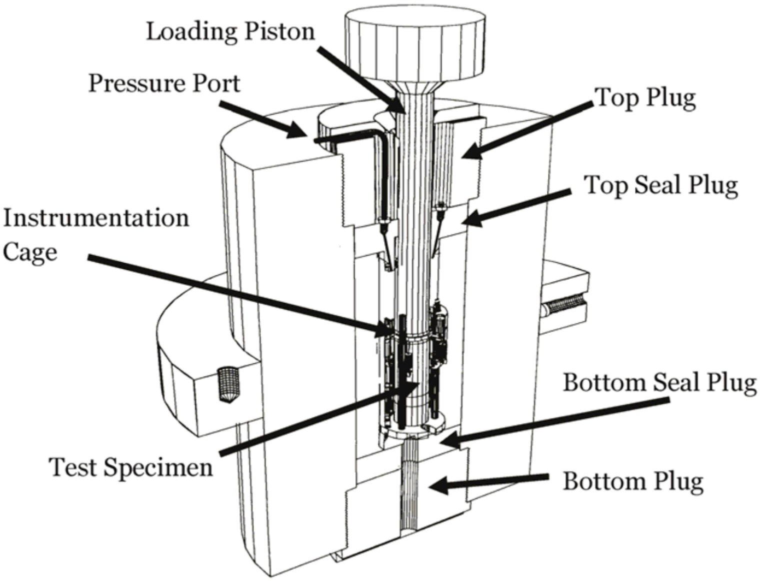

Fig. 4: Cross-sectional view of triaxial pressure chamber used to test concrete specimens [41]

Triaxial experiments were performed in two testing phases. The first phase was hydrostatic loading that increased fluid pressure in all directions so that the principal stress difference was zero ($\sigma_1 = \sigma_2 = \sigma_3$). The second phase maintained constant radial stress ($\sigma_1 = \sigma_2$) through fluid pressure while increasing the axial stress (σ_3) with a hydraulic actuator. All confined experiments presented in this study are considered to be undrained triaxial compression experiments since the pore fluid (liquid and/or gas) is unable to escape the membrane-enclosed specimens. Additional information on the testing apparatus can be found in ERDC technical reports [31,32,42-44].

2.2.3 Definitions for Strain and Stress Measurements

Radial strain (ε_r) measurements and axial strain (ε_a) measurements were continuously recorded through hydrostatic and triaxial loading phases. Volumetric strain (ε_v) was calculated as the sum of the axial strain and twice the radial strain, as shown in **Eq. 1**. Reported stress values are in terms of true stress, as they are based on the changing cross-sectional area of the specimen. The principal stress difference (q) is defined by the difference between radial stress (σ_r, or σ_1 and σ_2) and axial stress (σ_a, or σ_3), as shown in **Eq. 2**. Mean normal stress (p) is defined as the average of applied principal stresses, as shown in **Eq. 3**.

Eq. 1:

$$\varepsilon_v = \varepsilon_a + 2\varepsilon_r$$

Eq. 2:

$$q = \sigma_a - \sigma_r$$

Eq. 3:

$$p = \frac{(\sigma_1+\sigma_2+\sigma_3)}{3} = \frac{(\sigma_a+2\sigma_r)}{3}$$

2.3 Results and Discussion

2.3.1 Baseline Triaxial Experiments

The baseline triaxial compression experiments were conducted on cylindrical BBR9 specimens with a diameter of 50 mm and a height of 114 mm. The ERDC has used this particular specimen geometry for all of the triaxial experiments performed in the past decade. Since triaxial experiments are time/labor consuming, two replicate tests are typically performed at each testing condition. If the results show a large discrepancy, a third test is performed. For the BBR9 test series, two replicates were used to acquire triaxial compressive response under confining pressures of 10, 20, 50, 100, 200, and 300 MPa. The average response at each level of confining pressure is plotted in **Fig. 5** in terms of principal stress difference and axial strain. The resulting data were then plotted in terms of mean normal stress to show triaxial loading paths and peak loads, as shown in **Fig. 6**. The peak stresses were then used to develop a calibrated failure surface, using parameters described by the Advanced Fundamental Concrete (AFC) model [36].

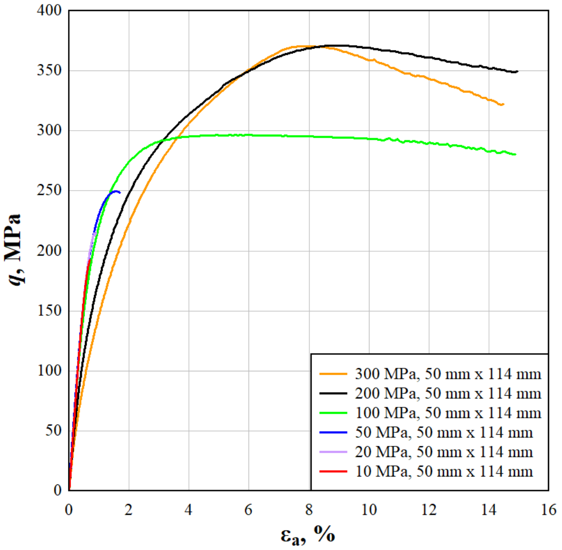

Fig. 5: Triaxial response of concrete specimens with 50-mm diameter to observe material response in terms of principal stress difference (*q*) and axial strain (ε_a) at confining pressures of 10, 20, 50, 100, 200 and 300 MPa

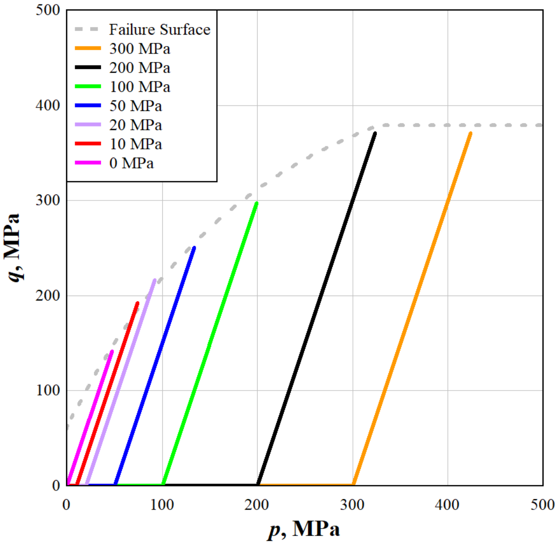

Fig. 6: Triaxial stress paths and failure surface

With increasing confinement pressures, the concrete transitions through multiple damage modes. In the unconfined state, the ultimate compressive strength for BBR9 is 141 MPa with a damage mode that is overwhelmed by unstable macrocrack propagation. As the confining pressure increases up to 10 and 20 MPa, crack growth is slightly stabilized. This stabilization leads to an increased compressive strength while maintaining a linear-elastic response until failure. At confining pressures of 50 MPa, the concrete begins to transition to a quasi-brittle failure regime where the material exhibits apparent plastic deformation. With confinement pressures in the range of 100-300 MPa, the material begins to flow plastically, as evidenced by the axial strain values extending to 15%. Although the specimens could continue to sustain mechanical loading beyond these strains, the specimens were unloaded after reaching a strain of 15% (the selection of this value is discussed in more detail in section **2.3.4**).

Based on the triaxial compressive behavior from the baseline BBR9 specimens, the following representative confinement pressures (and related failure modes) were selected to further analyze size effects: 10 MPa (brittle), 50 MPa (quasi-brittle), 100 MPa (ductile), and 200 MPa (ductile).

As a general note, the baseline triaxial experiments conducted in this section were performed with the concrete specimens directly in contact with steel loading platens. Although this is typical for historical triaxial work performed at the ERDC, a molybdenum disulfide (MoS_2) lubricant was applied between the concrete-platen interface for all reduced diameter (25 mm) specimens in this study. This step was taken to minimize frictional effects and improve repeatability. According to Van Mier, a decreasing frictional constraint in a triaxial experiment will result in decreasing post-peak ductility [45], which is more representative of true material behavior.

2.3.2 Effects of Specimen Size

Before investigating size effects under triaxial loads, it is important to quantify material behavior under unconfined compression. For these experiments, concrete specimens were cored and ground to achieve a constant L/D of ~2 for specimen diameters of 25 mm and 50 mm. Results from these experiments are presented in **Table 2**. The average compressive strength of the 25-mm-diameter specimens was 130.8 MPa, which represents a 7.5% decrease in strength as compared to the strength of 50-mm-diameter specimens at 141.4 MPa. Meanwhile, the coefficients of variation for baseline specimens were 5.6% and 7.3%, respectively. The observed decrease in the compressive strength of smaller specimens can be attributed to the reduction of frictional confinement at the specimen ends due to the application of the MoS_2 lubricant.

Similarly, the application of the lubricant also reduces the experimental scatter for smaller specimens.

Table 2: Unconfined compressive strength for BBR9 specimens with varying diameter

	Unconfined Compressive Strength (MPa)	
Specimen Number	25-mm Diameter	50-mm Diameter
1	123.9	151.2
2	130.1	125.0
3	141.6	147.3
4	131.9	134.4
5	118.0	138.7
6	134.8	132.9
7	137.9	159.1
8	125.5	140.7
9	133.6	143.5
Mean	130.8	141.4
Standard deviation	7.35	10.29
Coefficient of variation, %	5.62	7.28

Size effects were then evaluated by using the same specimen geometries for triaxial compression experiments. The principal stress difference was recorded as a function of axial strain, as shown in **Fig. 7**. For direct comparison, baseline data for 50- x 114-mm-diameter specimens are shown in dashed lines, and reduced diameter specimens (25 x 50 mm) are shown in solid lines. Minimal discrepancies were observed between baseline specimens and reduced diameter specimens at confining pressures of 10, 50, and 100 MPa. However at 200 MPa, the size effect begins to cause a deviation on stress-strain response at axial strains exceeding 8%.

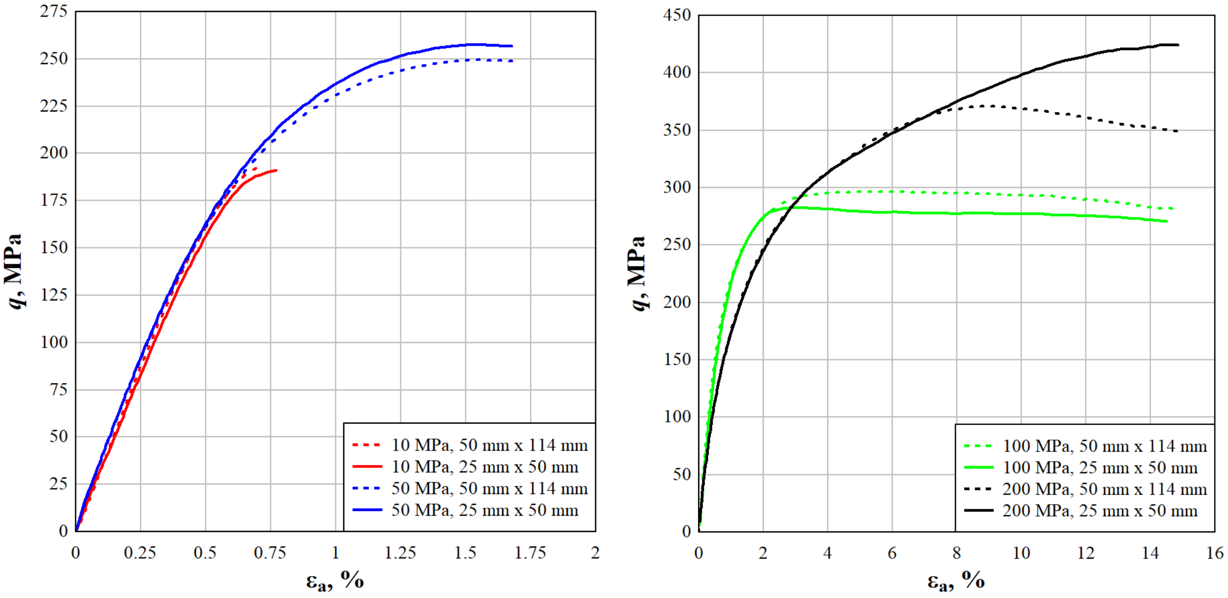

Fig. 7: Triaxial response of concrete specimens with 50-mm and 25-mm diameters to observe size effects in terms of principal stress difference (q) and axial strain (ε_a) at confining pressures of 10, 50, 100, and 200 MPa

It is evident from **Fig. 7** that all peak stress results match within 5% for varied specimen diameters under the same confinement pressure except for the 200-MPa confinement at large strains exceeding 8%. This degree of variability is common for heterogenous materials such as concrete, even with the same specimen size. Therefore, reducing the diameter from 50 mm to 25 mm while maintaining the L/D ratio has negligible effects on the triaxial response of BBR9 concrete. As a reference, BBR9 has a maximum (sand) particle size of 4.75 mm and a maximum pore size of 3.0 mm**.** Note that results for concretes with larger constituents (e.g., aggregate, fibers, and entrapped air) may not be representative of the bulk materials for specimens with a 25-mm diameter. However, it is likely that similar results would be observed for mortars, grouts, and UHPC materials with similarly sized constituents.

2.3.3 Effects of Length-to-Diameter Ratio

To determine a reasonable range of L/D, specimens were initially investigated with a diameter of 25 mm and a length of 12.7 mm (L/D = 0.5). This specimen geometry is common for high-rate unconfined Kolsky bar experiments performed on cementitious composites. At 200 MPa confining pressure, triaxial compression results were compared for L/D = 2 and L/D = 0.5 with a specimen diameter of 25 mm, as shown in **Fig. 8**. These preliminary results showed that the boundary conditions at the specimen ends included substantial frictional confinement effects, which caused material response to deviate at axial strains of 3.0%. Therefore, in an effort to reduce the end effects on the triaxial compressive response, additional specimens were fabricated with L/D = 1.0 at the same diameter for further evaluation.

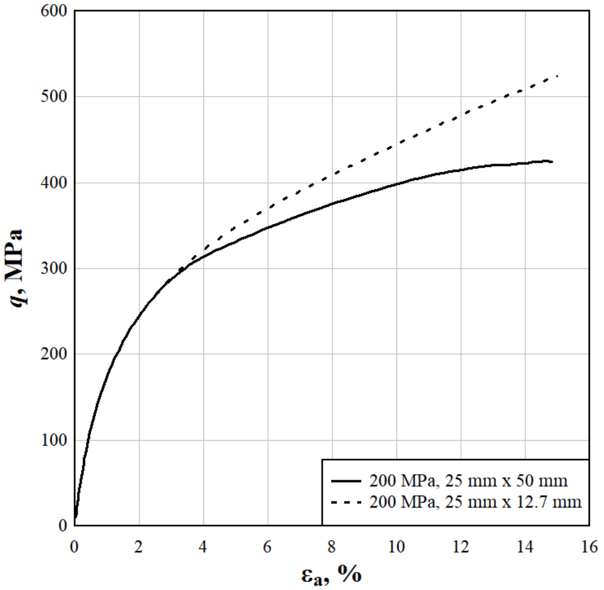

Fig. 8: Triaxial response of concrete specimens with 25-mm diameter and L/D of 2.0 and 0.5

Specimens with a diameter and height of 25 mm (L/D = 1) were fabricated to take a more in-depth look at the effects of changes in aspect ratio. First, unconfined compression experiments were conducted on specimens with different L/D, as displayed in **Table 3**. The average strength of the L/D = 1.0 specimens (140.7 MPa) must be multiplied by a correction factor of 0.93 to achieve the average compressive stress for L/D = 2.0 specimens (130.8 MPa). The strength correction for specimens with nonstandard aspect ratios is detailed in ASTM C39 [3], with a correction factor of 0.87 for L/D = 1.0. However, these published correction factors are intended only for concretes with a compressive strength below 42 MPa.

Table 3: Unconfined compressive strength for BBR9 specimens with varying L/D

	Unconfined Compressive Strength (MPa)	
Specimen Number	L/D = 1.0	L/D = 2.0
1	144.2	123.9
2	153.4	130.1
3	126.8	141.6
4	134.1	131.9
5	142.0	118.0
6	144.4	134.8
7	131.1	137.9
8	137.8	125.5
9	152.1	133.6
Mean	140.7	130.8
Standard deviation	9.06	7.35
Coefficient of variation, %	6.44	5.62

Subsequent triaxial compression experiments were performed on the 25- x 25-mm specimens and then compared to the triaxial results from 25- x 50-mm specimens, as shown in **Fig. 9**. As observed in the unconfined experiments, the shorter specimens (L/D = 1) have an apparent increase in strength. However, the relative trend for material response remains consistent at each level of confinement pressure (10, 50, 100 and 200 MPa). Modulus values show some deviation at low stress levels due to variations in compliance corrections for axial strain measurements. As observed in the literature, a reduction in L/D results in a more ductile stress-strain curve with a higher peak stress which may be attributed to frictional restraint in the shear band [45].

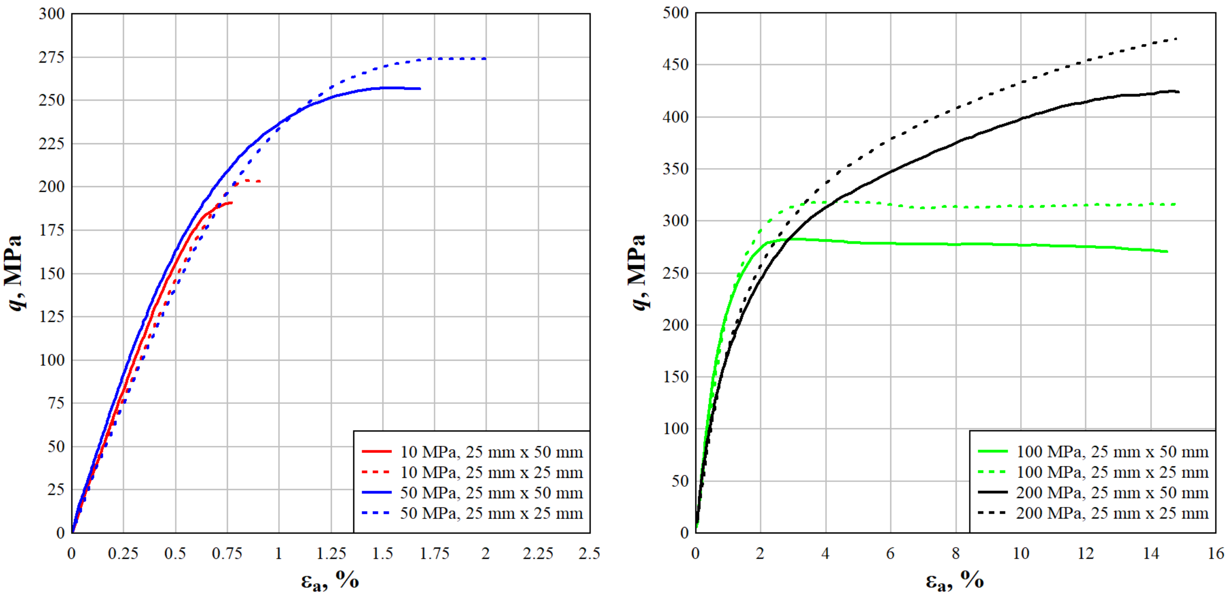

Fig. 9: Triaxial response of 25-mm-diameter concrete specimens with L/D = 2.0 and 1.0 to observe size effects

Since ASTM C39 presents simple correction factors for unconfined compressive strength of concrete, similar correction factors were calculated for each confining pressure to correlate data with L/D = 2.0 specimens and L/D = 1.0 specimens. According to the literature [13,14,40,46], the correction factor for specimens with an L/D of 1.0 should be in the range of 0.80 and to 0.91. However, as shown in **Table 4**, the correction factors calculated at different confinement pressures present a much narrower range from 0.89 to 0.94. The corrected stress-strain response for L/D = 1.0 specimens are shown in **Fig. 10**. These correction factors provide a reasonable method to relate triaxial behavior of short specimens to that of standard L/D specimens. The primary discrepancy among specimens with different aspect ratios is that the elastic portion of the curves from L/D = 1 specimens appears to slightly underestimate the material stiffness at low confinement pressures. This is probably due to the variability of compliance measurements for axial strain calculations.

Through extensive studies, ASTM C39 correction factors have been thoroughly documented and broadly used for unconfined compressive strength. However, no similar literature exists for cementitious materials under triaxial loading conditions. Since the behavior of concrete is drastically different under triaxial stress states [47-49], it is imperative that we understand the size effects under various complex stress states. Although the recommended correction factors might be specific to a particular class of materials, they still provide engineering significance for interpreting triaxial behavior from non-standard specimens (similar to the current use of ASTM C39 correction factors).

Table 4: Correction factors to account for changes in L/D

	Peak Stress (*q*) with Confining Pressures at:			
	0 MPa	10 MPa	50 MPa	100 MPa
25 x 50 mm	130.8	191.1	257.6	282.7
25 x 25 mm	140.7	204.2	274.0	318.3
Correction Factor	0.93	0.94	0.94	0.89

* Note that peak stresses are not observed at 200 MPa, but a correction factor of 0.92 was determined to provide the best fit.

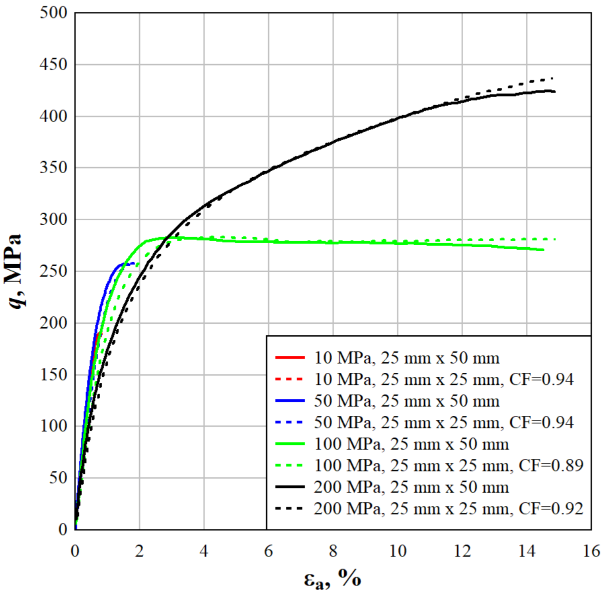

Fig. 10: Triaxial response of 25-mm-diameter concrete specimens with correction factors from Table 4 applied to L/D = 1 specimens

2.3.4 Limitations of Experimental Setup

As described in section **12.2.2**, the radial strain measurements are taken at the center of the specimens. These strain values are then used to calculate the true stress as the cross-sectional area increases under axial compression. However, at high axial strains, the specimen geometry starts to "barrel," as shown in **Fig. 11**. When the cross-sectional area begins to vary throughout the specimen, a local area measurement will no longer suffice for calculating volumetric strains. At this stage, the specimen is no longer under a uniform true stress loading condition.

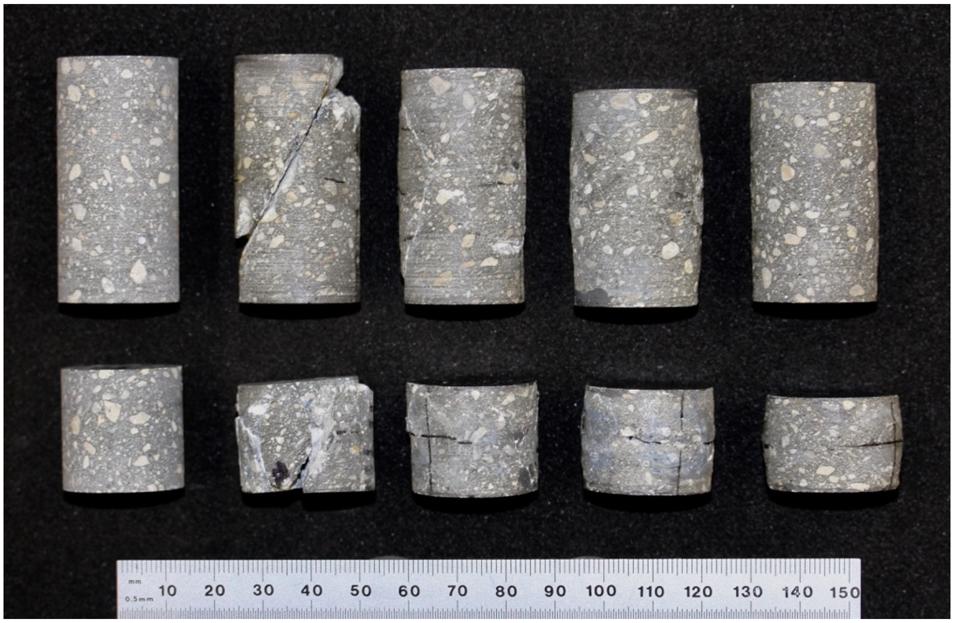

Fig. 11: 25-mm x 50-mm specimens (top) and 25-mm x 25-mm specimens (bottom) under the following conditions (from left to right): pristine, 10 MPa, 50 MPa, 100 MPa, and 200 MPa

To further investigate this phenomenon, tests were conducted in the ductile failure regime up to axial strains of ~30%. If the material has a scalar value of Poisson's ratio, a steady slope should be observed while plotting axial versus radial strains. However,

Fig. 12 shows that the slope is not constant. Each curve has three distinct phases: pore collapse/crushing (non-linear portion starting at zero up till ~5% axial strain), uniform deformation (axial strains of 5-10%), and non-uniform deformation (axial strains beyond 15%). Reference lines are included for the non-uniform (barreling) region to highlight the distinct change in slopes. As observed in **Fig. 11**, barreling is more prevalent in the 25-mm x 50-mm specimens, which is also supported by the higher measured radial strains for a given axial strain. To further confirm this observation, **Fig. 13** shows the dramatic barreling that occurs after undergoing axial strains up to 30%. The corresponding internal microstructures were also captured using micro-CT to confirm that the pore structure had completely collapsed. These experimental results suggest that only the first 10% strain on the triaxial stress-strain curve, which are obtained under relatively uniform deformation, may be used for constitutive modeling.

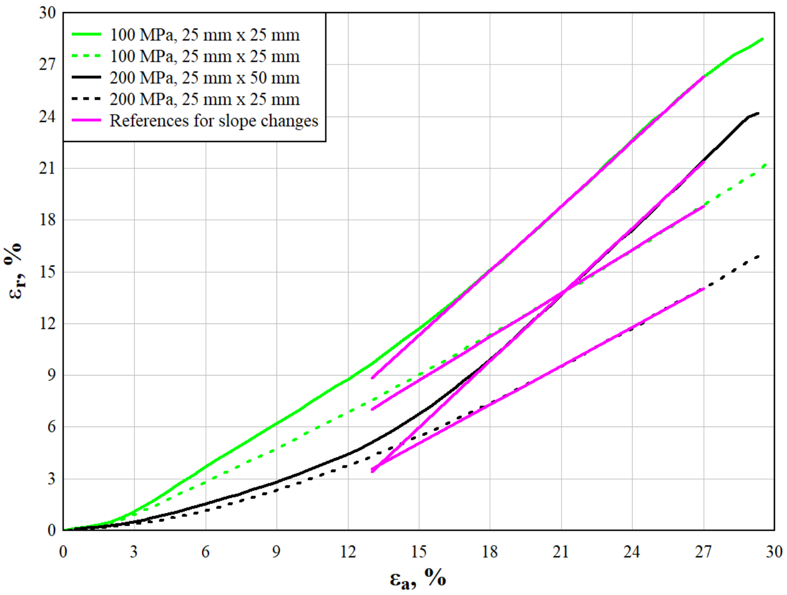

Fig. 12: Axial strain (ε_a) and radial strain (ε_r) measurements at confining pressures of 100 and 200 MPa

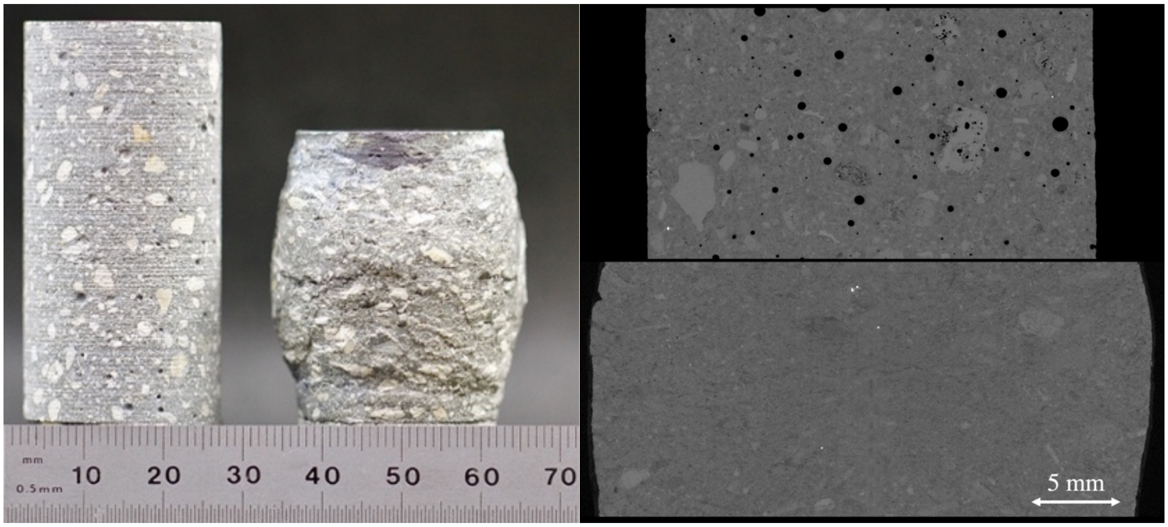

Fig. 13: Pristine vs. damaged specimens after 30% axial strain at 100 MPa (left) with corresponding microstructure for the pristine (top right) and damaged (bottom right) conditions

2.4 Conclusions

High-strength concretes, such as BBR9 used in this study, must be characterized under a variety of triaxial loading conditions for the calibration of material models that are used to predict dynamic impact events. This is typically done using cylindrical specimens with a diameter of 50 mm and a height of 100 -115 mm. However, high-strength concrete specimens with both reduced diameter (25 mm) and length-to-diameter ratio (L/D = 1.0) can also be used to characterize material behavior under triaxial loading conditions. By investigating changes in specimen diameter and L/D, the following conclusions can be drawn from this study on high-strength concrete.

- For high-strength concretes with a maximum particle size < 5 mm, it is reasonable to assume that there is a negligible size effect when comparing triaxial behavior of 25-mm x 50-mm specimens and 50-mm x 114-mm specimens.

- The value of L/D has a noticeable effect on the observed triaxial response. Values of L/D below 1.0 are not recommended as frictional effects become more apparent.

- The unconfined compressive response of 25-mm x 25-mm specimens (L/D = 1.0) can be correlated to the unconfined compressive response of 25-mm x 50-mm (L/D = 2.0) specimens by using a correction factor of 0.93.

- The triaxial compressive response of 25-mm x 25-mm specimens (L/D = 1.0) can be correlated to the triaxial compressive response of 25-mm x 50-mm (L/D = 2.0) specimens by using a correction factor in the range of 0.89-0.94.

- Although the proposed triaxial correction factor is primarily intended to provide the appropriate value of peak stress, the scalar factor also provides excellent correction to the full dataset in terms of principal stress difference (q) versus axial strain (ε_a).

- It should also be noted that a reduced specimen geometry may not be representative for concretes with large aggregates and/or fibers.

The use of a reduced specimen geometry provides opportunities to explore new parameters under triaxial loading conditions. First, a smaller specimen diameter allows for higher resolution morphometry data using conventional micro-computed tomography (micro-CT) scanners, where scan resolution increases as specimen size decreases. The corresponding micro-CT scans would allow for observing and quantifying damage mechanisms after exposure to triaxial loadings at various confining pressures. Second, specimens with a reduced diameter and a reduced L/D could be used for future dynamic triaxial experiments while satisfying the assumptions of constant strain rate and stress equilibrium. The dynamic triaxial loading results could further complement the quasi-static triaxial data by adding crucial strain-rate sensitivity to the concrete constitutive models. Future work will focus on using reduced specimen geometries to explore micro-CT and dynamic properties for high-strength concretes subjected to triaxial loads.

CHAPTER 3:

DAMAGE EVOLUTION

3.1 Introduction

Under a penetration event with multiple impacts, it is critical to know the state of damaged material in order to have predictive capabilities for subsequent impacts. This problem has proven to be very challenging for DoD researchers due to the very limited knowledge on pressure-dependent damage evolution for high-strength concrete. Many models incorporate a scalar damage variable that describes damage arbitrarily from zero (pristine) to one (fully damaged). However, the implementation of this parameter would be more effective if related to physical observations and measurements. In order to improve modeling capabilities, researchers have extensively investigated damage and fracture processes of brittle materials [50-55]. Through the use of nondestructive X-ray microtomography (micro-CT), internal damage can be documented in three dimensions to better understand complex cracking and fracture patterns. Rather than solely using a statistical distribution to describe flaws and damage, micro-CT provides a method to precisely characterize discrete features to better understand crack nucleation and propagation within the various phases of brittle geomaterials [56].

Through the development of high-resolution micro-CT, heterogeneities at small length scales can be precisely visualized and characterized allowing for better understanding of crack nucleation and propagation within complex geomaterials [56]. Cnudde provides a thorough review of the history of micro-CT as it relates to geosciences to include advantages, limitations, artifacts, and operator dependencies [57]. Although large CT systems had previously been used for concrete [58], Landis was one of the pioneers for utilizing micro-CT to investigate cementitious materials as he worked toward providing a physical basis for a scalar damage variable [59]. Landis used synchrotron radiation to map 3D crack morphology of loaded concrete cylinders (4 mm x 4 mm) with an initial voxel resolution of 6 μm [60,61] that later improved to 1.2 μm [62]. Researchers have also been pairing micro-CT studies with digital image correlation (DIC) [63] and eventually digital volume correlation (DVC) to measure displacements within heterogeneous materials to evaluate strain fields [64]. Micro-CT has provided valuable insight to concrete researchers in terms of compression [52,65,66], splitting tension [53,67], porosity [68], thermal effects [69], and self-healing [70]. A thorough review of micro-CT research as it relates specifically to cementitious materials has been documented by Brisard et al. [71].

Although micro-CT has been widely used on cementitious materials, the technique has been used infrequently for investigating specimens undergoing high-pressure triaxial loadings. In order to perform in situ micro-CT scans of specimens under confining pressure, the pressure vessel must be sufficiently X-ray transparent in order to achieve the desired resolution of the specimen. This poses many additional technical challenges, but the results would provide valuable information to measure crack formation without unloading the specimen and therefore causing crack closure. In situ micro-CT scans have been performed on Utica shale under triaxial direct-shear fracturing with confining pressures up to 22.2 MPa and a 25-μm voxel size [72]. However, an in situ scan for triaxial compression testing of concrete is not feasible since non-X-ray transparent pressure vessels are required to achieve pressures that produce ductile failure modes in concrete. Nonetheless, some researchers have performed ex situ scans to characterize triaxial damage modes for unloaded specimens made from conventional-strength concrete containing coarse aggregates [26].

However, to the best of the authors' knowledge, triaxial damage states have not been investigated for high-strength concretes that do not contain coarse aggregates. Furthermore, prior investigations using micro-CT for triaxial damage studies have not included volumetric strain measurements. Although strain gauges can be used for radial strain measurements, the strain readings are localized and may not sufficiently represent the bulk behavior. Additionally, strain gauges would cause artifacts in micro-CT scans of damaged specimens. Therefore, a removable strain sensor must be implemented so that damaged specimens can be fully analyzed using micro-CT. Potential solutions include a radial strain sensor [73] or an LVDT (Linear Variable Differential Transformer) based lateral deformeter with removable gauge mounts [74].

Although pressure-dependent material properties of high-strength concretes have been thoroughly documented [4,75-77], the corresponding triaxial damage modes are not well understood. This study aims to assess the damage evolution and size effects of high-strength concrete under hydrostatic and triaxial stress states with confining pressures up to 200 MPa to capture brittle, quasi-brittle, and ductile failure modes. Triaxial experiments are performed using a sealed specimen with hydrostatic fluid pressure maintained in the radial direction while an additional axial load is applied by a hydraulic actuator. Volumetric strains are calculated using vertical LVDTs and a radial strain sensor with removable mounts. A high-resolution laboratory micro-CT scanner is implemented to non-destructively view and analyze pristine and damaged concrete specimens. The resulting micro-CT scans allow for damage visualization and measurements in terms of volumetric strains, shear planes, crack saturation, and the evolution of pore size distributions. Additionally, residual strength measurements provide a method to connect damage morphologies to quantifiable material properties.

3.2 Materials and Methods

3.2.1 Material and Specimen Preparation

A high-strength self-consolidating concrete referred to as BBR9 was selected for all of the testing and characterization presented in this study. BBR9 has been previously documented in the literature to include design philosophy [78] and mechanical performance [35,79-81]. Damage modes have also been investigated for unconfined compression experiments at high strain rates [65]. The mixture proportion for BBR9 is presented in **Table 5** consisting of the following constituent materials: manufactured limestone sand, type I/II portland cement, grade-100 ground granulated blast-furnace slag (GGBFS), undensified microsilica (silica fume), polycarboxylate-ether-based high-range water-reducing admixture (HRWRA), and tap water. The concrete contains no coarse aggregate, and the fine aggregate (sand) has a maximum particle size of 4.75 mm.

Table 5. Mixture proportions for BBR9 high-strength concrete.

Constituent	Mixture Proportions, by Weight	Specific Gravity
Cement (Type I-II)	1.00	3.15
Manufactured limestone sand	2.25	2.57
Slag	0.60	2.95
Microsilica (silica fume)	0.26	2.20
Tap water	0.37	1.00
High-range water-reducing admixture	0.03	1.20

Cylindrical specimens with a diameter of 25.4 mm were cored from bulk samples in accordance with ASTM C 42 [40]. A precision saw was used to cut the specimens slightly longer than the desired length. The final specimen lengths of 25 mm and 50 mm were achieved using a PR Hoffman PR-1 85T double-sided planetary lapping machine resulting in parallelism and flatness within 25 μm. Pristine BBR9 specimens are shown in **Fig. 14**.

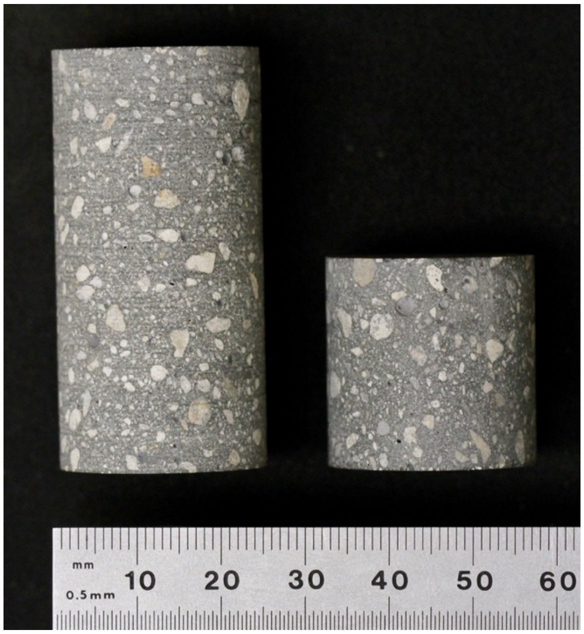

Fig. 14. Pristine cylindrical BBR9 high-strength concrete specimens with L/D = 2.0 (left) and L/D = 1.0 (right)

3.2.2 Quasi-static Hydrostatic and Triaxial Compression

The quasi-static hydrostatic and triaxial test equipment is detailed in the literature [4,42,44]. An in-depth review of the quasi-static triaxial testing on 25-mm-diameter BBR9 concrete specimens is presented in previously published work [74]. As a brief overview, the cylindrical concrete specimen is sealed with fluid pressure being applied to the entire specimen to achieve a hydrostatic stress state. For the triaxial loading, the desired level of fluid confinement pressure is held constant in the radial direction while an actuator loads the specimen in the axial direction. Furthermore, a MoS_2-based lubricant is applied at the specimen/platen interface to reduce frictional end effects.

Triaxial experiments frequently report data in terms of principal stress difference versus mean normal stress. All results in this study are presented in terms of true stress through active monitoring of the specimen's cross-sectional area using a centrally located LVDT-based lateral deformeter with removable gauge mounts. The principal stress difference (*q*) is defined by the difference between axial stress (σ_a, or σ_3) and radial stress (σ_r, or σ_1 and σ_2), as shown in **Eq. 4**, and mean normal stress (*p*) is defined as the average of applied principal stresses, as shown in **Eq. 5**. Specimen deformations were measured in terms of axial strain (ε_a) and radial strain (ε_r), with volumetric strain (ε_v) being calculated as defined in **Eq. 6**. Triaxial confinement pressures of 10 MPa, 50 MPa, 100 MPa, and 200 MPa were selected to facilitate different types of damage modes (brittle, quasi-brittle, and ductile).

Eq. 4:
$$q = \sigma_a - \sigma_r$$

Eq. 5:
$$p = \frac{(\sigma_1+\sigma_2+\sigma_3)}{3} = \frac{(\sigma_a+2\sigma_r)}{3}$$

Eq. 6:
$$\varepsilon_v = \varepsilon_a + 2\varepsilon_r$$

3.2.3 Micro-computed Tomography

For damage visualization and quantification, X-ray microtomography was utilized for nondestructive characterization. All micro-CT scans presented in this study were conducted on a Bruker Skyscan 1173 high-energy spiral-scan micro-CT with a maximum X-ray energy of 130 kV and a 5-megapixel (2240x2240) flat-panel sensor. Offset scans were used for all specimens by stitching side-by-side horizontal scans for the purpose of achieving the highest possible resolution. Optimized scan settings for 25.4-mm-diameter concrete specimens were determined to be 130 kV and 60 µA with a rotational step size of 0.20 degrees for 360-degree scans. A 0.25-mm thick brass filter was also used to remove lower energy X-rays that cause beam hardening artifacts on dense specimens. To reduce the effects of noise in the X-ray detector signal, dark flatfield corrections were updated at 60-minute intervals throughout the scan and 14 frames were averaged to record each saved X-ray projection image. Random stage movements (up/down) were also employed to reduce any artifacts that might be present from defective pixels in the detector. Voxel sizes were in the range of 8.8-25 µm depending on the specimen size and field of view and are notated in each relevant section.

Cone-beam X-ray tomography projection images were reconstructed into cross-sectional images using a Feldkamp algorithm within Bruker's NRecon software paired with the GPUReconServer reconstruction engine. Reconstruction parameters included a beam hardening correction of 15 and a ring artifacts correction of 15. To illustrate the input and output of the reconstruction process, an example projection image and reconstructed cross-sectional image are provided in **Fig. 15**. Finally, all of the cross-sectional images are vertically stacked to provide a complete dataset made up of 256-bit grayscale spectrum where black voxels represent the lowest density and white voxels represent the highest density.

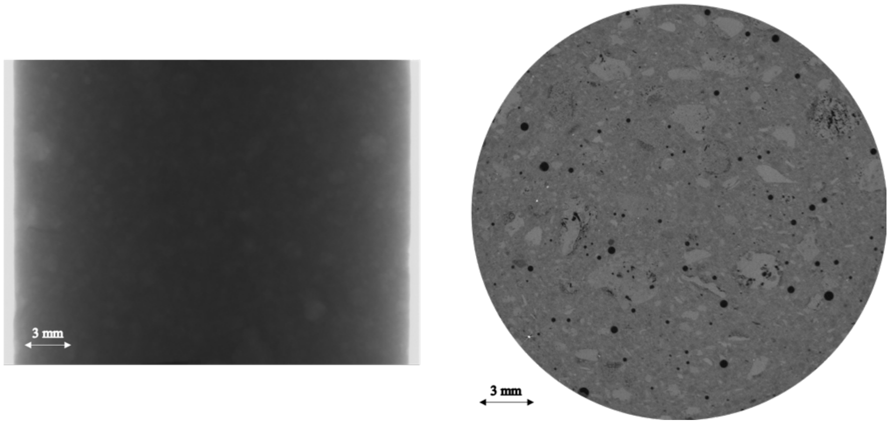

Fig. 15. X-ray projection image (left) and reconstructed cross-sectional image (right)

The 3D microstructure of each specimen was recorded before and after loading to better understand damage initiation and propagation. Analysis for brittle failure modes focused on isolating large interconnected crack networks for visualization purposes and for measuring shear plane angles. For ductile failure modes (as observed at the macroscale), cracking occurs at a length scale that is not detectable within the resolution restrictions of the Skyscan 1173 micro-CT. Nonetheless, micro-CT data still provides a means to quantify changes in pore structure.

3.2.4 Image Segmentation

Reconstructed cross-sectional images were all loaded into DataViewer to register pristine and damaged datasets to have the same orientation using sagittal, coronal and transverse plane views as shown in **Fig. 16**. Subsequently, unique features at the top and bottom boundaries of the pristine volumes of interest (VOIs) were identified in the damaged specimen scan data to appropriately determine the damaged VOIs. After registration, binary image operations were performed in CT-Analyser. Segmentation began with an automatic Otsu threshold method applied to a global histogram function while visually confirming that pore space was segmented appropriately from the surrounding concrete matrix. After segmenting distinct phases, a shrink-wrap tool was implemented to define the region of interest. Analysis included 2D measurements for the porosity of individual cross-sectional images and 3D measurements for global porosity measurements. Furthermore, individual object analysis was performed on each and every discreet binarized object (i.e., pore) in terms of either volume equivalent sphere diameter or major diameter. Objects were also binned into color coded images based on pore sizes to produce 3D images that clearly compare and contrast void structures before and after triaxial loading.

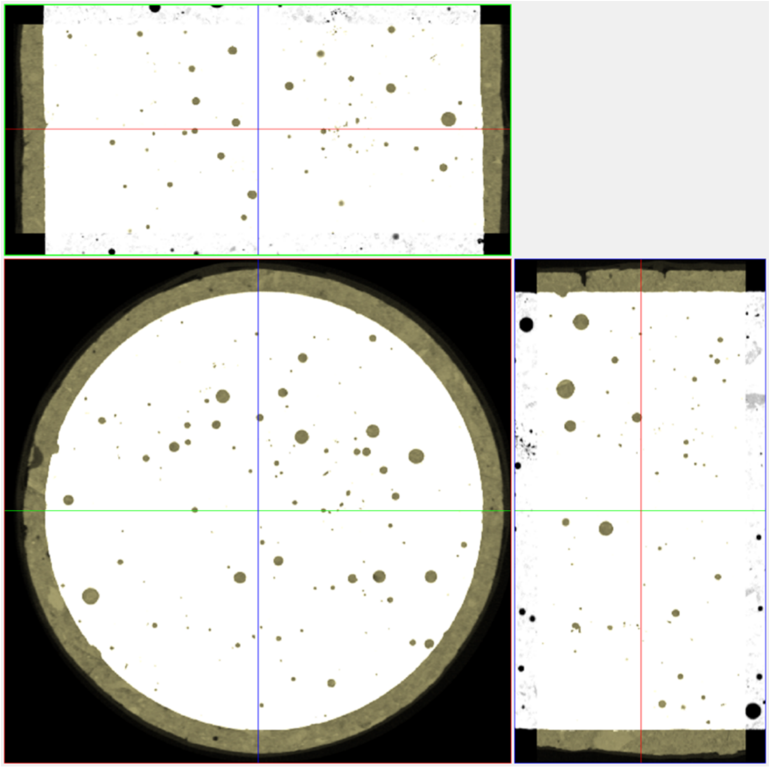

Fig. 16. DataViewer registration example for pristine (white) and damaged (brown) micro-CT scan data

The geometry of brittle damage observed in the specimens features multiple hairline fractures that are poorly captured by the thresholding segmentation. The fractures are segmented with discontinuities or not identified at all. Similarly, the fine aggregate posed problems with thresholding due to either thin features (shells) or high local variations of intensity (larger objects). Thus, to observe how fracture patterns relate to all phases in the material, selected specimens have been segmented with a manually trained Fast Random Forest machine learning algorithm [82,83]. After segmentation, fracture geometry has been inspected and corrected manually to provide the most accurate representation.

3.3 Results and Discussion

3.3.1 Triaxial Compression Data

Triaxial compression (TXC) specimens were tested with length-to-diameter ratios (L/D) of 2.0 (25 mm x 50 mm) and 1.0 (25 mm x 25 mm). Replicate tests were conducted at each combination of pressure level and specimen size. For the first phase of a triaxial experiment, the specimen is initially loaded hydrostatically up to the desired confinement pressure. To illustrate material behavior under hydrostatic compression (HC) conditions, **Fig. 17** presents loading and unloading data for hydrostatic specimens up to a mean normal stress (p) of 200 MPa. Note that the hydrostatic loading is fully reversible under these test conditions. TXC data is presented in **Fig. 18** and **Fig. 19**, where each curve represents the average of two replicate experiments. Results are plotted in terms of both volumetric strains and axial strains. Although axial strains have been reported and discussed previously [74], the inclusion of volumetric strain measurements provides valuable insight when interpreting micro-CT imagery of triaxially damaged specimens.

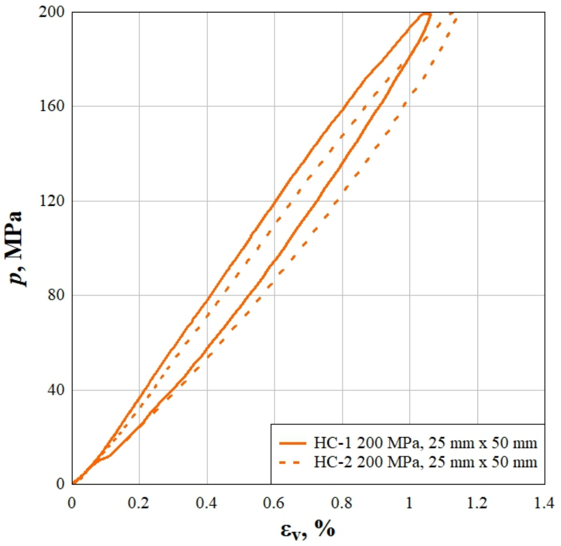

Fig. 17. Hydrostatic loading and unloading for 25 mm x 50 mm specimens up to 200 MPa mean normal stress

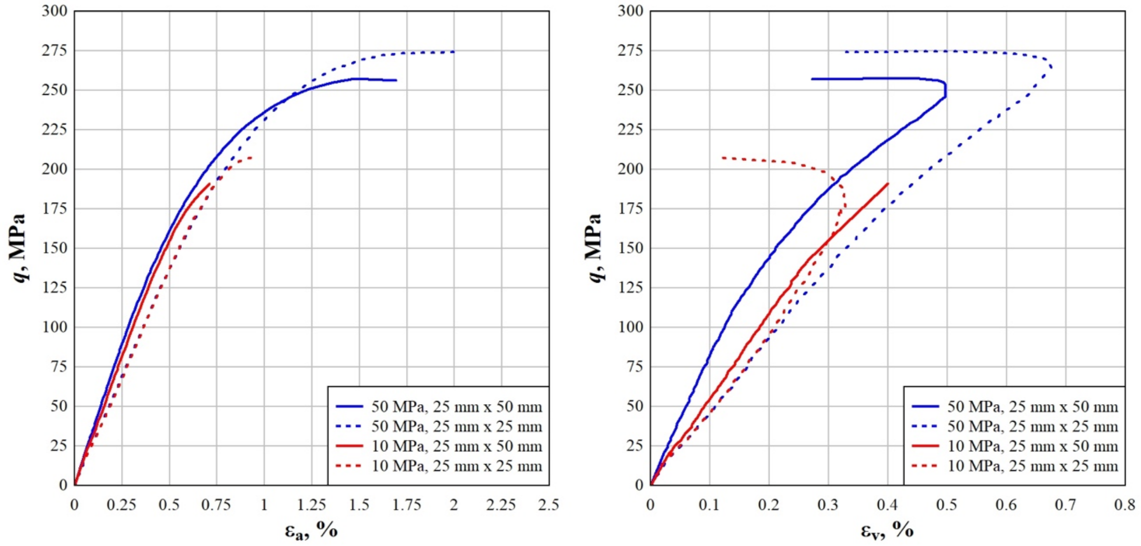

Fig. 18. Material response in terms of axial (left) and volumetric (right) strains for 25 mm x 50 mm and 25 mm x 25 mm TXC specimens at 10 and 50 MPa confining pressure

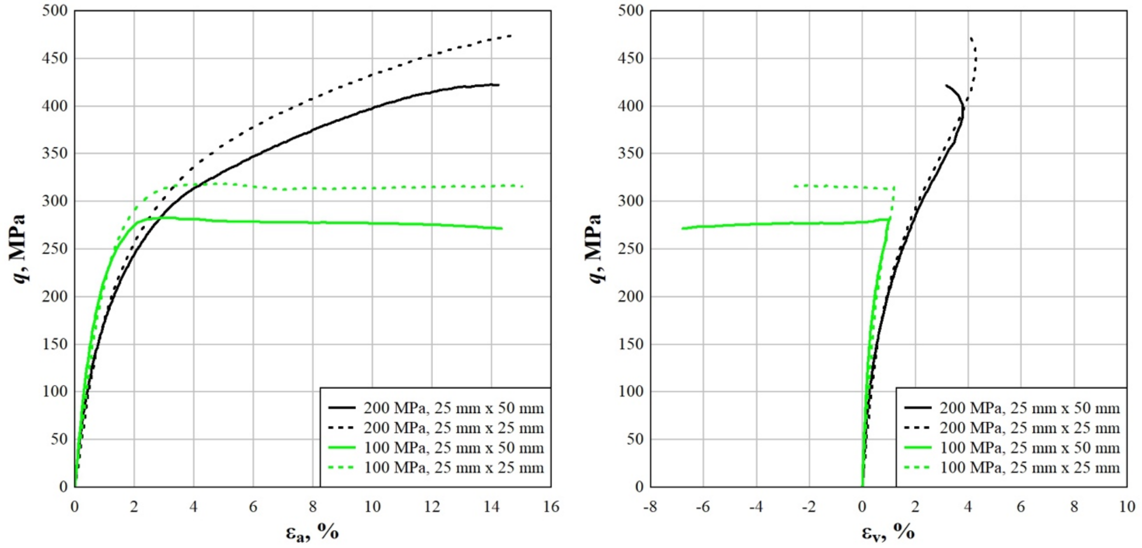

Fig. 19. Material response in terms of axial (left) and volumetric (right) strains for 25 mm x 50 mm and 25 mm x 25 mm TXC specimens at 100 and 200 MPa

For all data presented in this paper, compression is considered positive. Therefore, axial strains are reported as positive while the specimen length decreases. Similarly, a positive volumetric strain indicates a decrease in the volume of the specimen. However, note that volumetric strains are calculated based on a combination of axial and radial strain measurements. As the concrete specimen begins to fail, internal crack formation causes expansion and a measured increase in volume.

Considering **Fig. 18**, 10 MPa TXC experiments with an L/D of 2.0 exhibit an extremely brittle failure mode that is typical for unconfined compression experiments. The recovered specimens were fully fractured within the latex membrane. However, the corresponding specimens with an L/D of 1.0 experience a higher peak stress with volumetric strains decreasing near failure indicating that damage accumulation is likely more substantial as compared to the taller specimens. For the 50 MPa TXC experiments, specimens were unloaded shortly after reaching a peak stress and the recovered specimens were mostly intact with some fragmentation observed. The 50 MPa TXC data for specimens having an L/D of 1.0 exhibited a larger decrease in volumetric strains after reaching a peak volumetric strain that is likely attributed to increased damage accumulation as compared to L/D = 2 specimens. The noted discrepancies from size effects are likely a result of higher confinement stresses in the shorter specimens due to end effects.

At higher confinement pressures presented in **Fig. 19**, specimen size continues to have substantial effects on material behavior. For 100 MPa and 200 MPa TXC experiments, the tests are stopped after reaching an axial strain of 15% for the purpose of directly comparing material behavior. Note that these specimens experience a ductile failure mode and continue to have substantial load bearing capacity at axial strains beyond 15%. Prior to reaching a peak volumetric strain, changes in L/D do not appear to have any effect on volumetric response. As discussed further in sections 3.3.3 through 3.3.5, gauge-indicated volumetric strain readings are not reliable when the volumetric strains begin to move in the negative direction. However, in a relative sense, the amount of negative volumetric strain indicates the severity of non-uniform specimen deformation where the central region of the specimen expands more than the specimen ends (also referred to as barreling).

3.3.2 Limitations of Volumetric Strain Measurements

Volumetric strain measurements have limited use when approaching peak stress values since specimen cross-section is not uniform throughout the vertical axis after undergoing large axial deformations. To clearly observe non-uniform deformations, four specimens were tested to axial strains of ~30%. The material response is plotted in **Fig. 20** with volumetric strains plotted based on gauge-indicated values for ε_a and ε_r and the use of **Eq. 6**. However, this method for calculating volumetric strain is only valid if deformations are uniform throughout the vertical axis of the specimen since the radial strain is only determined at one location in the center of the specimen. To better understand the deficiencies of volumetric strain calculations, gauge-indicated readings were compared to micro-CT-indicated measurements from the full specimen volume as shown in **Table 6**. As mentioned earlier, a positive volumetric strain represents a reduction in volume, thus a negative volumetric strain should represent an increase in volume.

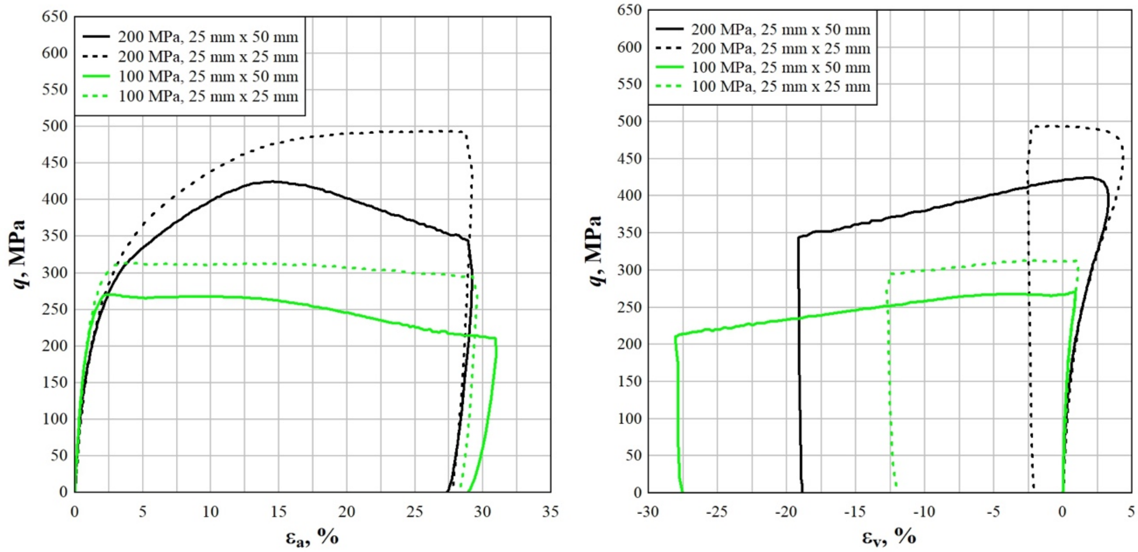

Fig. 20. Gauge indicated material response in terms of axial (left) and volumetric (right) strains for large deformations ($\varepsilon_a \cong 30\%$)

Table 6. Volumetric strain readings from in situ gauges and ex situ micro-CT measurements for specimens loaded to $\varepsilon_a \cong 30\%$.

Specimen	Gauge indicated ε_v (%)	Micro-CT indicated ε_v (%)
100 MPa, L/D = 2.0	-27.6	2.12
100 MPa, L/D = 1.0	-12.0	1.73
200 MPa, L/D = 2.0	-18.8	5.71
200 MPa, L/D = 1.0	-2.1	7.91

The large negative values for volumetric strains are clearly errant as triaxial compression does not lead to expansion within the concrete microstructure. Referencing the gauge-indicated and micro-CT indicated volumetric strain measurements in **Table 6**, note that after unloading, gauge-indicated volumetric strains differ from micro-CT results by 10-30%. Therefore, the gauge-indicated volumetric readings should be neglected at the onset of non-uniform specimen deformation. Although large deformation volumetric strain readings can be misleading due to non-uniform specimen geometry, high axial strains were required to reach a true peak stress for the 200 MPa TXC specimens with L/D = 1.0. In cases where non-uniform specimen deformation is anticipated, additional in-situ measurement locations would provide a more accurate estimate of volumetric strain history. Micro-CT provides an additional method to verify specimen volume measurements before and after loading.

3.3.3 Visual Observations from Micro-CT

For preliminary observations, full-specimen micro-CT scans were conducted on all damaged specimens using voxel sizes with a side length of 25 μm or 18 μm for specimens with a height of 50 mm or 25 mm, respectively. Prior to looking at triaxially damaged specimens, we will first observe fracture patterns in unconfined compression experiments to provide a baseline reference. For high-strength concretes, a common failure mode in unconfined compression (especially with lubricated surfaces to reduce end friction) is actually a tensile driven failure mode known as axial splitting [84,85]. The vertical cracking failure mode is defined as a Type III fracture by ASTM C39 [11]. For BBR9 specimens tested in uniaxial compression with MoS_2 lubricant applied to the specimen/platen interface, most specimens failed with a Type III columnar fracture pattern as shown in **Fig. 21**. Although less common, damage modes similar to Type II (well-formed cone on one end with vertical cracks) and Type IV (diagonal cracking) fracture patterns were observed in some cases. These specimens were preserved for micro-CT analysis by using a flexible latex membrane to contain post-fracture rubblized concrete debris.

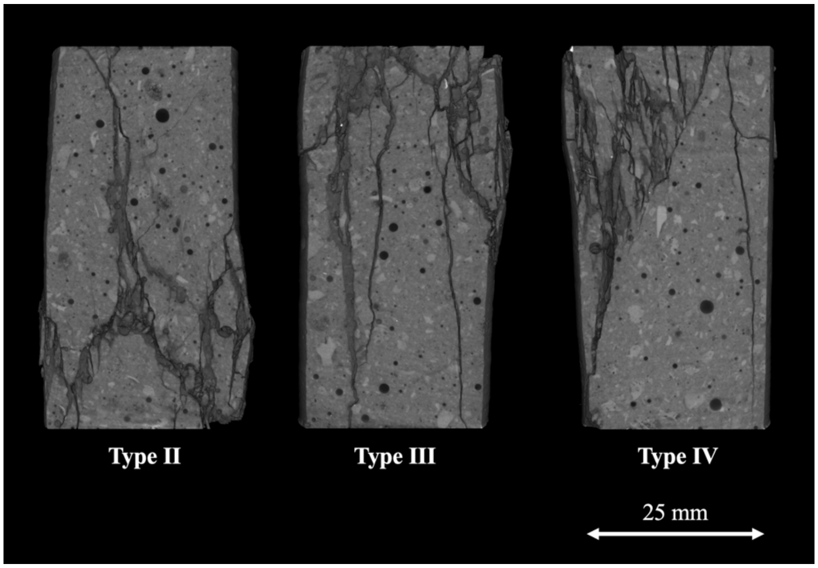

Fig. 21. Micro-CT imagery of concrete fracture patterns under unconfined compression

All specimens exposed to multi-axial stress states were isolated from the hydraulic fluid using a latex membrane that was removed prior to micro-CT analysis. Images of damaged concrete specimens from hydrostatic and triaxial loadings up to 200 MPa are presented in **Fig.**

22. Note that after a 200 MPa hydrostatic compression (HC) experiment the specimen still appears to be in a pristine condition. It is interesting to note that visually observable damage is minimal even at high hydrostatic pressure, as expected based on the data recorded in **Fig. 17**. As the shear component is introduced during triaxial compression (TXC) experiments, damage progresses through different failure modes. At 10 MPa, the concrete undergoes a brittle failure mode similar to that of the unconfined specimens. However, this low level of confinement pressure changes the fracture pattern from axial splitting to a dominant shear fracture. For the 50 MPa triaxial test, the concrete specimen still exhibits a primarily brittle (or quasi-brittle) failure mode. In this case, the crack network is more stable allowing damage to accumulate throughout the specimen as it undergoes slightly higher axial strains as compared to 10 MPa TXC experiments. For 100 MPa TXC experiments, the concrete displays a clear transition from brittle to ductile failure. The confinement pressure substantially stabilizes crack growth causing a dominant failure mode of pore collapsing and pore crushing. A slight barreling shape is also observed, which is likely attributed to additional confinement caused by end effects. Lastly, the 200 MPa triaxial specimens exhibit a failure mode that is similar to 100 MPa TXC specimens. However, at this maximum pressure, cracks are not discernable in the micro-CT images and end effects become less substantial as the specimen undergoes uniform deformation in the radial direction. Visual observations show that barreling is more pronounced in 100 MPa TXC specimens as compared to 200 MPa TXC specimens, which was predicted by the volumetric strain behavior as discussed at the end of section **3.3.1**.

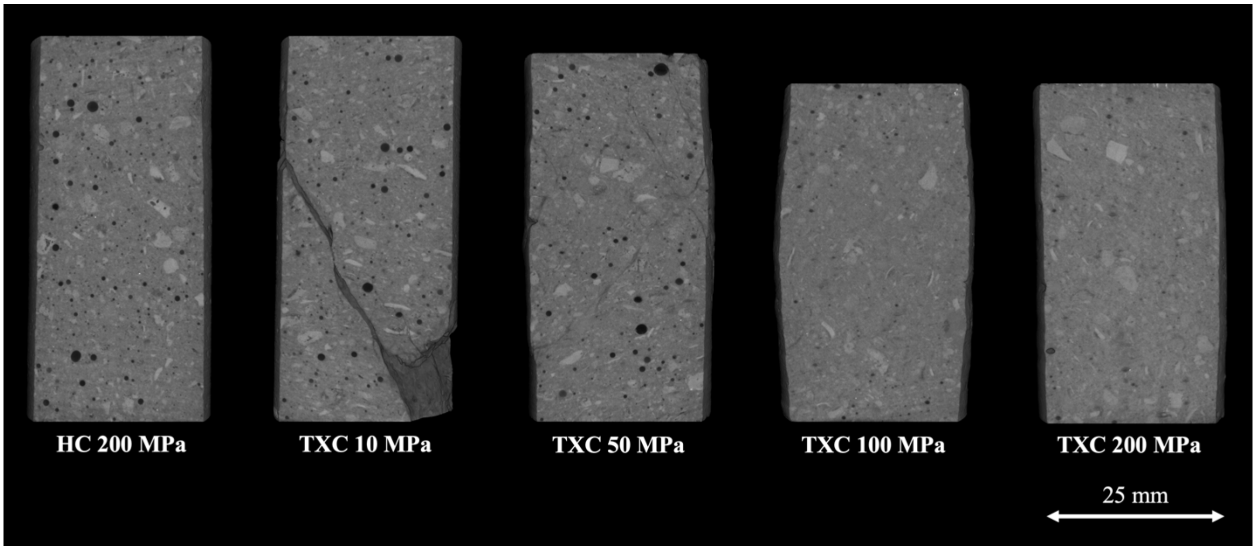

Fig. 22. Micro-CT imagery of damaged concrete after multi-axial loading

Historically, triaxial experiments conducted at the ERDC triaxial testing facility have only gone up to axial strains of 15%. In prior work, it was predicted that non-uniform deformation becomes dominant at axial strains beyond this point [74]. To further verify this claim, 100 MPa and 200 MPa TXC experiments were carried out to axial strains of ~30% to confirm deformed specimen geometries. As shown in **Fig. 23**, barreling becomes much more pronounced at higher axial strains and volumetric strain calculations based on uniform radial deformations are no longer valid as previously discussed in section **3.3.2**.

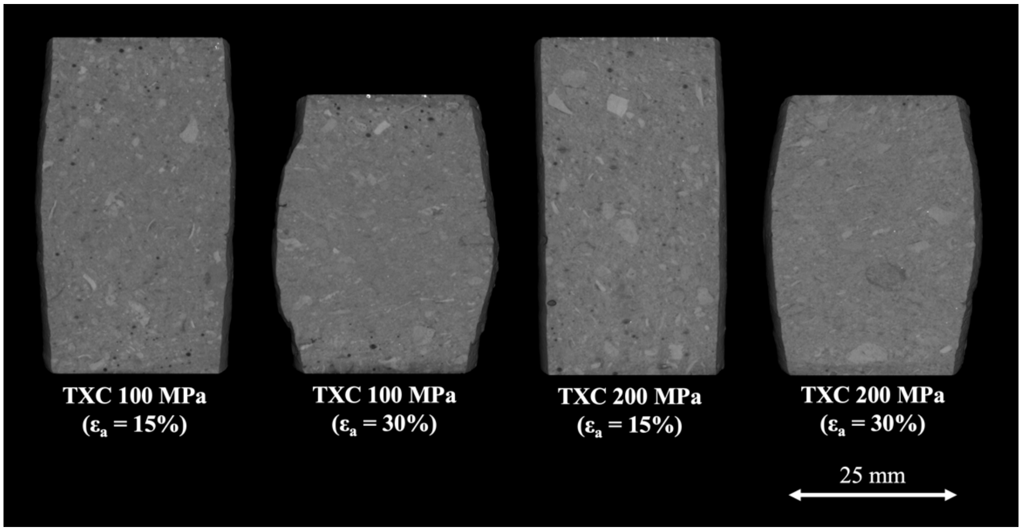

Fig. 23. Comparison of damaged geometry at high confinement pressures with increasing axial deformations

Finally, damage modes were also observed for specimens with a reduced length-to-diameter ratio (L/D). The 25 mm x 25 mm specimens (L/D = 1.0) shown in **Fig. 24** were exposed to the same testing conditions as the 25 mm x 50 mm (L/D = 2.0) TXC specimens from **Fig. 22**. As noted in section 3.3.1, there is an observed strength increase when transitioning from L/D = 2 to L/D = 1 that is likely due to end effects. Furthermore, fracture patterns also change with variations in L/D. For the 10 MPa TXC experiments, the shorter specimen is able to endure multiple shear cracks rather than a single, dominant failure plane. The 50 MPa TXC specimen appears to have a higher degree of crack saturation as compared to the taller specimen geometry. At 100 MPa, the L/D = 1.0 specimen shows visible cracks near the specimen ends that were not apparent at L/D = 2.0. However, fracture patterns at 200 MPa appear consistent between different specimen geometries. Damage isolation and quantification is further evaluated in sections 3.3.4 and 3.3.5.

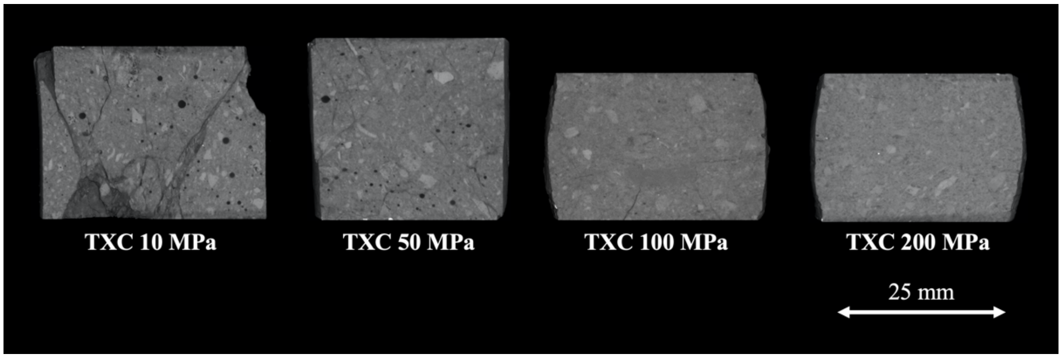

Fig. 24. Micro-CT imagery of TXC specimens with L/D = 1.0

3.3.4 Isolation of Crack Patterns for Brittle Failure Modes

As confinement pressure increases, material response transitions from a brittle failure mode (indicated by a sudden unloading after reaching a peak stress) to a ductile failure mode (indicated by material flow with significant residual load bearing capacity). However, even within the brittle failure mode, damage morphology and crack saturation can vary widely. To confirm visual observations, the scan data detailed in section 3.3.3 was used to isolate 3D damage in full specimens. For a more detailed look at microstructure, additional scans were conducted at maximum resolution (8.8 μm voxel size) and 2D sections were carefully segmented to visualize microcracking.

For 10 MPa TXC experiments, shear dominated the fracture pattern. As observed in **Fig. 25**, the 25 mm x 50 mm (L/D = 2.0) specimen failed through a single crack at an angle of ~30° from the vertical axis with a clearly defined shear plane. Taking a closer look in **Fig. 26**, a minimal number of microcracks were detected near the primary failure plane. In contrast, the 25 mm x 25 mm (L/D = 1.0) specimen shown in **Fig. 25** has multiple shear planes with crack angles ranging from 25-30° from the vertical axis. The higher resolution scan presented in **Fig. 26** reveals distributed microcracking with high concentrations surrounding primary failure planes.

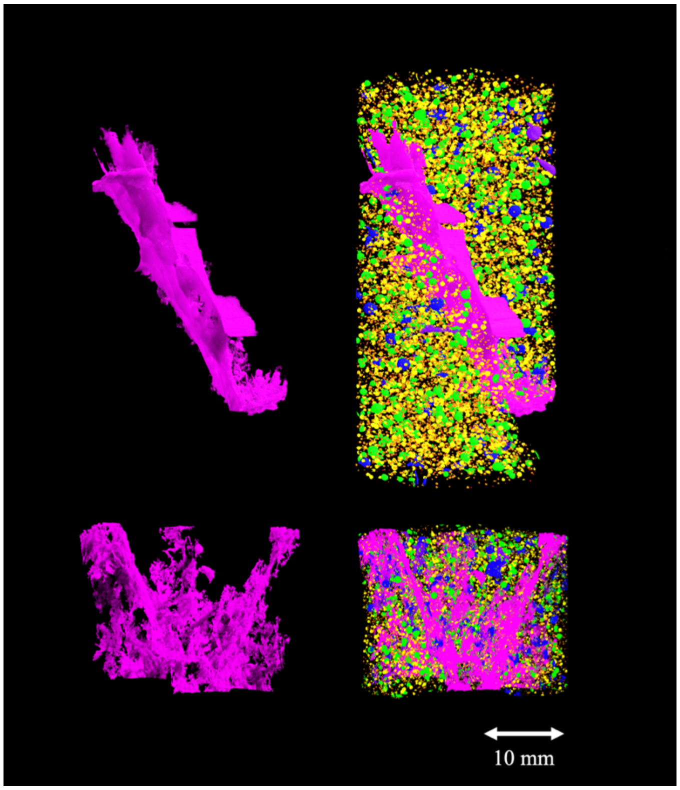

Fig. 25. Crack segmentation for 10 MPa TXC specimens with L/D = 2.0 (top) and L/D = 1.0 (bottom)

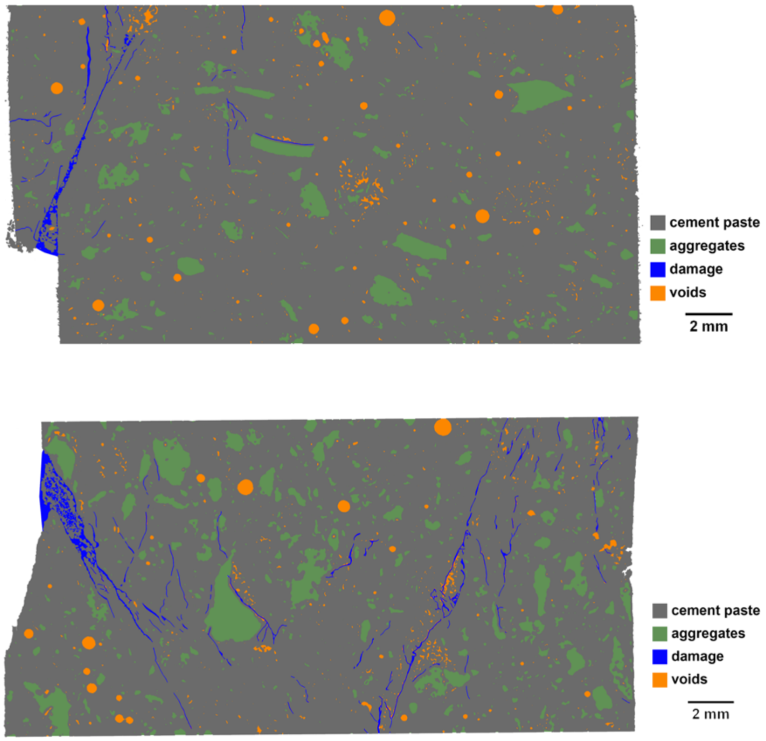

Fig. 26. Fracture patterns for 10 MPa TXC specimens with L/D = 2.0 (top) and L/D = 1.0 (bottom

As the confinement pressure increases to 50 MPa, observable damage progression continues to occur primarily through brittle fracture planes. In **Fig. 27**, the 25 mm x 50 mm (L/D = 2.0) specimen shows two intersecting shear planes at angles ranging from 25-30° from the vertical axis. Also in **Fig. 27**, the 25 mm x 25 mm (L/D = 1.0) specimen shows similar shear-cracking angles with distributed shear planes throughout the specimen. In both specimen geometries, coalescence of microcrack networks and large voids ultimately leads to brittle failure. Taking a closer look at microstructure in **Fig. 28**, it is evident that microcracks are present throughout the specimens for both geometries. Keep in mind that as crack widths become smaller, damage is more difficult to segment due to the resolution limitations of the micro-CT scanner.

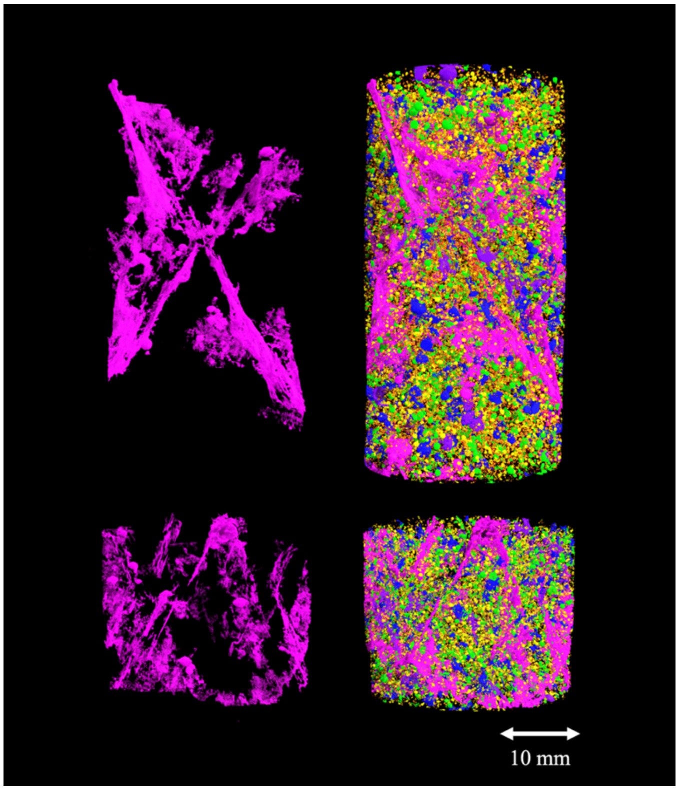

Fig. 27. Crack segmentation for 50 MPa TXC specimens with L/D = 2.0 (top) and L/D = 1.0 (bottom)

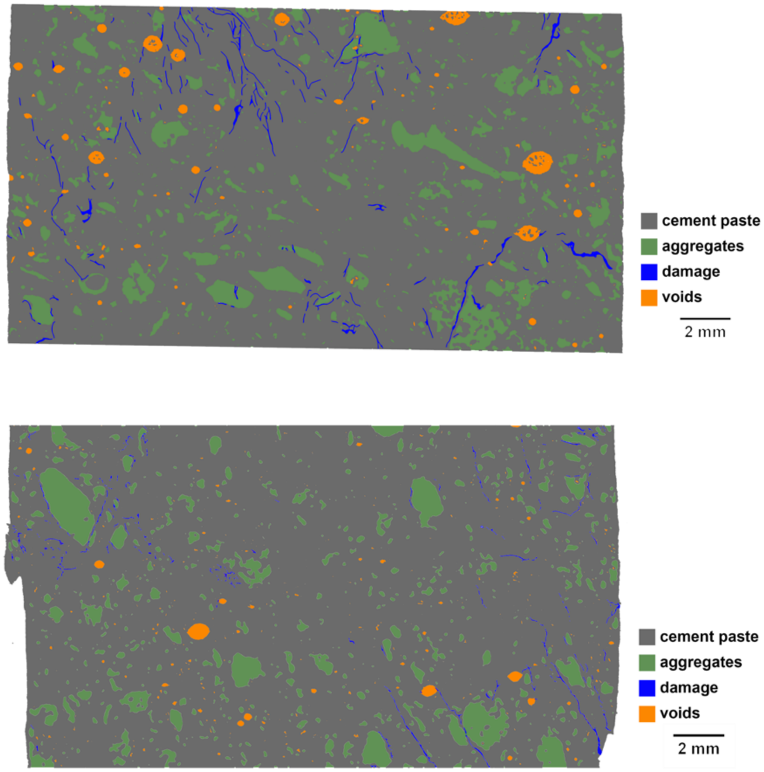

Fig. 28. Fracture patterns for 50 MPa TXC specimens with L/D = 2.0 (top) and L/D = 1.0 (bottom)

When comparing damage from unconfined compression, 10 MPa TXC, and 50 MPa TXC specimens, a stark contrast in crack patterns is observed. Although axial splitting is the primary failure mode in unconfined compression experiments, failure occurs along shear planes in triaxial experiments at confining pressures of 10 MPa and 50 MPa. Crack growth is stabilized as the level of confinement increases. This is further supported by the higher number of shear crack planes observed with reduced L/D specimens that undergo additional confinement as a result of frictional end effects. Shear plane angles remain consistently in the range of 25-30° from the vertical axis for both specimen geometries at confining pressures of 10 MPa and 50 MPa.

3.3.5 Quantifying Damage for Ductile Failure Modes

At higher confinement pressures, brittle failure modes are absent from the CT images of the deformed specimens. Instead, large axial deformation (high ductility) accompanied by significant reduction in porosity becomes prevalent, which is a hallmark for ductile failure of concrete. All porosity analysis utilized maximum resolution (8.8 μm voxel size) scans to capture pore sizes distributions. In this case, the scans focused only on the central portion of the specimen with a volume of interest (VOI) height of 14.3 mm. To visualize local variations and changes in pore structure, porosity was calculated for each cross-sectional image throughout the vertical axis of the VOI. Since the length of a specimen changes during testing, results are presented in terms of normalized axial position where "0" represents the bottom of the VOI and "1" represents the top of the VOI. **Fig. 29** presents local porosity variations for 100 MPa and 200 MPa TXC specimens after undergoing axial strains of ~15% (left) and ~30% (right).

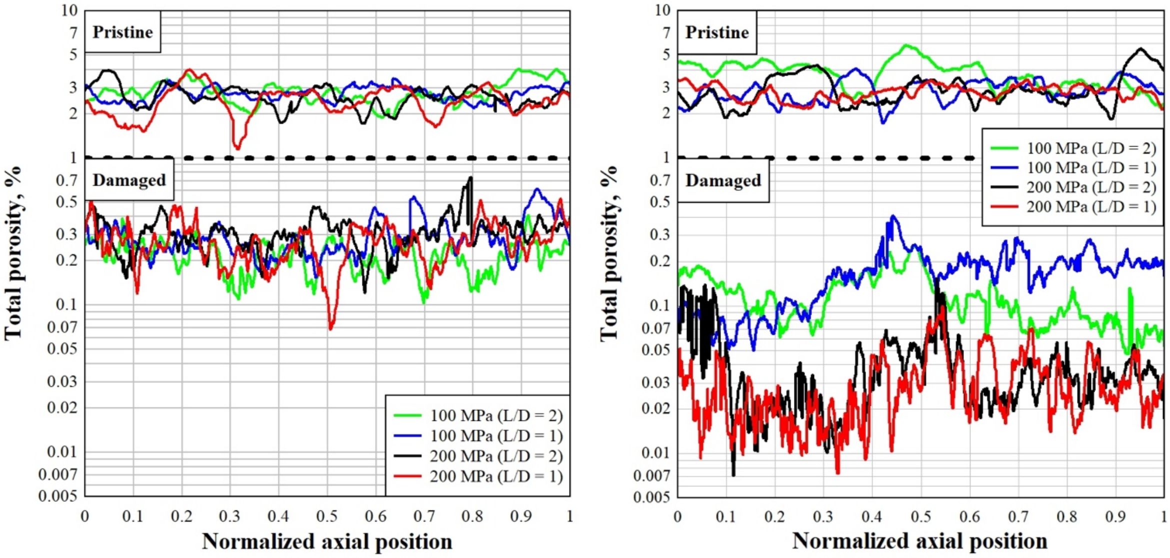

Fig. 29. Cross-sectional porosity percentages for 2D sections in terms of normalized axial position before and after ~15% (left) and ~30% (right) axial strain deformations

The variability in local porosity values for pristine specimens is an indication of the heterogeneous nature of concrete. Although cross-sectional values of porosity in pristine BBR9 specimens ranged from 1-5%, the mean total porosity was determined to be 3.01% (not accounting for porosity with a volume-equivalent sphere diameter below 50 μm). Referencing **Fig. 29**, no substantial differences were observed in terms of L/D. Specimens undergoing 15% axial strains in 100 MPa and 200 MPa TXC experiments did not show any clear discrepancies in terms of cross-sectional porosity measurements with mean values of 0.25% and 0.29%, respectively. However, at axial strains of 30%, mean porosity values were 0.14% for 100 MPa TXC specimens as compared to 0.03% for 200 MPa TXC specimens, indicating that pores are more thoroughly collapsed under higher pressure.

Porosity size distributions were also calculated in terms of volume-equivalent sphere diameters ranging from 50 μm up to 4 mm. Bin sizes started at a minimum of 50 μm to ensure that a sufficient number of voxels (8.8 μm) were used to resolve individual pore morphologies. Starting with the smallest bin size, each subsequent bin size was identified using a multiplier of 1.1 until reaching a maximum bin size of 3.64 mm. The resulting pore size distributions were then plotted in a log-log format as shown in **Fig. 30** to clearly visualize distribution data for the full range of pore sizes.

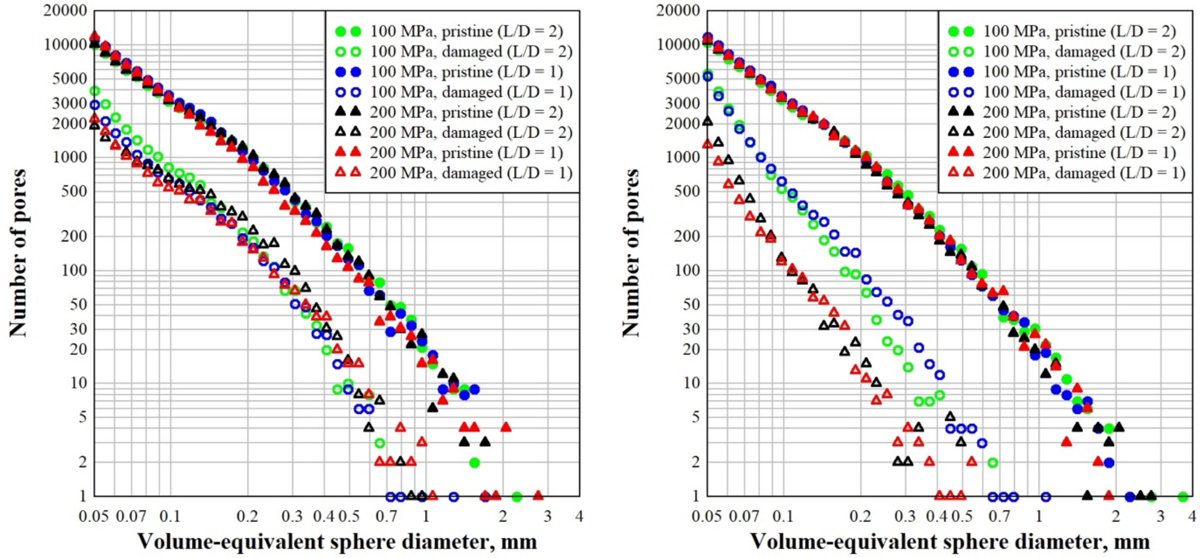

Fig. 30. Void analysis in terms of volume-equivalent sphere diameter before and after ~15% (left) and ~30% (right) axial strain deformations

Pore size distributions for pristine specimens were observed to be quite consistent considering the heterogeneous nature of concrete. Similar to observations made for **Fig. 29**, the pore size distributions are quite similar for all damaged specimens undergoing axial strains of ~15%. However, it does appear that the 200 MPa TXC tests provided slightly more compaction for damaged volume-equivalent sphere diameters ranging from 50-120 µm. Also following observations from **Fig. 29**, samples undergoing axial strains of ~30% had more severe pore collapse (for all damaged pore sizes) in 200 MPa TXC specimens as compared to 100 MPa TXC specimens. As barreling becomes more pronounced at high axial strains, 100 MPa TXC specimens exhibit relatively larger radial deformations while the higher confinement in 200 MPa TXC specimens continues to drive the additional compaction of remaining void structures.

Although reducing L/D has been shown to increase peak stress values, changes in L/D do not show substantial differences for ductile failure modes.

Since L/D was determined to have negligible effects on pore size distributions, visualization efforts were solely focused on specimens with a traditional L/D of 2.0. Each image in **Fig. 31** and **Fig. 32** depicts a specimen with pristine porosity shown on the left half and damaged porosity shown on the right half for a given VOI. Pores are color coded by major diameter to conveniently distinguish individual pores and sizes.

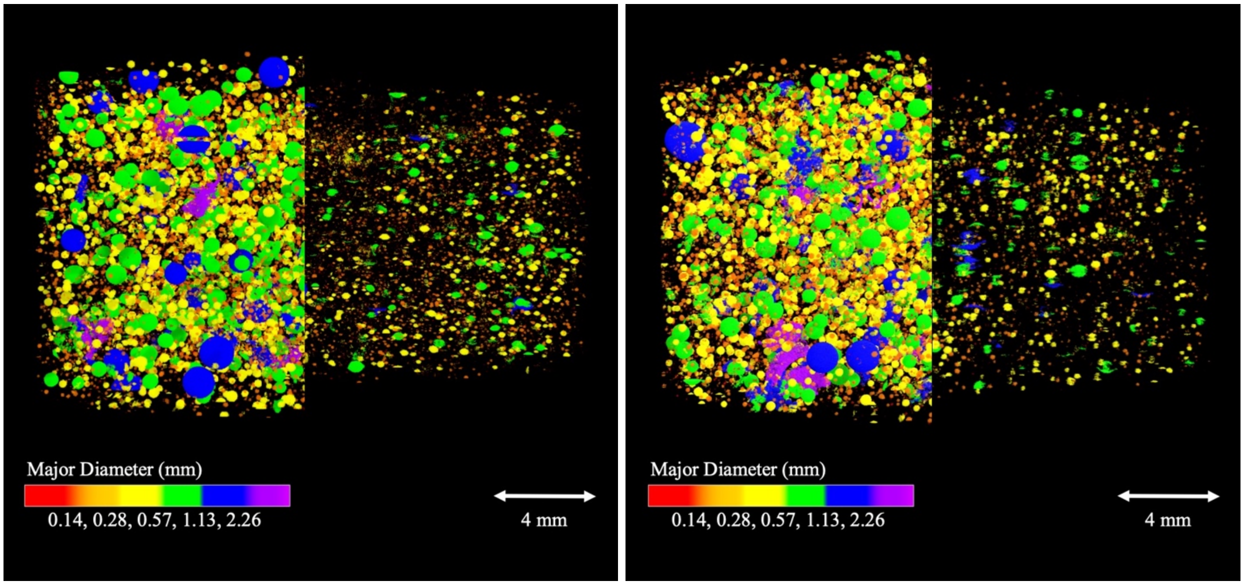

Fig. 31. Void structure for pristine and damaged 100 MPa (left) and 200 MPa (right) TXC specimens after ~15% axial strain deformations

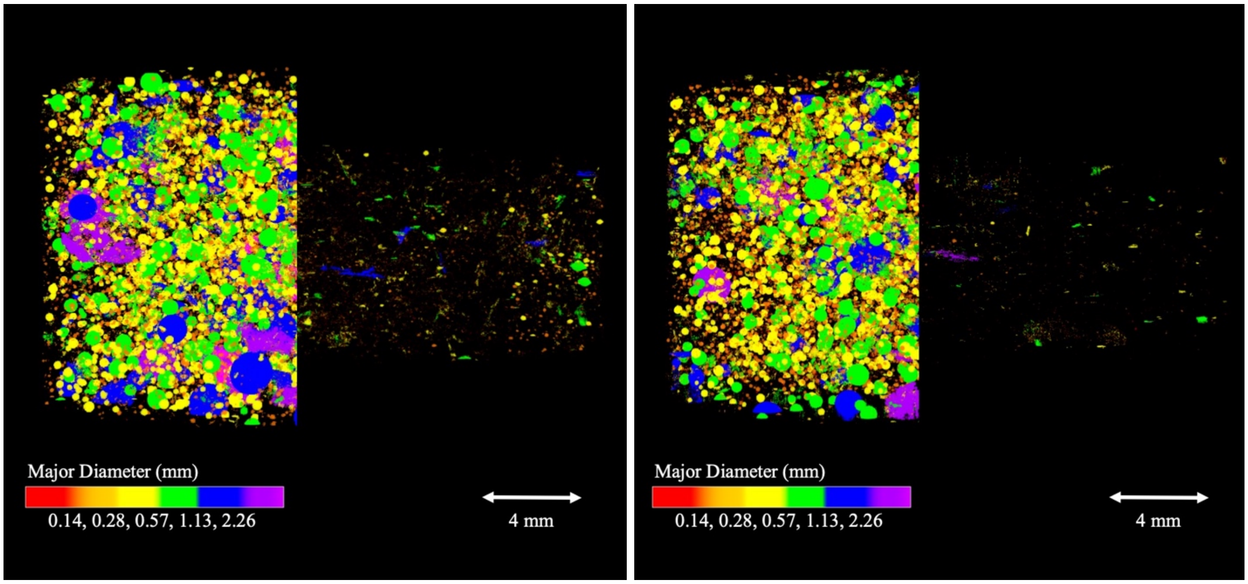

Fig. 32. Void structure for pristine and damaged 100 MPa (left) and 200 MPa (right) TXC specimens after ~30% axial strain deformations

In pristine specimens, porosity is nearly spherical resulting in a major diameter that is approximately equivalent to the volume-equivalent sphere diameters presented in **Fig. 30**. However, damaged pores are more clearly distinguished by major diameter since the pore geometry is severely flattened after axial loading. The 3D rendering of damaged pore structures in **Fig. 31** reveals similar void structures for 100 MPa and 200 MPa TXC specimens undergoing axial strains of ~15%. However, discrepancies are observed after ~30% axial strain deformations in **Fig. 32** with the 200 MPa TXC specimen having a smaller number of observable pores as compared to the 100 MPa TXC specimen. As expected, the damaged VOI shrinks in height and expands radially as compared to the pristine VOI. The qualitative pore structure images in **Fig. 31** and **Fig. 32** provide visual evidence that is consistent with quantitative porosity measurements presented earlier in **Fig. 29** and **Fig. 30**

3.3.6 Residual Strength Measurements

Residual strength experiments were conducted on specimens that underwent a ductile failure mode to provide a means for correlating pore collapse (as presented in section 3.3.5) to a physical measurement of strength degradation resulting from microstructural damage. Residual strength measurements were obtained for all triaxially damaged 100 MPa and 200 MPa TXC specimens by performing destructive unconfined compression experiments. As a reference for comparison, the mean unconfined compressive strength of pristine BBR9 specimens with LD = 1 and L/D = 2 was previously reported to be 140.7 MPa and 130.8 MPa, respectively [74]. Residual strength measurements for damaged specimens are reported in **Table 7**. Stress measurements were calculated by using the largest specimen diameter in the center of each triaxially damaged specimen. Residual strength percentages were calculated by dividing the residual strength by the mean strength for pristine specimens having the same L/D.

Table 7. Residual strength measurements

Confining Pressure, MPa	Axial Strain, %	Length-to-diameter ratio (L/D)	Residual Strength, MPa	Residual Strength, %
100	~15	1	49.9	35.5
100	~15	2	56.1	42.9
100	~30	1	47.7	33.9
100	~30	2	31.8	24.3
200	~15	1	67.7	48.1
200	~15	2	69.9	53.4
200	~30	1	48.9	34.8
200	~30	2	40.8	31.2

After undergoing axial strains of ~15%, 100 MPa and 200 MPa TXC specimens retain approximately 40% and 50%, respectively, of their pristine strength capacity. Even after undergoing axial strains of ~30%, 100 MPa and 200 MPa TXC specimens retain approximately 30% of their pristine strength capacity. These residual strength measurements indicate that the cohesive strength of TXC specimens undergoing a ductile failure mode remains substantial and should be considered when defining a damage variable.

3.4 Conclusions

X-ray microtomography was used to analyze both pristine and damaged high-strength concrete specimens to characterize damage modes and size effects under hydrostatic and triaxial stress states. Specimens with a diameter of 25 mm and an L/D of either 1 or 2 were evaluated to determine damage features under triaxial confinement pressures of 0, 10, 50, 100 and 200 MPa. The conclusions below are based on the findings of this research

- Axial splitting is the dominant failure mode for BBR9 high-strength concrete specimens under unconfined compression.
- Deformations at hydrostatic pressures up to 200 MPa are fully reversible. Although the confining pressure is significant, a shear component is required to initiate plastic deformation.
- Volumetric strain measurements can be recorded using a centrally located LVDT-based lateral deformeter, noting that signals are only valid up to the point where volumetric strains turn negative due to non-uniform specimen deformation. Removable gauge mounts are critical for conducting micro-CT scans on damaged triaxial specimens.
- Micro-CT provides an accurate approach for measuring ultimate volumetric strains for irregularly shaped damaged specimens.
- From visual observations, a transition in damage mode is noted as confining pressure increases: 10 MPa – brittle failure through a single crack with a predominant shear

failure, 50 MPa – quasi-brittle failure with distributed microcracks ultimately leading to shear failure, 100 MPa – ductile failure with minimal microcracks and damage primarily consisting of pore collapse, 200 MPa – ductile failure with no discernable cracking and damage observed through pore collapse and crushing.

- At axial strains of 30%, specimen geometry presents a severe barreling shape leading to substantial variations in cross-sectional area throughout the specimen. However, at axial strains of 15%, the observed variations in cross-sectional area are minimal.
- Brittle and quasi-brittle fracture modes for 10-50 MPa TXC experiments result in shear planes at angles ranging from 25-30° from the vertical axis.
- As specimens undergo triaxial compression at 100-200 MPa, spherical voids are flattened into ellipsoidal morphologies as total porosity percentages continue to reduce.
- After undergoing 15% axial strains, individual object analysis shows that specimens damaged under 200 MPa TXC include a more noticeable reduction of pore sizes in the range of 50-120 microns as compared to 100 MPa TXC specimens.
- After undergoing 30% axial strains, porosity size distributions are noticeably lower for all pore sizes undergoing 200 MPa TXC as compared to 100 MPa TXC. This observation can be explained by the fact that the 200 MPa TXC specimens undergo a more complete pore collapse with smaller radial strain measurements for a given axial deformation as compared to the 100 MPa TXC specimens.
- After undergoing axial strains of ~15-30%, triaxially damaged specimens in a ductile failure mode maintain a residual unconfined compressive strength that is ~30-50% of the pristine strength

For axial strains up to 15%, the damage modes under the same confining pressure were very similar regardless of the change in length-to-diameter ratio (L/D). This observation indicates that specimens with a reduced L/D could be reasonably used to assess mechanical properties for high-strength concrete, although perceived strength increases as a result of end effects should still be considered. The suitability of L/D = 1 specimens is encouraging for experimental methods using a triaxial Kolsky bar where the specimen length must be restricted to ensure a constant strain rate deformation under dynamic stress equilibrium.

CHAPTER 4:

HIGH-RATE RESPONSE

4.1 Introduction

In both civilian and military applications, engineers attempt to design structures that can withstand extreme events such as blast, fragmentation, and penetration. However, it can be challenging to predict material behavior under complex stress states that occur during a dynamic loading event. Continuum models for cementitious materials [1-3,5] are extensively used in explicit hydrocodes [6,7] to predict material behavior under dynamic loading events. Quasi-static triaxial experiments have been widely used to develop failure surfaces and define model parameters for a variety of cementitious materials [42,81,86,87], while the rate-effect parameters for concrete are typically acquired through unconfined Kolsky bar experiments [65,88,89]. Nonetheless, a simultaneous characterization of rate effects under triaxial loading conditions presents a substantial knowledge gap for cementitious materials.

The Kolsky bar, or split-Hopkinson pressure bar, was named after the pioneers who developed controlled dynamic experiments based on the principles of wave mechanics [90-92]. Over the years, the technique has been utilized to determine the high-rate properties of concrete in compression [93-98], split tension [99,100], direct tension [101-103], and spall [104-107]. The method aims to achieve a constant strain rate deformation while the specimen is loaded under dynamic stress equilibrium, which can be challenging for brittle materials [108,109]. Pulse shaping is required to achieve these conditions [110-113]. The shape of the incident pulse is tailored through the use of a deformable "tip" material placed between the striker and the incident bar, known as a pulse shaper, which is typically made of annealed copper for the testing of brittle materials [114-116].

The Kolsky bar technique has also been adapted to induce complex stress states in the test specimens. The simplest experimental setup is achieved by using a mechanical sleeve to confine a specimen during the Kolsky bar experiment [117,118]. However, this process can cause difficulty in data interpretation because of the unknown frictional effects between the sleeve and the specimen. The method is also incapable of producing a constant radial stress throughout the experiment. Other methods have used a pressurized chamber for radial stress but implemented an actuator on the end of the bar to provide axial stress [119,120]. However, these designs result in an imbalanced load state where the system undergoes a reaction moment from the axial loading. This causes issues with non-normal impacts of the striker, bending of the bars, susceptibility to buckling, and increased friction in guide bushings [121].

To achieve a better defined radial stress state, i.e., confinement pressure, a more sophisticated confinement chamber system was designed for Kolsky bars [121]. This system utilizes a symmetric tie-rod configuration to eliminate the possibility of a reaction moment in the system. Additionally, two separate chambers are used for radial and axial loads but operate on the same hydraulic system to ensure uniform pressure loading throughout the system. Constant radial confinement is maintained throughout the test by providing sufficient fluid volume for dissipation of pressure changes due to volume changes in the specimen. Lastly, this design allows for the use of pulse shapers to develop the appropriate loading wave to maintain constant strain rates during testing. A schematic of the triaxial Kolsky bar is presented in

Fig. 33.

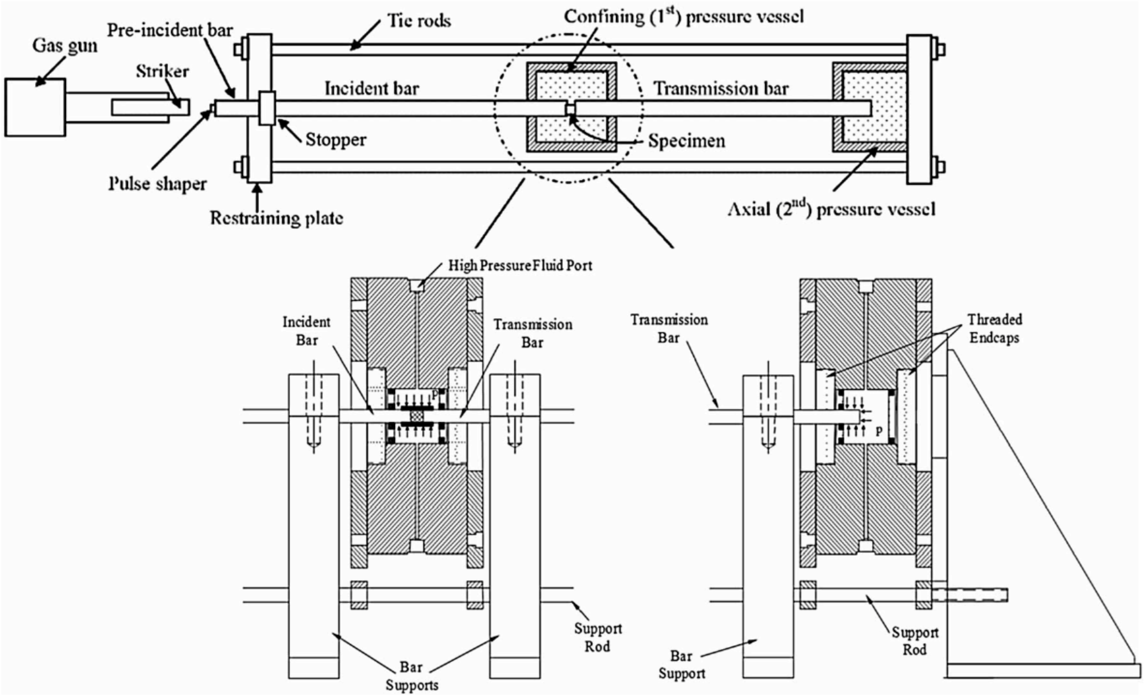

Fig. 33: Schematic of the triaxial Kolsky bar with hydraulic confinement chambers [122].

Since the introduction of this triaxial Kolsky bar system, it has been applied to the testing of several materials. Dynamic confined behavior of sand [123-127], glass [122,128], rock [129], and concrete [130] has been investigated by using a 19-mm-diameter triaxial Kolsky bar system. Limestone has also been evaluated by using a 12.7-mm-diameter triaxial Kolsky bar [121]. However, for heterogeneous composites, specimen size becomes a critical issue due to the large constituent phases. Therefore, a large-diameter (~50 mm) triaxial Kolsky bar system is needed to minimize size effects for cementitious materials. Prior work analyzed the effects of specimen geometry under triaxial loading to determine that a cylindrical specimen with a diameter and height of 25.4 mm (L/D = 1:1) can be used to characterize the bulk behavior of high-strength concrete with a maximum particle size of 4.75mm [74]. To the best of the authors' knowledge, identical specimen geometries have not been evaluated at both quasi-static and dynamic strain rates under triaxial loading conditions.

4.2 Materials and Methods

4.2.1 Material

All testing was performed on BBR9 high-strength concrete, which is detailed in literature [35,65,74,79-81]. A mixture proportion for BBR9 is presented in **Table 1**. The self-consolidating material was developed based on particle packing methodologies while using a central composite design of experiments to reduce the number of trial mixtures [78]. Constituent materials include manufactured limestone sand, type I/II portland cement, grade-100 ground granulated blast-furnace slag (GGBFS), undensified microsilica (silica fume), polycarboxylate-ether-based high-range water-reducing admixture (HRWRA), and tap water. Sand is the largest constituent material with a maximum particle size of 4.75 mm.

Table 8. Mixture proportions for BBR9 high-strength concrete

Constituent	Mixture Proportions, by Weight	Specific Gravity
Cement (Type I-II)	1.00	3.15
Manufactured limestone sand	2.25	2.57
Slag	0.60	2.95
Microsilica (silica fume)	0.26	2.20
Tap water	0.37	1.00
High-range water-reducing admixture	0.03	1.20

4.2.2 Specimen Preparation

Following guidance of ASTM C 42 [40], 25.4-mm-diameter concrete cores were taken from a bulk sample. The resulting cores were cut with a precision diamond blade to a length of approximately 30 mm. A PR Hoffman PR-1 85T double-sided planetary lapping machine was used to achieve a final length of 25.4 mm with parallelism and flatness within 25 μm. A pristine BBR9 specimen is shown in **Fig. 2**.

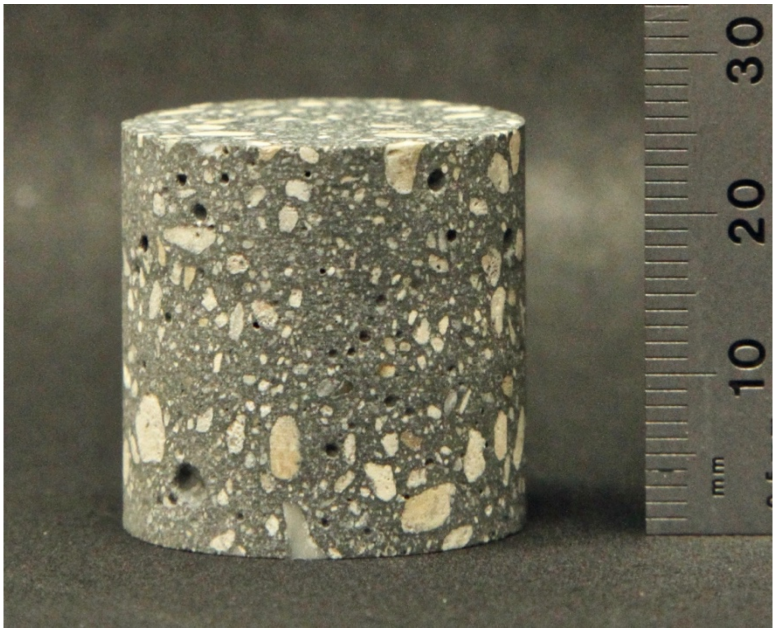

Fig. 34. Cylindrical BBR9 high-strength concrete specimen.

4.2.3 Quasi-static Triaxial Compression

Although the primary focus of this paper is the acquisition of pressure-dependent dynamic properties for concrete using a novel triaxial Kolsky bar system, a quasi-static baseline is required for the development of rate-effect parameters. A detailed description of quasi-static test methods, results, and size effects was presented in a prior publication [74]. The quasi-static triaxial test equipment is also detailed in the literature [4,42,44]. To provide a brief summary, the triaxial loading device uses sealed cylindrical specimens with hydrostatic loading applied by fluid pressure. A hydraulic ram then contacts the specimen to apply axial loading. A light coating of MoS_2 lubricant is applied at the specimen/platen interface to reduce the influence of frictional end effects.

Triaxial experiments frequently report data in terms of principal stress difference and mean normal stress. Previously reported stress values [74] were in terms of true stress, as they were based on the changing cross-sectional area of the specimen. However, axial engineering stress will be employed in the current study to make a direct comparison to triaxial Kolsky bar experiments. The principal engineering stress difference (q_{eng}) is defined by the difference between axial engineering stress (σ_a, or σ_3) and radial stress (σ_r, or σ_1 and σ_2), as shown in **Eq. 7**. Mean normal stress (p) is defined as the average of applied principal stresses, as shown in **Eq. 8**.

Eq. 7:

$$q_{eng} = \sigma_a - \sigma_r$$

Eq. 8:

$$p = \frac{(\sigma_1 + \sigma_2 + \sigma_3)}{3} = \frac{(\sigma_a + 2\sigma_r)}{3}$$

4.2.4 Unconfined Kolsky Bar

Although unconfined Kolsky bar experiments have been well documented in the literature for a wide variety of cementitious materials, it is critical to determine dynamic unconfined BBR9 properties by using the geometry specified in this work. Note that specimens in the literature that show evidence of satisfying stress equilibrium and constant strain rate requirements typically have a diameter below 25 mm and/or a length-to-diameter ratio (L/D) below 1.0. Although a larger L/D is preferred for standardized measurements of the quasi-static compressive strength of concrete, achieving dynamic stress equilibrium becomes more challenging for longer specimens. Meanwhile, the specimen diameter must be large enough to be representative of the bulk material. The unconfined Kolsky bar utilized C300 maraging steel bars of 50.8-mm diameter with the striker, incident bar, and transmission bar having lengths of 0.46 m, 3.05 m, and 1.52 m, respectively. Annealed copper sheets were utilized to fabricate annular pulse shapers

4.2.5 Triaxial Kolsky bar

The U.S. Army Engineer Research and Development Center (ERDC) recently acquired a large-diameter triaxial Kolsky bar that was designed and manufactured by Dynamic Systems & Research Corporation (DSR). In addition to the traditional Kolsky bar setup, this bar incorporates a confinement system that is a larger version of the optimized design shown in

Fig. 33. The confinement system utilizes kerosene as a medium to apply hydrostatic fluid pressures up to 200 MPa. A radial confinement chamber, located between the incident and transmission bars, provides fluid pressure around the specimen. Similarly, an axial confinement chamber is located at the end of the transmission bar, providing axial loading through the specimen-bar interfaces. A reaction structure is created by using four tie rods (38.1-mm diameter) located in a symmetric pattern with the incident/transmission bars centrally located to eliminate bending stresses. Both confinement chambers and the tie rod system are shown in **Fig. 35**. The C300 maraging steel bars have a diameter of 50.8 mm with the strikers having lengths of 0.46 m or 0.61 m, while the incident bar and transmission bar are 2.44 m in length.

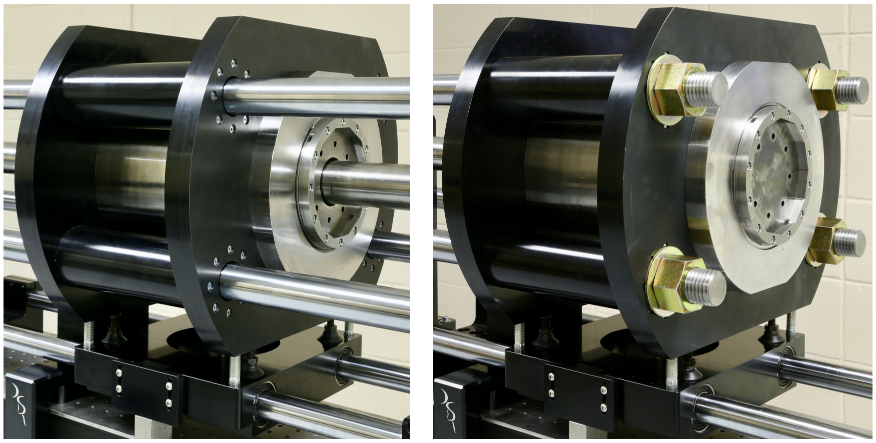

Fig. 35. Confinement chambers for applying fluid pressure in the radial (left) and axial (right) directions.

A uniform hydrostatic pressure loading is achieved through a high-pressure air-driven liquid pump that simultaneously pressurizes the radial and axial chambers by using kerosene. The dynamic axial loading is then applied in a typical fashion for Kolsky bar experiments. For a successful experiment, it is critical that the specimen is sealed to prevent confining fluid from penetrating both the specimen itself and the specimen-bar interface. The final specimen installation method consists of applying a small radius of J-B WaterWeld epoxy to eliminate the sharp transition from the 25.4-mm-diameter specimen to the 50.8-mm-diameter bar. A latex triaxial membrane is then slid over the specimen, overlapping the previously installed epoxy. Lastly, another layer of WaterWeld epoxy is used to cover the ends of the triaxial membrane and is feathered across the full diameter of the bar. To minimize the influence from the epoxy, tests were conducted after a 1-hour cure time while the epoxy remained in a soft malleable state. A picture of the final specimen is shown in **Fig. 36**. Note that a small piece of electrical tape was periodically added around the membrane to squeeze out lingering air bubbles.

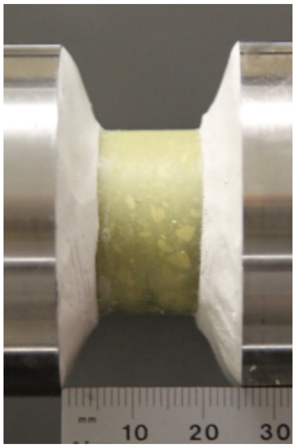

Fig. 36. An installed triaxial test specimen.

To properly interpret data from triaxial Kolsky bar experiments, it is important to note that the static offset (preload) must be removed from dynamic data analysis as described by Chen and Song [131]. The offset correction is required because the static preload is lost when the bar separates from the stopper shortly after impact. As the stopper reengages with the incident bar, a secondary loading wave (also known as the detachment wave) is observed. To further illustrate the impact of the detachment wave, **Fig. 37** provides original test signals at two locations on the incident bar and one location on the transmission bar.

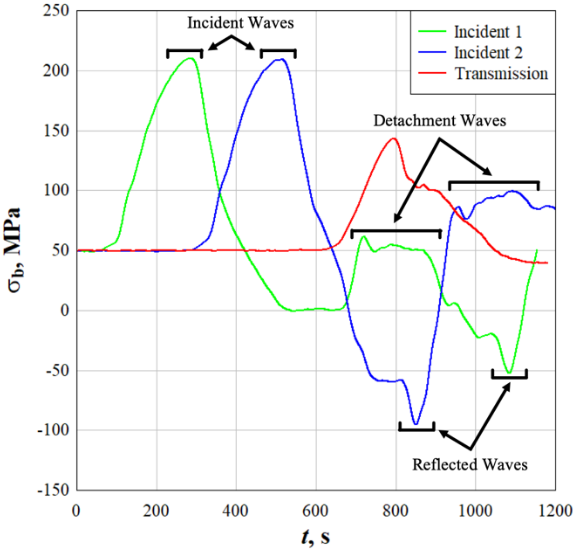

Fig. 37. Original test signal in the form of bar stress under 50 MPa confining pressure.

Prior to the collection of data, a hydrostatic pressure is applied (50 MPa for the experiment shown in **Fig. 37**). The test signal from the first strain gauge location on the incident bar shows that it is possible to have the detachment wave occurring between the incident and the reflected waves. However, by recording the signal at the second strain gauge location on the incident bar (closer to the specimen), the reflected wave can be captured prior to the arrival of the detachment wave. By comparing the two signals from the incident bar, the reflected waves have an offset in the amount of the hydrostatic prestress (~50 MPa). Therefore, a proper understanding of the unloading and loading of static prestress is critical for data analysis. A more thorough discussion on the detachment wave is provided in the literature [132].

As demonstrated in **Fig. 38**, stress equilibrium is satisfied under 10 MPa confining pressure. At higher pressures, stress equilibrium is more easily satisfied due to increased specimen ductility and longer loading times. However, it is difficult to verify stress equilibrium at high confining pressures due to overlapping of the detachment wave and the reflected wave [132]. Therefore, subsequent data analysis uses the stress equilibrium assumption to calculate the reflected wave as the difference between the incident and transmission waves. By utilizing this approach, data processing no longer requires a means to separate overlapping signals from the detachment wave and the reflected wave. Equations 9-11 were used to calculate specimen stress (σ_s), specimen strain rate history ($\dot{\varepsilon}_s$), and specimen strain (ε_s), where A_b, A_s, E_b, C_b, and L_s are the cross-sectional area of the bar, the cross-sectional area of the specimen, the Young's modulus of the bar, the wave speed in the bar, and the specimen length, respectively, and ε_T and ε_R are the transmitted and reflected waves.

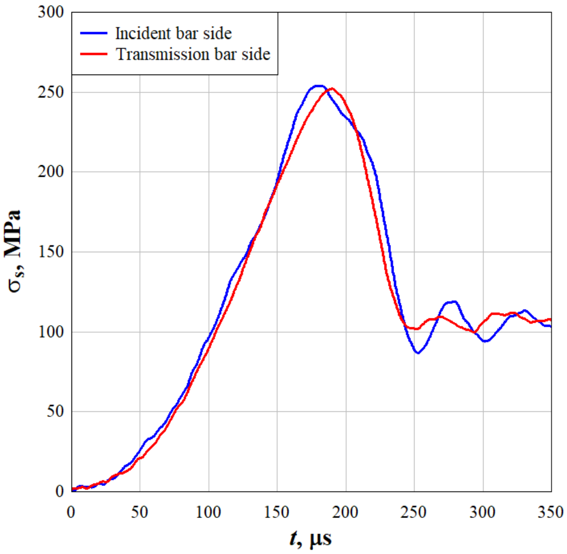

Fig. 38. Demonstration of stress equilibrium for tests under 10 MPa confining pressure.

Eq. 9: $$\sigma_s = \frac{A_b}{A_s} E_b \varepsilon_T$$

Eq. 10: $$\dot{\varepsilon}_s = -2\frac{C_b}{L_s}\varepsilon_R$$

Eq. 11: $$\varepsilon_s = -\frac{2C_b}{L_s}\int_0^t \varepsilon_R dt$$

4.3 Results and Discussion

4.3.1 Unconfined Dynamic Response

Cylindrical BBR9 specimens (25 mm x 25 mm) were evaluated for dynamic unconfined compressive strength ($\sigma_r = 0$). To achieve a constant strain rate, an annealed copper pulse shaper with an annular geometry was implemented having a thickness, outer diameter, and inner diameter of 1.59 mm, 25.4 mm and 19.1 mm, respectively. Between the specimen-bar interfaces, MoS_2 lubricant was applied to reduce end friction effects. Five replicate experiments are shown in **Fig. 39** with a mean unconfined compressive strength of 249.6 MPa. The average strain rate history is also plotted in **Fig. 39** to highlight the constant strain rate loading at 70 s^{-1}, which remains constant until the specimen fails.

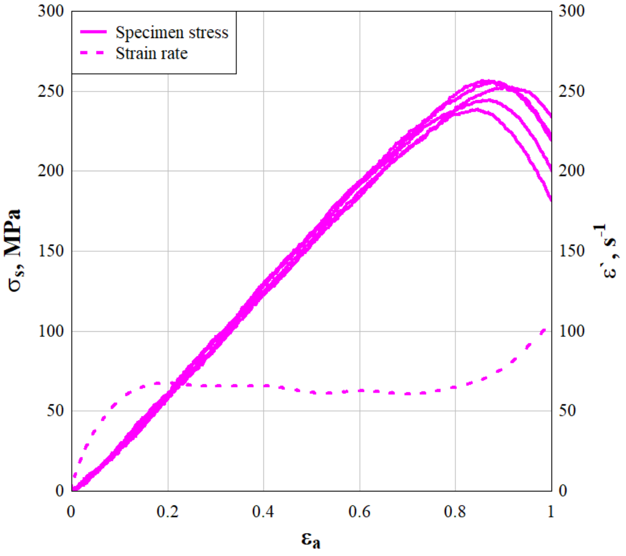

Fig. 39. Unconfined dynamic compressive response of BBR9 and strain rate history

For the most direct comparison, quasi-static experiments were conducted using the same specimen size and lubricant as those of dynamic experiments. From prior results [74], the mean quasi-static unconfined compressive strength of cylindrical BBR9 specimens was determined to be 140.7 MPa at 10^{-5} s^{-1}. Subsequently, the dynamic increase factor (DIF) can be calculated by dividing the dynamic strength by the quasi-static strength, yielding a DIF of 1.77.

4.3.2 Confined Dynamic Response

4.3.2.1 Pulse Shaping

In contrast to pulse shaping for unconfined experiments, the desired loading wave for dynamic triaxial testing is no longer linear-elastic as the failure mode of concrete transitions from brittle to ductile. However, the difference between the incident and the transmission waves must remain constant to achieve a constant strain rate deformation. Preliminary experiments were conducted at each confinement pressure to determine the approximate profile of the transmitted wave. Subsequently, pulse shaping experiments were performed to achieve the appropriate wave shape, strain rate, and amplitude required for constant strain rate deformation at each level of confining pressure. All pulse shapers were fabricated from various thicknesses of annealed copper sheets. Specifications for all pulse shaper designs are presented in **Table 9** and visually depicted in **Fig. 40**.

Table 9. Pulse shaper specifications.

			Primary Pulse Shaper				Secondary Pulse Shaper			
Confinement Pressure (MPa)	Striker Length (cm)	Tank Pressure (kPa)	QTY	Thickness (mm)	OD (mm)	ID (mm)	QTY	Thickness (mm)	OD (mm)	ID (mm)
10	45.7	138	1	1.59	25.4	19.1	---	---	---	---
50	45.7	193	1	2.36	28.6	12.7	3	0.305	4.76	---
100	45.7	241	1	1.59	28.6	12.7	1	0.071	22.2	19.1
200	61.0	448	1	0.81	31.8	19.1	---	---	---	---

Fig. 40. Pulse shapers for confinement pressures of (left to right) 10 MPa, 50 MPa, 100 MPa, and 200 MPa.

4.3.2.2 Triaxial Kolsky Bar Experiments

Triaxial Kolsky bar experiments were conducted at confinement pressures of 10 MPa, 50 MPa, 100 MPa, and 200 MPa. Five replicate specimens were tested at each level of confining pressure. **Table 10** provides a summary of experimental results for all Kolsky bar experiments with strain rates in the range of 70-245 s^{-1}. To demonstrate that an approximately constant strain rate deformation was achieved, strain rate profiles are plotted in **Fig. 41**. For most confinement pressures, a distinct plateau is present to confirm a constant strain rate deformation. However, experiments at 100 MPa resulted in a gradual increase of strain rate from 100 s^{-1} to approximately 200 s^{-1} before reaching the peak stress. This is mainly caused by the brittle-to-ductile transition of the material constitutive behavior between 100~200 MPa confining pressure, which makes precise pulse shaping very difficult as the material response becomes increasingly nonlinear. To observe stress-strain behavior, principal engineering stress difference (q_{eng}) is plotted in **Fig. 42** as a function of strain for each experiment.

Table 10. Summary of Kolsky bar experiments.

			Principal engineering stress difference, q_{eng}		
Specimen Number	Confinement Pressure (MPa)	Strain Rate (s^{-1})	Peak (MPa)	Mean (MPa)	Coefficient of Variation (%)
1	0	70	255.7	249.6	3.10%
2	0	75	244.4		
3	0	70	256.6		
4	0	75	252.7		
5	0	70	238.8		
6	10	90	291.3	303.0	2.81%
7	10	90	309.6		
8	10	85	297.7		
9	10	85	311.9		
10	10	90	304.5		
11	50	115	383.8	379.9	2.08%
12	50	115	389.3		
13	50	115	373.9		
14	50	115	369.8		
15	50	110	382.6		
16	100	190	398.7	412.4	3.57%
17	100	200	404.6		
18	100	205	422.9		
19	100	195	402.8		
20	100	185	432.8		
21	200	235	464.4	473.7	6.34%
22	200	225	489.3		
23	200	245	432.5		
24	200	240	468.9		
25	200	215	513.2		

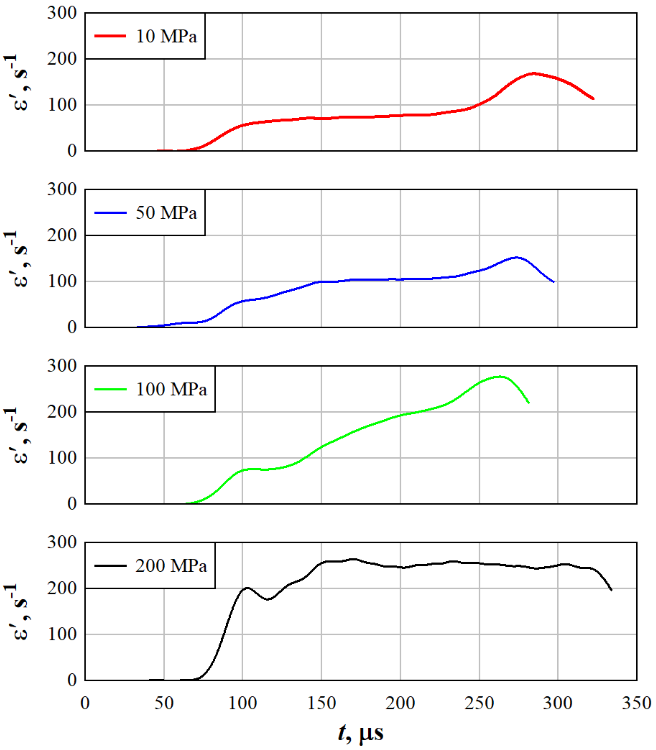

Fig. 41. Kolsky bar strain rate histories at each confinement pressure.

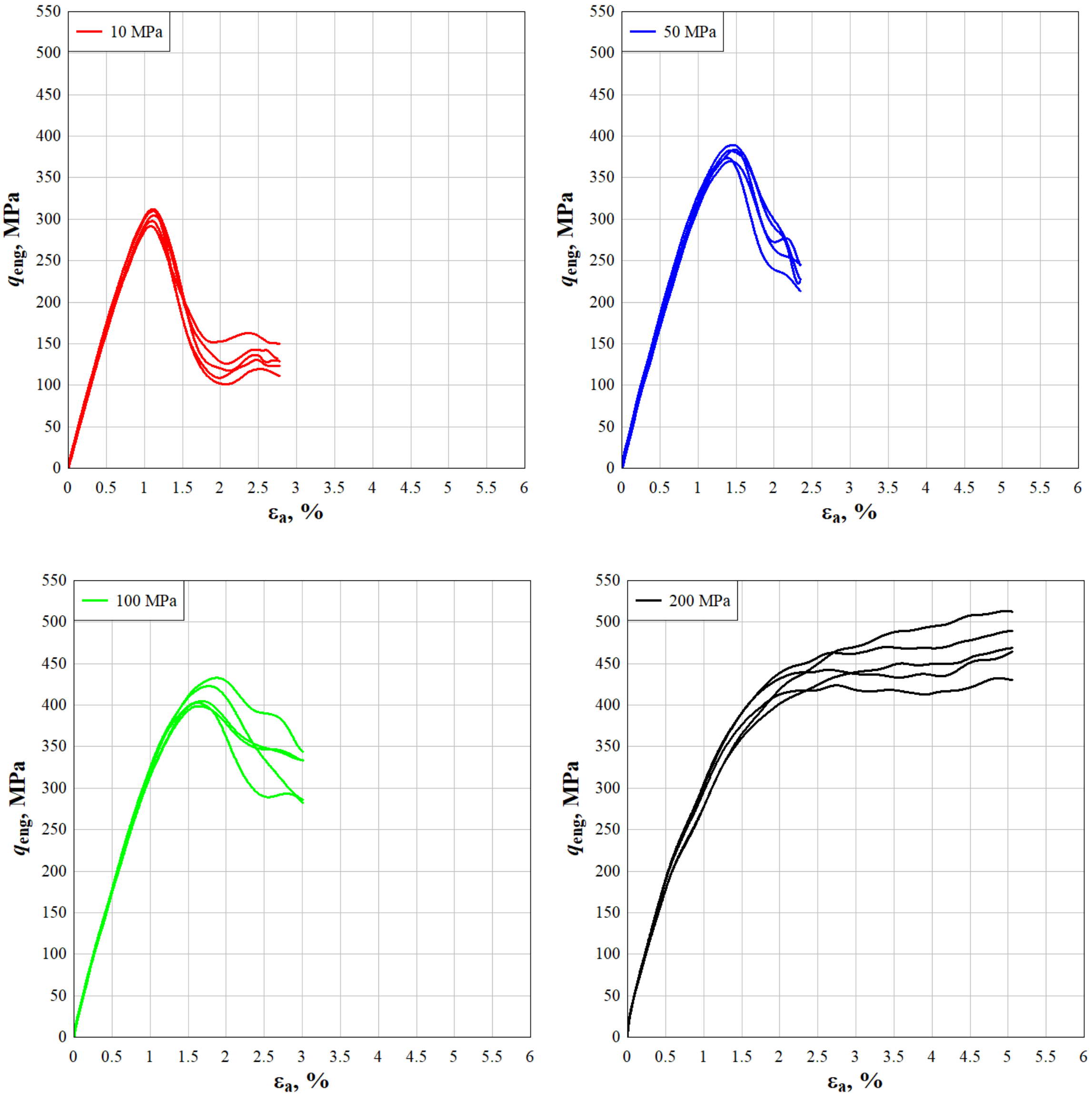

Fig. 42. Stress-strain behavior at each confinement pressure.

Dynamic strain rates had minimal variation for a given combination of confining pressure and pulse shaper design. The coefficient of variation (COV, standard deviation divided by the mean) for peak stress values was 2.0-3.6% for specimens tested at confinement pressures up to 100 MPa. Previous research on dynamic triaxial properties of granite observed that size effects increased COV at low levels of confinement for 11.8-mm-diameter specimens [129]. The consistently low COV in the present study further supports the earlier claim that the 25-mm x 25-mm specimens are representative. The increased COV for 200 MPa experiments is likely due to these specimens' inability to reach a peak stress prior to unloading. Specimens under confining pressures of 200 MPa would have likely experienced a further increase in q_{eng} if higher strain deformations were possible under dynamic loading conditions.

4.3.2.3 Dynamic Pressure Changes

In section **4.3.2.2**, a key assumption is that the hydrostatic pressure remains constant throughout the duration of the dynamic experiment. However, it must be noted that a pressure increase may occur as the result of the hydraulic fluid's being compressed together with the test specimen by the advancing incident bar. In this research, an analytical study is conducted to evaluate the amount of hydrostatic pressure change during the specimen deformation.

In general, two aspects contribute to the pressure changes in the triaxial chamber. One is the possible specimen volume change during axial loading, and the other is the squeezing of the hydraulic fluid as a result of bar movement. Since it is extremely challenging to directly acquire radial deformation, and thus the volume change, of the specimen during the dynamic test, the volumetric strain was instead measured from quasi-static tests under the same loading path. The engineering axial, radial, and volumetric strains measured from triaxial compression experiments at the confining pressure of 200 MPa are presented in

Fig. 43a. Synchronizing the strain measurement with the loading procedure shown in

Fig. 43b, an initial axial deformation ΔL_{a0} with corresponding strain ε_{a0} (positive in compression) driven by the increase of hydrostatic pressure up to the predetermined level (200

MPa) can be determined. To exclude this deformation from the initial system setup, the corrected specimen axial strain ${\varepsilon_a}'$ is then given by

Eq. 12: $$ {\varepsilon_a}'(t) = \frac{\Delta {L_a}'(t)}{{L_a}'} = \frac{\Delta L_a(t) - \Delta L_{a0}}{L_a - \Delta L_{a0}} $$

where L_a is the axial dimension of the undeformed concrete specimen. By submitting the real-time axial engineering strain $\varepsilon_a(t) = \Delta L_a(t)/L_a$ and the initial axial strain $\varepsilon_{a0} = \Delta L_{a0}/L_a$ into **Eq. 12**, we then have

Eq. 13: $$ {\varepsilon_a}'(t) = \frac{\varepsilon_a(t) - \varepsilon_{a0}}{1 - \varepsilon_{a0}} $$

Similarly, the corrected radial strain is given by

Eq. 14: $$ {\varepsilon_r}'(t) = \frac{\varepsilon_r(t) - \varepsilon_{r0}}{1 - \varepsilon_{r0}} $$

where ε_{r0} is the initial radial strain. Both corrected and uncorrected axial and radial strains are presented in

Fig. 43a, together with the volumetric strain $\varepsilon_V(t)$ (uncorrected) and ${\varepsilon_V}'(t)$ (corrected). The volume change of the hydraulic fluid caused by the specimen deformation can then be expressed as

Eq. 15: $$ \Delta V_1'(t) = -[-V_s \varepsilon_V'(t)] = S_s L_a [{\varepsilon_a}'(t) + 2{\varepsilon_r}'(t)\,] $$

where S_s is the cross-sectional area of the concrete specimen. Additionally, a strain ratio factor $\nu(t)$ is introduced

Eq. 16: $$ \nu(t) = -\frac{{\varepsilon_r}'(t)}{{\varepsilon_a}'(t)} $$

In typical uniaxial compression or tension, $\nu(t)$ is known as the Poisson's ratio and is generally considered a rate-independent constant. Herein we still assume $\nu(t)$ is rate-independent under triaxial loading conditions, but its value may be dependent on the axial deformation history of the specimen. Under this assumption, the specimen radial deformation under dynamic triaxial loading can be inferred from that of the quasi-static triaxial loading at the same axial strain and confining pressure. In this case, **Eq. 16** can be written as

Eq. 17: $$\nu(\varepsilon_a{'}) = -\frac{\varepsilon_r{'}}{\varepsilon_a{'}}$$

With **Eq. 15**, **Eq. 16**, and **Eq. 17**, we can establish the volume change for the specimen under dynamic triaxial loading

Eq. 18: $$\Delta V_1' = S_s L_a \varepsilon_a' [1 - 2\nu(\varepsilon_a{'})]$$

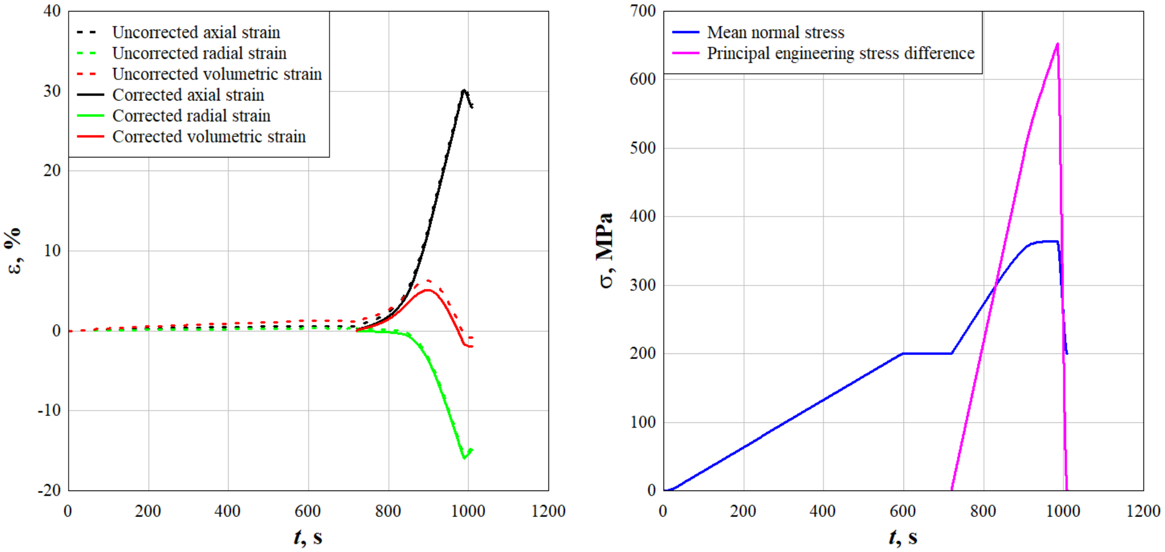

Fig. 43. The corrected and uncorrected engineering strain histories from quasi-static triaxial compression (left) and specimen loading and deformation histories from quasi-static triaxial compression at confining pressure of 200 MPa (right).

On the other hand, the movement of the Kolsky bars, which directly interface with the hydraulic fluid and the specimen during dynamic loading, may also cause additional volume change as the gap between the two bar ends decreases with specimen deformation. The change of volume caused by bar movement can be expressed as

Eq. 19: $$\Delta V_2(t) = -S_b \Delta L_a(t)$$

where S_b is the cross-sectional area of the bars. Then the corrected volume change can be written as

Eq. 20: $$\Delta V_2'(t) = -S_b[\Delta L_a(t) - \Delta L_{a0}]$$

By submitting Eq.3 into Eq. 11, we have

Eq. 21: $$\Delta V_2' = S_b L_a \varepsilon_a{}'(\varepsilon_{a0} - 1)$$

Finally, the total corrected volume change ΔV_k of the hydraulic fluid throughout the dynamic triaxial experiment is

Eq. 22: $$\Delta V_k' = \Delta V_1' + \Delta V_2'$$

For a specimen loaded to a certain axial strain in dynamic tests, the corresponding volume change ΔV_k can be determined based on **Eq. 22**, and the results are shown in **Fig. 44** together with the normalized value $\Delta V_k/V_k$ which represents the volumetric strain of the fluid. The total initial volume of the hydraulic fluid in the confinement chamber is $V_k = 810.4$ cm^3. Due to very limited experimental data for the equation of state for the hydraulic fluid (kerosene), it is assumed that the pressure in the confinement chamber increases linearly with decreasing volume

Eq. 23: $$\Delta P = -K \Delta V_k / V_k$$

where $K = 1.3$ GPa is the bulk modulus of kerosene [133]. To better demonstrate the pressure change in the chamber relative to the applied confinement pressure, a pressure change factor is defined as

Eq. 24: $$\eta = \Delta P/P$$

where *P* is the hydrostatic confining pressure under which the dynamic triaxial tests were conducted.

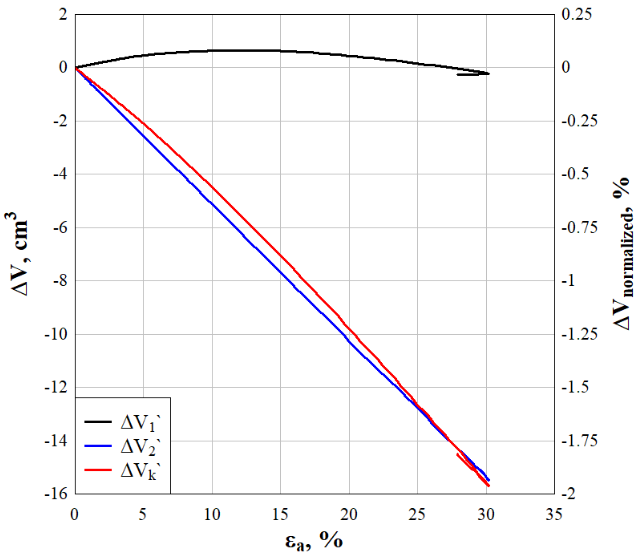

Fig. 44. Volume change of the hydraulic fluid as a function of the specimen axial strain.

Based on the above discussion, the pressure change throughout the duration of the specimen deformation is calculated and presented in **Fig. 45**. The chamber pressures are found to increase by 0.69-3.4 MPa, depending on the peak specimen strain. The stars placed in **Fig. 45** represent the peak specimen strain (at which the specimen failure strength is calculated) under each respective confining pressure. Meanwhile, Table 1 gives a detailed pressure change under different initial hydrostatic pressures when specimens reach their peak stress. For confining pressures of 10 MPa, the pressure change factor is $\eta = 0.069$. This factor decreases drastically with increasing hydrostatic pressure and reaches the lowest value of 0.011 at 100 MPa. The data presented in **Table 11** and **Fig. 45** show that the overall dynamic pressure change in the confinement chamber is relatively small. Therefore, this slight fluctuation in confining pressure is not likely to cause significant error for the strength characterization.

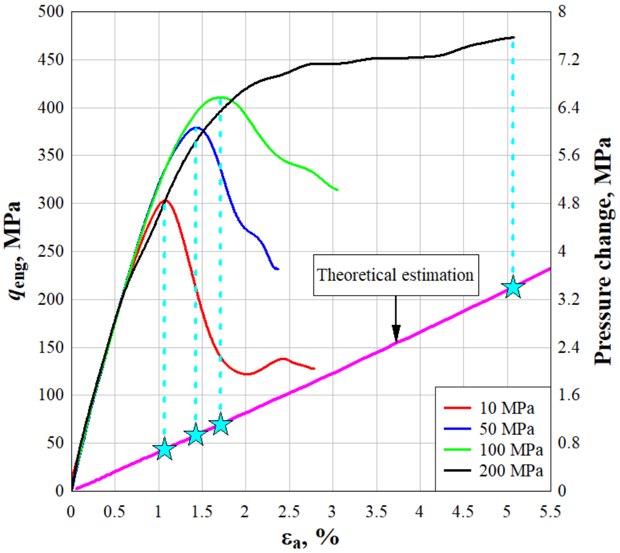

Fig. 45: The pressure change in the confinement chamber throughout the duration of the specimen deformation.

Table 11. The calculation of pressure change under different initial hydrostatic pressures.

Initial hydrostatic pressure (MPa)	10	50	100	200
Axial strain at peak stress (%)	1.07	1.43	1.71	5.07
Pressure increase (MPa)	0.69	0.94	1.10	3.40
Relative pressure change (%)	6.9	1.9	1.1	1.7

4.3.3 Pressure-dependent Dynamic Increase Factor

The dynamic increase factor (DIF) is a ratio between dynamic and quasi-static strength that is commonly used to determine rate-effect parameters based on unconfined compression experiments. The novel triaxial Kolsky bar technique developed in the current study offers a unique opportunity to calculate the DIF as a function of confining pressure. In **Fig. 46**, triaxial Kolsky bar data are compiled with quasi-static triaxial data to provide a means of direct comparison. Quasi-static data are represented by a solid line that represents the average response from two replicate specimens for a given loading condition. Similarly, dynamic data are presented by a dashed line that represents the average response from five replicate specimens for a given loading condition. Quasi-static tests previously published in terms of *q* have been converted to q_{eng}, as presented in **Table 12**.

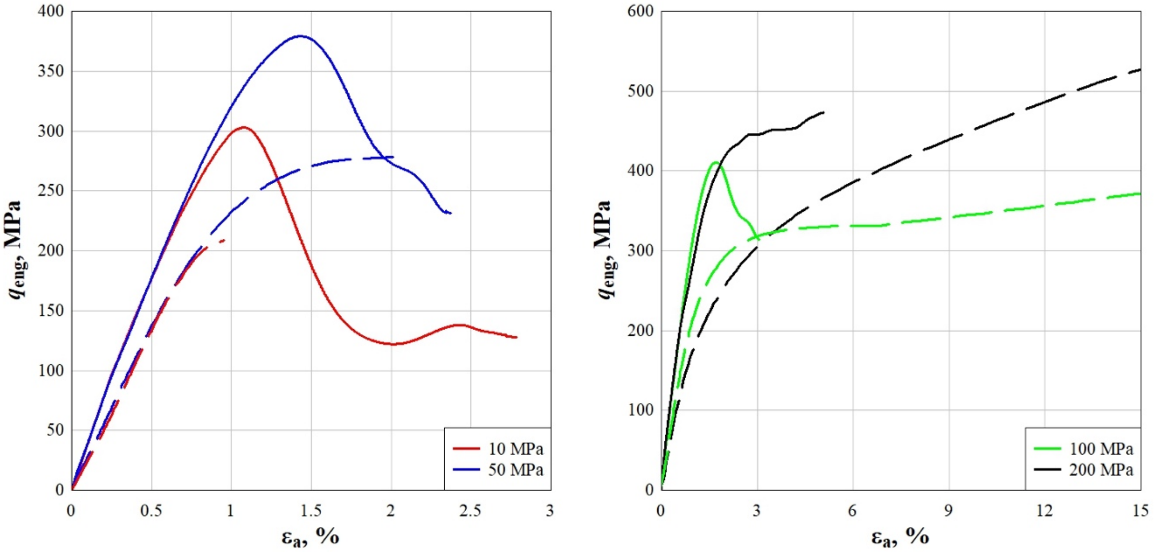

Fig. 46. Quasi-static (dashed lines) and dynamic (solid lines) response of BBR9 concrete under different confining pressure.

Table 12. Quasi-static principal stress difference conversion.

Confinement Pressure (MPa)	Strain Rate (s^{-1})	Peak q (MPa)	Peak q_{eng} (MPa)
0	10^{-5}	140.7	140.7
10	10^{-4}	204.2	208.7
50	10^{-4}	274	278.2
100	10^{-4}	318.3	---
200	10^{-4}	497.4	---

As evidenced in **Table 12**, converting principal stress difference from q (true stress) to q_{eng} (engineering stress) results in minor differences at confining pressures ranging from 0-50 MPa. This negligible difference is directly related to small changes in cross-sectional area. However, triaxial experiments ranging from 100-200 MPa experience substantial changes in cross-sectional area. Referencing **Fig. 46**, tests at 100 MPa and 200 MPa do not reach a peak value in terms of q_{eng} after undergoing axial strains of 15%. Specimens were not tested beyond 15% axial strain due to the development of non-uniform deformation (barreling) [74].

Subsequently, the DIF was calculated for each confinement pressure by dividing the dynamic peak stress by the quasi-static peak stress. Values for the DIFs are presented in **Table 13**. For the 100 MPa triaxial experiments, a peak stress was recorded only in terms of q, so the Kolsky bar data at 100 MPa was transformed into true stress to make an approximation of the DIF. Since radial strains were not measured directly during Kolsky bar experiments, the 100 MPa DIF approximation assumed that the relationship between axial and radial strains observed at quasi-static strain rates would also be valid at dynamic strain rates. The DIF could not be calculated or approximated at 200 MPa, since peak stresses were not observed in either quasi-static or dynamic tests. A clear trend emerges showing that the DIF decreases with increasing confining pressure. Another key observation from **Fig. 46** is that the brittle-ductile transition shifts under dynamic strain rates, as evidenced by material behavior under 100 MPa confining pressure.

Table 13. Pressure dependency of the DIF for BBR9.

	Quasi-Static		Dynamic		
Confinement Pressure (MPa)	Strain Rate (s^{-1})	Peak q_{eng} (MPa)	Strain Rate (s^{-1})	Peak q_{eng} (MPa)	DIF
0	10^{-5}	140.7	70	249.6	1.77
10	10^{-4}	208.7	90	303.0	1.45
50	10^{-4}	278.2	105	379.9	1.37
100	10^{-4}	---	195	412.4	~1.29*

* Approximated by transforming 100 MPa Kolsky bar data from q_{eng} to q

A recent study on the uniaxial unconfined DIF for this same material reveals that the damage initiation under impact loading occurs at a stress level much lower than the peak failure stress, which is what has been typically used for the DIF calculation [65]. Therefore, the DIF calculated by using the damage initiation stress, known as the True DIF, appears to have a much lower value (~1.32). In the current study, a transition in damage mechanism from axial splitting to shear cracking was observed with increasing confining pressure. While axially cracked specimens are still capable of bearing dynamic axial mechanical loading, which leads to higher peak failure stress, such load-bearing capability is completely compromised once the failure mode changes to shear cracking. Hence, it is reasonable to assume that the lower DIF observed at higher confining pressure is caused by the gradual transitioning of failure mode.

4.3.4 Dynamic Failure Surface

From prior work [74,80,81], a quasi-static failure surface was developed for BBR9 high-strength concrete using cylindrical specimens with a diameter of 50 mm and a length of 114 mm. However, experimental work has not previously been used to validate changes in the failure surface for dynamic events under complex stress states. Since the DIF values from **Table 13** are calculated by using the same specimen geometry at both quasi-static and dynamic strain rates, the DIFs are applied to the quasi-static failure surface, as the DIFs do not inherently contain size effects. Prior research on high-strength concrete has shown that unconfined failure strength is dependent on specimen geometry while the DIF is independent of specimen size [89]. The authors recognize that this observation may or may not hold true under triaxial loading conditions. Under the assumption that the DIF is independent of specimen size for triaxial Kolsky bar experiments, the calculated DIF values were applied to the quasi-static failure surface, as shown in **Fig. 47**, by extending quasi-static test data (solid lines) with a dynamic strength increase (dashed lines).

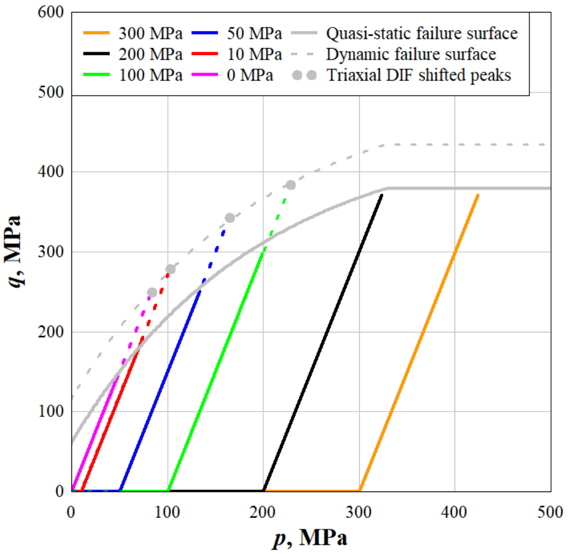

Fig. 47. Dynamic failure surface in terms of principal stress difference (q) and mean normal stress (p).

As evidenced by the decay in the DIF at increasing confinement pressures, the failure surface should shift as a function of both strain rate and stress state. After applying the DIFs to the quasi-static triaxial results for 50-mm x 114-mm specimens, the triaxial DIF shifted peaks were plotted as distinct points for determining a dynamic failure surface. It is clear that a scalar multiplier for strain rate effects would not match the experimental results presented in this study. However, a vertical offset of 55 MPa applied to the quasi-static failure surface results in a dynamic failure surface that fits well with peak values of q that were shifted to account for the triaxial DIF values. Please note that the proposed dynamic failure surface accounts only for experimental results with confining pressures in the range of 0-100 MPa. These results are intended to provide a visual representation of the DIF values presented in **Table 13**. Although the dynamic failure surface cannot be directly incorporated into existing concrete models, it does provide an experimental basis for further interrogation of future modeling and simulation efforts.

4.4 Conclusions

A large-diameter triaxial Kolsky bar was designed and implemented to characterize the bulk material behavior of heterogenous brittle materials as a function of both strain rate and confining pressure. BBR9 high-strength concrete was selected as a representative material for this study, but the method is applicable to a variety of concretes and other brittle materials. To quantify rate effects, BBR9 specimens were tested at quasi-static strain rates and dynamic strain rates for the same specimen geometry and boundary conditions. All data presented in this study were gathered from cylindrical concrete specimens with a diameter and length of 25.4 mm. The confining pressures in this study included tests at 0 MPa, 10 MPa, 50 MPa, 100 MPa, and 200 MPa. Specific conclusions are presented in the list below.

- A specimen sealing technique was established by using a latex membrane paired with layered epoxy to sufficiently isolate the specimen from confining fluid while maintaining a non-rigid form.
- Dynamic pressure variations within the confining chamber were determined to be negligible, with a maximum relative pressure change of 6.9%.
- Annular pulse shaping techniques were incorporated to provide various geometries from annealed copper sheets to establish constant strain rate deformations at each loading condition.
- Stress equilibrium was verified at lower confining pressures where deformation time is shortest. Subsequent tests calculated the reflected wave as the difference between the incident and the transmitted waves to avoid signal interference from the detachment wave resulting from the stopper/bar interface.

- Triaxial Kolsky bar experiments provided very repeatable high strain rate deformations with a maximum COV of 6.3% for q_{eng} values at confining pressures of 200 MPa.
- The dynamic increase factor (DIF) was determined to decay as confining pressure increases. The DIF values were 1.77, 1.45, 1.37 and ~1.29 for confining pressures of 0 MPa, 10 MPa, 50 MPa, and 100 MPa, respectively.
- The brittle to ductile transition point shifts as a function of strain rate. This is evidenced at 100 MPa where the failure mode is extremely ductile at quasi-static strain rates but becomes brittle at dynamic strain rates.
- A dynamic failure surface was presented to illustrate interdependent effects from both strain rate and confining pressure.

This study confirms that the behavior of high-strength concrete is both strain-rate and pressure dependent. For high-fidelity modeling of concrete under extreme loading conditions, it is imperative to quantify the dynamic material behavior under complex stress states. The large-diameter triaxial Kolsky bar provides an experimental method to support future interrogation of modeling parameters, as it has proven to be a robust method for characterizing dynamic triaxial properties of cementitious materials with representative specimen sizes.

CHAPTER 5:

CONCLUSIONS

5.1 Conclusions

The research presented in this study provides novel methods and results for determining the damage evolution and high-rate response of high-strength concrete under triaxial loading. As a foundational step, size effects were rigorously investigated in terms of changes in diameter and length-to-diameter ratio. Size effects must be considered since damage analysis and high-rate experiments require non-standard specimen geometries. The results show that specimen diameter can be successfully reduced from 50 mm to 25 mm while maintaining the same stress-strain relationships under confining pressures ranging from 10-200 MPa. Furthermore, changes in L/D from 2.0 to 1.0 were shown to have minimal effects on triaxial stress-strain relationships. A scalar correction factor (similar to those recommended by ASTM for unconfined compression) provides an empirical solution that accounts for end effects while maintaining minor variations as compared to standard specimen geometries. Thus, specimens with reduced diameter and reduced L/D were shown to be representative of the bulk material behavior of high-strength concrete.

Specimens having a diameter of 25 mm and an L/D of either 1.0 or 2.0 were evaluated for damage evolution after undergoing quasi-static triaxial compression with confining pressures of 10, 50, 100, and 200 MPa. A removable strain gauge mount was also incorporated to document volumetric strain behavior. Each specimen was scanned in the pristine and damaged condition to make direct comparisons for damage isolation and quantification. Specimens in a brittle failure mode ultimately failed along shear planes with higher crack saturation as confining pressures increased from 10 MPa to 50 MPa. Specimens undergoing a ductile failure mode (100 MPa and 200 MPa confinement pressures) experienced substantial pore collapse and microcracking while maintaining residual strength capacities of 30-50%. Although damage modes were similar, increasing the confinement pressure from 100 MPa to 200 MPa resulted in additional pore compaction, especially for smaller pore sizes (below 120 um). Specimens with a reduced L/D (1.0) had slightly more distributed crack growth due to end effects, but damage modes remained consistent with specimens having a standard L/D (2.0).

Lastly, high-rate response was investigated using a state-of-the-art large-diameter (50 mm) triaxial Kolsky bar. All triaxial Kolsky bar experiments required a specimen with a diameter of 25 mm and length of 25 mm (L/D = 1.0) to achieve dynamic stress equilibrium while maintaining a constant strain rate deformation. Annular pulse shapers were carefully designed for each level of confinement pressure. Quasi-static experiments were also conducted on the same specimen geometry to determine the dynamic increase factor (DIF) at each level of confinement pressure (10, 50, 100, and 200 MPa). The DIF was determined to be pressure dependent with results that provide insight towards the development of a dynamic failure surface. Additionally, comparisons in stress-strain relationships indicate that failure modes transition from ductile to brittle as strain rates increase from quasi-static to dynamic.

After verifying the suitability of non-standard specimen sizes, damage progression and dynamic material behavior have been recorded under a variety of triaxial loading conditions. The results link damage morphology under complex stress states to material property measurements. Furthermore, it has been shown that rate parameters are pressure dependent, indicating that quasi-static triaxial characterization is not sufficient to fully describe the dynamic behavior of high-strength concrete under extreme loading events.

5.2 Future Work

The presented research program has confirmed the suitability of non-standard specimen geometries, developed methods for quantifying damage accumulation, and established an experimental technique for a large-diameter triaxial Kolsky bar. These developments have led to the following ideas for future research activities.

- In practice, high-strength concrete and ultra-high-performance concrete (UHPC) frequently incorporates fiber reinforcement. Future work should aim at understanding the effects of fibers on damage evolution and high-rate response under triaxial loadings.
- The scope of damage evolution portion of this study was limited to quasi-static triaxial loadings. However, the development of a single loading technique for the triaxial Kolsky bar could provide a way to observe dynamic damage evolution under triaxial loadings.
- In quasi-static triaxial experiments, saturation (moisture content) effects can be substantial, especially at high confinement pressures. A rigorous investigation of saturation effects using the triaxial Kolsky bar might show that saturation effects become more significant at dynamic strain rates.
- The pressure dependent DIF values should be utilized to interrogate material models to determine the sensitivity of adjustments in a dynamic failure surface. Perhaps model accuracy can be improved by adapting rate parameters to have a pressure dependent term.
- Lower values of DIF corresponding to damage initiation stress are likely attributed to the intrinsic enhancement of material strength at dynamic strain rates. However, high-

dynamic strength gain is likely a structural effect more so than a material effect [134]. Future work should take a closer look at developing a fundamental approach for understanding the different components that contribute to a dynamic increase factor, including crack tip inertia, crack velocity, radial confinement pressures, and corresponding wave speeds within a specimen. For reference, maximum crack-tip velocities are typically in the range of 8-30% of the primary (P) wave speed and typically less than 50% of the Rayleigh wave speed [135].

5.3 Publications

- **Williams B.**, Heard W., Graham S., Martin B., Loeffler C., Nie X. (2019). Mechanical Response and Damage Evolution of High-Strength Concrete Under Triaxial Loading. In: Kimberley J., Lamberson L., Mates S. (eds) Dynamic Behavior of Materials, Volume 1. Conference Proceedings of the Society for Experimental Mechanics Series. Springer, Cham
- **Williams B.**, Heard W., Martin B., Loeffler C., Nie X. (2020). Large-Diameter Triaxial Kolsky Bar for Evaluating Very-High-Strength Concrete. In: Lamberson L. (eds) Dynamic Behavior of Materials, Volume 1. Conference Proceedings of the Society for Experimental Mechanics Series. Springer, Cham
- **Williams, B. A.**, Heard, W. F., Graham, S. S., & Nie, X. (2020). Effect of specimen geometry on triaxial compressive response of high-strength concrete. *Construction and Building Materials*, *244*, 118348. http://doi.org/10.1016/j.conbuildmat.2020.118348
- **Williams, B. A.**, Sun, Q., Heard, W. F., Loeffler, C. Graham, S. S., Vankirk, G., and Nie, X. (submitted). Investigation of strain-rate and pressure effects for high-strength

concrete using a novel large-diameter triaxial Kolsky bar technique. *Cement and Concrete Composites*.

- **Williams, B. A.**, Madra, A., Heard, W. F., Graham, S. S., Grotke, M. J., Hillman, M. Z., Nie, X. (ERDC review). Characterizing damage modes and size effects in high-strength concrete under hydrostatic and triaxial stress states using X-ray microtomography. *Construction and Building Materials*.

BIBLIOGRAPHY

[1] Adley MD, Frank AO, Danielson KT. The high-rate brittle microplane concrete model: Part I: bounding curves and quasi-static fit to material property data. Computers and Concrete 2012;9:293–310. doi:10.12989/cac.2012.9.4.293.

[2] Frank AO, Adley MD, Danielson KT, McDevitt HSJ. The high-rate brittle microplane concrete model: Part II: application to projectile perforation of concrete slabs. Computers and Concrete 2012;9:311–25. doi:10.12989/cac.2012.9.4.311.

[3] Adley MD, Frank AO, Danielson KT, Akers SA, O'Daniel JL. ERDC/GSL TR-10-51 The Advanced Fundamental Concrete (AFC) Model. Vicksburg, MS: 2010.

[4] Williams EM, Graham SS, Reed PA, Rushing TS. ERDC/GSL TR-09-22 Laboratory characterization of Cor-Tuf concrete with and without steel fibers. 2009.

[5] Bažant ZP, Caner FC, Carol I, Adley MD, Akers SA. Microplane model M4 for concrete. I: Formulation with work-conjugate deviatoric stress. Journal of Engineering Mechanics 2000;126. doi:10.1061/(ASCE)0733-9399(2000)126\:9(944);pageGroup:string:Publication.

[6] Bell B, Brannon C, Crawford E, Hertel S. CTH User's Manual and Input Instructions, Version 6.01 2003.

[7] Johnson GR, Beissel SR, Gerlach CA, Holmquist TJ, Stryk RA. User instructions for the 2010 version of the EPIC code, Southwest Research Institute, Final Report. Contract W56HZV-06-C-0194 with US Army RDECOM-TARDEC 2010.

[8] Frank AO, Burchfield CA, Ertle CW. A Perspective on Modeling Ultra High Performance Concretes (UHPCs) with the High-Rate-Brittle (HRB) Model: material characterization, model fitting, and high-resolution fragment penetration simulations. Warheads and Ballistics Symposium, Monterey, CA: 2012.

[9] Cement Sustainability Initiative. The Cement Sustainability Initiative 2009:1–42.

[10] 239 ACI Committee. 239R-18: Ultra-High-Performance Concrete: An Emerging Technology Report 2018:1–5.

[11] C09 Committee. ASTM C39: Standard test method for compressive strength of cylindrical concrete specimens. West Conshohocken, PA: ASTM International; 2018. doi:10.1520/C0031_C0031M.

[12] Ozyildirim C, Carino NJ. Chapter 13: Concrete Strength Testing. Significance of Tests and Properties of Concrete and Concrete-Making Materials, West Conshohocken, PA 19428-2959: ASTM International; 2006, pp. 125–40. doi:10.1520/STP37731S.

[13] Arioz O, Ramyar K, Tuncan M, Tuncan A. Effect of Length-to-Diameter Ratio of Core Sample on Concrete Core Strength—Another Look. Jte 2007;36:1–4. doi:10.1520/JTE100573.

[14] Bartlett FM, MacGreggor JG. Effect of core length-to-diameter ratio on concrete core strengths. ACI Materials Journal 1994;91.

[15] Meininger RC, Wagner FT, Hall KW. Concrete Core Strength—The Effect of Length to Diameter Ratio. Jte 1977;5:147–53. doi:10.1520/JTE11631J.

[16] Tuncan M, Arioz O, Ramyar K, Karasu B. Assessing concrete strength by means of small diameter cores. Mechanics of Materials 2006.

[17] Bishop AW, Henkel DJ. The Measurement of Soil Properties in the Triaxial Test. London: Edward Arnold LTD; 1957.

[18] Balmer GG. Shearing strength of concrete under high triaxial stress-computation of Mohr's envelope as a curve. 1949.

[19] Kotsovos MD, Newman JB. Generalized Stress-Strain Relations for Concrete. Journal of the Engineering Mechanics Division 1978;104:845–56.

[20] Bellotti R, Rossi P. Cylinder tests: experimental technique and results. Mater Struct 1991;24:45–51. doi:10.1007/BF02472681.

[21] Chern J-C, Yang H-J, Chen H-W. Behavior of Steel Fiber Reinforced Concrete in Multiaxial Loading. ACI Materials Journal 1993;89:32–40. doi:10.14359/1242.

[22] Imran I, Pantazopoulou SJ. Experimental study of plain concrete under triaxial stress. HiPerMat 1996;November-December:589–601.

[23] Li QM, Meng H. About the dynamic strength enhancement of concrete-like materials in a split Hopkinson pressure bar test. International Journal of Solids and Structures 2003;40:343–60. doi:10.1016/S0020-7683(02)00526-7.

[24] Schmidt MJ, Cazacu O, Green ML. Experimental and theoretical investigation of the high-pressure behavior of concrete. International Journal for Numerical and Analytical Methods in Geomechanics 2009;33:1–23. doi:10.1002/nag.700.

[25] Gabet T, Malécot Y, Daudeville L. Triaxial behaviour of concrete under high stresses: Influence of the loading path on compaction and limit states. Cement and Concrete Research 2008;38:403–12. doi:10.1016/j.cemconres.2007.09.029.

[26] Poinard C, Piotrowska E, Malécot Y, Daudeville L, Landis EN. Compression triaxial behavior of concrete: the role of the mesostructure by analysis of X-ray tomographic images. European Journal of Environmental and Civil Engineering 2012;16:s115–36. doi:10.1080/19648189.2012.682458.

[27] Malécot Y, Daudeville L, Dupray F, Poinard C, Buzaud E. Strength and damage of concrete under high triaxial loading. European Journal of Environmental and Civil Engineering 2011;14:777–803. doi:10.1080/19648189.2010.9693262.

[28] Chuan-Zhi W, Zhen-Hai G, Xiu-Qin Z. Experimental Investigation of Biaxial and Triaxial Compressive Concrete Strength. ACI Materials Journal 1987;84:92–100. doi:10.14359/1808.

[29] Forquin P, Arias A, Zaera R. An experimental method of measuring the confined compression strength of geomaterials. International Journal of Solids and Structures 2007;44:4291–317. doi:10.1016/j.ijsolstr.2006.11.022.

[30] Akers SA, Reed PA, Ehrgott JQ. WES (Waterways Experiment Station) High-Pressure Uniaxial Strain and Triaxial Shear Test Equipment 1986.

[31] Williams EM, Akers SA, Reed PA. Laboratory Characterization of SAM-35 Concrete 2006.

[32] Williams EM, Akers SA, Reed PA. Laboratory Characterization of Gray Masonry Concrete 2007.

[33] Lee MY. Sandia Geomechanics Department Capabilities. 2011.

[34] Mondal AB, Chen WW, Martin BE, Heard WF. Dynamic Triaxial Compression Experiments on Cor-Tuf Specimens. In: Song B, Casem D, Kimberley J, editors. Cham: Springer International Publishing; 2014, pp. 245–9.

[35] Williams BA, Heard WF, Graham SS, Martin BE, Loeffler CM, Nie X. Mechanical Response and Damage Evolution of High-Strength Concrete Under Triaxial Loading. Dynamic Behavior of Materials, Volume 1, Cham: Springer, Cham; 2019, pp. 69–71. doi:10.1007/978-3-319-95089-1_9.

[36] Vankirk G, Heard WF, Frank A, Hammons M, Roth MJ. Residual Structural Capacity of a High-Performance Concrete. In: Kimberley J, Lamberson LE, Mates S, editors. vol. 815, Springer International Publishing; 2019, pp. 233–6. doi:10.1007/978-3-319-95089-1_42.

[37] Ragalwar K, Prieto V, Fakhri H, Heard WF, Williams BA, Ranade R. Systematic Development of Environmentally Sustainable Ultra-High Performance Concrete, Kassel, Germany: 2016.

[38] Ragalwar KA, Nguyen H, Ranade R, Heard WF, Williams BA. Influence of Distribution Modulus of Particle Size Distribution on Rheological and Mechanical Properties of Ultra-High-Strength SHCC Matrix. RILEM Bookseries 2017;15. doi:https://doi.org/10.1007/978-94-024-1194-2_26.

[39] C01 Committee. Standard Specification for Flow Table for Use in Tests of Hydraulic Cement. West Conshohocken, PA: ASTM International; 2016. doi:10.1520/C0230_C0230M-14.

[40] C09 Committee. ASTM C42: Standard Test Method for Obtaining and Testing Drilled Cores and Sawed Beams of Concrete. Westt Conshohocken, PA: ASTM International; 2020.

[41] Sfer D, Carol I, Gettu R, Etse G. Study of the behavior of concrete under triaxial compression. J Eng Mech 2002. doi:10.1061/jenmdt.2002.128.issue-2;page:string:Article/Chapter.

[42] Williams EM, Akers SA, Reed PA. ERDC/GSL TR-05-16 Laboratory Characterization of Fine Aggregate Cementitious Material. Vicksburg, MS: U.S. Army Engineer Research and Development Center; 2005.

[43] Beatty HB, Graham SS, Williams EM, Reed PA. Laboratory Characterization of Talley Brick 2011.

[44] Beatty HB, Graham SS, Moxley RE, Akers SA, Reed PA. ERDC/GSL TR-12-26 Laboratory Characterization of Adobe (Scottsdale) 2012.

[45] Van Mier JGM, Vonk RA. Fracture of concrete under multiaxial stress - recent developments. Pascal-FrancisInistFr 1991;24:61–5.

[46] C09 Committee. ASTM C192: Standard Practice for Making and Curing Concrete Test Specimens in the Laboratory. West Conshohocken, PA: ASTM International; 2016. doi:10.1520/C0070.

[47] Livingston CW, Smith FL. Bomb Penetration Project 1951.

[48] Cargile JD. Development of a Constitutive Model for Numerical Simulation of Projectile Penetration into Brittle Geomaterials 1999.

[49] Heard WF. Development and multi-scale characterization of a self-consolidating high-strength concrete for quasi-static and transient loads. vol. 15. Dordrecht: Springer Netherlands; 2014. doi:10.1007/978-94-024-1194-2.

[50] Toda H, Sinclair I, Buffiere JY, Maire E, Khor KH. A 3D measurement procedure for internal local crack driving forces via synchrotron X-ray microtomography. Acta Materialia 2004. doi:10.1016/j.actamat.2003.11.014.

[51] Landis EN, Zhang T, Nagy EN, Nagy G. Cracking, damage and fracture in four dimensions. Mater Struct 2007. doi:10.1617/s11527-006-9145-5.

[52] Huang S, Xia K, Zheng H. Observation of microscopic damage accumulation in brittle solids subjected to dynamic compressive loading. Review of Scientific Instruments 2013. doi:10.1063/1.4821497.

[53] de Wolski SC, Bolander JE, Landis EN. An in-situ x-ray microtomography study of split cylinder fracture in cement-based materials. Exp Mech 2014. doi:10.1007/s11340-014-9875-1.

[54] Nguyen TT, Yvonnet J, Bornert M, Chateau C. Initiation and propagation of complex 3D networks of cracks in heterogeneous quasi-brittle materials: Direct

comparison between in situ testing-microCT experiments …. J Mech Phys Solids 2016. doi:10.1016/j.jmps.2016.06.004.

[55] Skarżyński Ł, Tejchman J. Experimental Investigations of Fracture Process in Concrete by Means of X-ray Micro-computed Tomography. Strain 2016. doi:10.1111/str.12168.

[56] Renard F. Microfracturation in rocks: from microtomography images to processes. The European Physical Journal Applied Physics 2012. doi:10.1051/epjap/2012120093.

[57] Cnudde V, Boone MN. High-resolution X-ray computed tomography in geosciences: A review of the current technology and applications. Earth Science Reviews 2013;123:1–17. doi:10.1016/j.earscirev.2013.04.003.

[58] Morgan IL, Ellinger H, Klinksiek R, Thompson JN. Examination of Concrete by Computerized Tomography. Jp 1980;77:23–7. doi:10.14359/6987.

[59] Landis EN, Nagy EN, Keane DT, Shah SP. Observations of internal crack growth in mortar using x-ray microtomography. Materials for the New Millennium, ASCE; 1996, pp. 1330–6.

[60] Landis EN, Keane DT. X-ray microtomography for fracture studies in cement-based materials. Spie 1999.

[61] Landis EN, Nagy EN, Keane DT. Microstructure and fracture in three dimensions. Engineering Fracture Mechanics 2003;70:911–25. doi:10.1016/S0013-7944(02)00157-1.

[62] Diamond S, Landis EN. Microstructural features of a mortar as seen by computed microtomography. Mater Struct 2007. doi:10.1617/s11527-006-9194-9.

[63] Lawler JS, Keane DT, Shah SP. Measuring Three-Dimensional Damage in Concrete under Compression. ACI Materials Journal 2001;98:465–75. doi:10.14359/10847.

[64] Hild F, Roux S, Bernard D, Hauss G. On the use of 3D images and 3D displacement measurements for the analysis of damage mechanisms in concrete-like materials. International Conference on Fracture Mechanics of Concrete and Concrete Structures, 2013.

[65] Loeffler CM, Sun Q, Williams BA, Martin BE, Heard WF, Nie X. A Damage-Based Approach to Determine the Dynamic Increase Factor for Concrete. J Dynamic Behavior Mater 2020;24:1–11. doi:10.1007/s40870-019-00232-9.

[66] Landis EN, Nagy EN, Keane DT, Nagy G. Technique to Measure 3D Work-of-Fracture of Concrete in Compression. J Eng Mech 1999;125:599–605. doi:10.1061/(ASCE)0733-9399(1999)125:6(599).

[67] Mahabadi OK, Randall NX, Zong Z, Grasselli G. A novel approach for micro-scale characterization and modeling of geomaterials incorporating actual material heterogeneity. Geophys Res Lett 2012;39:n/a–n/a. doi:10.1029/2011GL050411.

[68] Bernardes EE, Carrasco EVM, Vasconcelos WL. X-ray microtomography (μ-CT) to analyze the pore structure of a Portland cement composite based on the selection of different regions of interest. Construction and Building Materials 2015. doi:10.1016/j.conbuildmat.2015.07.128.

[69] Henry M, Darma IS, Sugiyama T. Analysis of the effect of heating and re-curing on the microstructure of high-strength concrete using X-ray CT. Construction and Building Materials 2014;67:37–46. doi:10.1016/j.conbuildmat.2013.11.007.

[70] Fan S, Li M. X-ray computed microtomography of three- dimensional microcracks and self-healing in engineered cementitious composites. Smart Materials and Structures 2014;24:1–14. doi:10.1088/0964-1726/24/1/015021.

[71] Brisard S, Serdar M, Monteiro PJM. Multiscale X-ray tomography of cementitious materials_ A review. Cement and Concrete Research 2020;128:105824. doi:10.1016/j.cemconres.2019.105824.

[72] Frash LP, Carey JW, Lei Z, Rougier E, Ickes T, Viswanathan HS. High-stress triaxial direct-shear fracturing of Utica shale and in situ X-ray microtomography with permeability measurement. Journal of Geophysical Research 2016:1–16. doi:10.1002/(ISSN)2169-9356.

[73] Zingg L, Malécot Y, Briffaut M, Baroth J, Pla S. A Radial Strain Sensor for the Characterization of Concrete Under Triaxial Loading. Exp Mech 2015;56:703–11. doi:10.1007/s11340-015-0109-y.

[74] Williams BA, Heard WF, Graham SS, Nie X. Effect of specimen geometry on triaxial compressive response of high-strength concrete. Construction and Building Materials 2020;244:118348. doi:10.1016/j.conbuildmat.2020.118348.

[75] Girgin ZC, Arioglu N, Journal EAAS, 2007. Evaluation of strength criteria for very-high-strength concretes under triaxial compression. HiPerMat n.d.

[76] Wang YB, Liew JY, Journal SLAM, 2016. EBSCOhost | 112480065 | Experimental Study of Ultra-High-Strength Concrete under Triaxial Compression. ACI Materials Journal n.d.

[77] Sovják R, Vogel F, Beckmann B. TRIAXIAL COMPRESSIVE STRENGTH OF ULTRA HIGH PERFORMANCE CONCRETE. Acta Polytech 2013;53:901–5. doi:10.14311/AP.2013.53.0901.

[78] Ragalwar K, Heard WF, Williams BA, Ranade R. Significance of the particle size distribution modulus for strain-hardening-ultra-high performance concrete (SH-UHPC) matrix design. Construction and Building Materials 2020;234:117423. doi:10.1016/j.conbuildmat.2019.117423.

[79] Williams BA, Heard WF, Martin BE, Loeffler CM, Nie X. Large-Diameter Triaxial Kolsky Bar for Evaluating Very-High-Strength Concrete. Dynamic Behavior of Materials, Volume 1, Cham: Springer, Cham; 2020, pp. 115–8. doi:10.1007/978-3-030-30021-0_20.

[80] Vankirk G, Heard WF, Frank A, Hammons M, Roth MJ. Residual Structural Capacity of a High-Performance Concrete. Dynamic Behavior of Materials, Volume 1, Cham: Springer, Cham; 2019, pp. 233–6. doi:10.1007/978-3-319-95089-1_42.

[81] Vankirk G, Frank AO, Roth MJ. The Effects of Concrete Damage on Projectile Penetration: A Computational Study using the HRB Model and the EPIC Hydrocode. International Symposium for the Interaction of Munitions with Structures, Panama City Beach: 2019, pp. 1–14.

[82] Madra A, Hajj NE, Benzeggagh M. X-ray microtomography applications for quantitative and qualitative analysis of porosity in woven glass fiber reinforced thermoplastic. Composites Science and Technology 2014;95:50–8. doi:10.1016/j.compscitech.2014.02.009.

[83] Madra A, Adrien J, Breitkopf P, Maire E, Trochu F. A clustering method for analysis of morphology of short natural fibers in composites based on X-ray microtomography. Composites Part a: Applied Science and Manufacturing 2017;102:184–95. doi:10.1016/j.compositesa.2017.07.028.

[84] Lu X, Hsu C-TT. Behavior of high strength concrete with and without steel fiber reinforcement in triaxial compression. Cement and Concrete Research 2006;36:1679–85. doi:10.1016/j.cemconres.2006.05.021.

[85] Mindess S, Young FJ, Darwin D. Concrete. 2nd ed. Upper Saddle River, NJ: Pearson Education, Inc; 2003.

[86] Frank AO, Burchfield CA, Ertle CW. A Perspective on Modeling Ultra High Performance Concretes (UHPCs) with the High-Rate-Brittle (HRB) Model: material characterization, model fitting, and high-resolution fragment penetration simulations. Warheads and Ballistics Symposium, Monterey, CA: 2012.

[87] Paliwal B, Hammi Y, Moser RD, Horstemeyer MF. A three-invariant cap-plasticity damage model for cementitious materials. International Journal of Solids and Structures 2016;108:186–202. doi:10.1016/j.ijsolstr.2016.12.015.

[88] Bischoff PH, Perry SH. Compressive behaviour of concrete at high strain rates. Mater Struct 1991;24:425–50. doi:10.1007/BF02472016.

[89] Martin BE, Heard WF, Loeffler CM, Nie X. Specimen Size and Strain Rate Effects on the Compressive Behavior of Concrete. Exp Mech 2018;58:1–12. doi:10.1007/s11340-017-0355-2.

[90] Kolsky H. An investigation of the mechanical properties of materials at very high rates of loading, 1949, pp. 676–700. doi:10.1088/0370-1301/62/11/302.

[91] Kolsky H. Stress Waves in Solids. New York: Dover Publications, Inc; 1963.

[92] Hopkinson B. A method of measuring the pressure produced in the detonation of high, explosives or by the impact of bullets. Phil Trans R Soc Lond A 1914;213:437–56. doi:10.1098/rsta.1914.0010.

[93] Goldsmith W, Polivka M, Yang T. Dynamic behavior of concrete. Exp Mech 1966;6:65–79. doi:10.1007/BF02326224.

[94] Hughes BP, Gregory R. Concrete subjected to high rates of loading in compression. Magazine of Concrete Research 2015;24:25–36. doi:10.1680/macr.1972.24.78.25.

[95] Ross CA, Thompson PY, Tedesco JW. Split-Hopkinson Pressure-Bar tests on Concrete and Mortar in Tension and Compression. ACI Materials Journal 1989;86:475–81. doi:10.14359/2065.

[96] Ross CA, Jerome DM, Tedesco JW, Hughes ML. Moisture and Strain Rate Effects on Concrete Strength. ACI Materials Journal 1996;93:293–300. doi:10.14359/9814.

[97] Grote DL, Park SW, Zhou M. Dynamic behavior of concrete at high strain rates and pressures: I. experimental characterization. Int J Impact Eng 2001;25:869–86. doi:10.1016/S0734-743X(01)00020-3.

[98] Groeneveld AB, Ahlborn TM, Crane CK, Long WR. ERDC/GSL TR-17-23 Effect of Fiber Orientation on Dynamic Compressive Properties of an Ultra-High Performance Concrete. Vicksburg, MS: 2017.

[99] JOHN R, ANTOUN T, RAJENDRAN AM. EFFECT OF STRAIN RATE AND SIZE ON TENSILE STRENGTH OF CONCRETE. Shock Compression of Condensed Matter–1991, Elsevier; 1992, pp. 501–4. doi:10.1016/B978-0-444-89732-9.50115-1.

[100] Lambert DE, Allen Ross C. Strain rate effects on dynamic fracture and strength. Int J Impact Eng 2000;24:985–98. doi:10.1016/S0734-743X(00)00027-0.

[101] Reinhardt HW, 1982. Concrete under Impact Loading, Tensile Strength and Bond. Heron 1982;27:1–48.

[102] Cadoni E, Albertini C, Solomos G. Analysis of the concrete behaviour in tension at high strain-rate by a modified Hopkinson bar in support of impact resistant structural design. J Phys IV France 2006;134:647–52. doi:10.1051/jp4:2006134100.

[103] Thomas RJ, Sorensen AD. Review of strain rate effects for UHPC in tension. Construction and Building Materials 2017;153:846–56. doi:10.1016/j.conbuildmat.2017.07.168.

[104] Dean AW, Heard WF, Loeffler CM, Martin BE, Nie X. A New Kolsky Bar Dynamic Spall Technique for Brittle Materials. J Dynamic Behavior Mater 2016;2:246–50. doi:10.1007/s40870-016-0062-6.

[105] Erzar B, Forquin P. An Experimental Method to Determine the Tensile Strength of Concrete at High Rates of Strain. Exp Mech 2009;50:941–55. doi:10.1007/s11340-009-9284-z.

[106] Klepaczko JR, Brara A. An experimental method for dynamic tensile testing of concrete by spalling. Int J Impact Eng 2001;25:387–409. doi:10.1016/S0734-743X(00)00050-6.

[107] Forquin P. On the Processing of Spalling Experiments. Part I: Identification of the Dynamic Tensile Strength of Concrete. J Dynamic Behavior Mater 2018;4:34–55. doi:10.1007/s40870-017-0135-1.

[108] Frew DJ, Forrestal MJ, Chen WW. A split Hopkinson pressure bar technique to determine compressive stress-strain data for rock materials. Exp Mech 2001;41:40–6. doi:10.1007/BF02323102.

[109] Ravichandran G, Subhash G. Critical Appraisal of Limiting Strain Rates for Compression Testing of Ceramics in a Split Hopkinson Pressure Bar. Journal of the American Ceramic Society 1994;77:263–7. doi:10.1111/j.1151-2916.1994.tb06987.x.

[110] Frew DJ, Forrestal MJ, Chen WW. Pulse shaping techniques for testing brittle materials with a split hopkinson pressure bar. Exp Mech 2002;42:93–106. doi:10.1007/BF02411056.

[111] Frew DJ, Forrestal MJ, Chen WW. Pulse shaping techniques for testing elastic-plastic materials with a split Hopkinson pressure bar. Exp Mech 2005;45:186–95. doi:10.1007/BF02428192.

[112] Heard WF, Martin BE, Nie X, Slawson TR, Basu PK. Annular Pulse Shaping Technique for Large-Diameter Kolsky Bar Experiments on Concrete. Exp Mech 2014;54:1343–54. doi:10.1007/s11340-014-9899-6.

[113] Xu M, Wille K. Numerical Investigation of the Effects of Pulse Shaper, Lateral Inertia, and Friction on the Calculated Strain-Rate Sensitivity of UHP-FRC Using a Split Hopkinson Pressure Bar. J Mater Civ Eng 2016;28:04016114. doi:10.1061/(ASCE)MT.1943-5533.0001580.

[114] Nie X, Chen WW. High-Rate Progressive Failure of Borosilicate Glass under Mechanical Confinement at High Temperatures. Exp Mech 2013;53:67–75. doi:10.1007/s11340-012-9635-z.

[115] Forrestal MJ, Wright TW, Chen WW. The effect of radial inertia on brittle samples during the split Hopkinson pressure bar test. Int J Impact Eng 2007;34:405–11. doi:10.1016/j.ijimpeng.2005.12.001.

[116] Chen X, Wu S, Zhou J. Experimental and modeling study of dynamic mechanical properties of cement paste, mortar and concrete. Construction and Building Materials 2013:419–30. doi:10.1016/j.conbuildmat.2013.05.063.

[117] Nemat-Nasser S, Isaacs JB, Starrett JE. Hopkinson Techniques for Dynamic Recovery Experiments. Proceedings of the Royal Society of London a: Mathematical, Physical and Engineering Sciences 1991;435:371–91. doi:10.1098/rspa.1991.0150.

[118] Gong JC, Malvern LE. Passively confined tests of axial dynamic compressive strength of concrete. Exp Mech 1990;30:55–9. doi:10.1007/BF02322703.

[119] Christensen RJ, Swanson SR, Brown WS. Split-Hopkinson-bar Tests on Rock under Confining Pressure. Exp Mech 1972;12:508–13. doi:10.1007/BF02320747.

[120] Lindholm US, Yeakley LM, Nagy A. The Dynamic Strength and Fracture Properties of Dresser Basalt. Int J Rock Mech Min Sci & Geomech Abstr 1974;11:181–91. doi:10.1016/0148-9062(74)90885-7.

[121] Frew DJ, Akers SA, Chen WW, Green ML. Development of a dynamic triaxial Kolsky bar. Meas Sci Technol 2010;21:105704. doi:10.1088/0957-0233/21/10/105704.

[122] Chojnacki JT, Chen WW. Mechanical Response of Borosilicate and Soda-Lime Glass Under Dynamic Triaxial Compression. J Dynamic Behavior Mater 2016;2:251–8. doi:10.1007/s40870-016-0063-5.

[123] Kabir ME, Chen WW. Measurement of specimen dimensions and dynamic pressure in dynamic triaxial experiments. Review of Scientific Instruments 2009. doi:10.1063/1.3271538.

[124] Kabir ME. Dynamic behavior of granular materials. Purdue, 2010.

[125] Kabir ME, Chen WW. Dynamic Triaxial Test on Sand. Society of Engineering Mechanics, New York, NY: Springer New York; 2011, pp. 7–8. doi:10.1007/978-1-4419-8228-5_2.

[126] Martin BE, Kabir ME, Chen WW. Undrained high-pressure and high strain-rate response of dry sand under triaxial loading. Int J Impact Eng 2013;54:51–63. doi:10.1016/j.ijimpeng.2012.10.008.

[127] Kabir ME, Chen WW, Kuokkala V-T. Measurement of Stresses and Strains in High Rate Triaxial Experiments, New York, NY: Springer New York; 2011, pp. 415–6. doi:10.1007/978-1-4419-8228-5_62.

[128] Chojnacki JT. Dynamic triaxial compression experiments on borosilicate and soda-lime glass. ProQuest, 2016.

[129] Hokka M, Black J, Tkalich D, Fourrmeau M, Kane A, Hoang NH, et al. Effects of strain rate and confining pressure on the compressive behavior of Kuru granite. Mechanics of Materials 2016. doi:10.1016/j.ijimpeng.2016.01.010.

[130] Mondal AB, Chen WW, Martin BE, Heard WF. Dynamic Triaxial Compression Experiments on Cor-Tuf Specimens. vol. 1, Springer International Publishing; 2013, pp. 245–9. doi:10.1007/978-3-319-00771-7_30.

[131] Chen WW, Song B. Split Hopkinson (Kolsky) bar. Springer; 2010.

[132] Chen R, Yao W, Lu F, Xia K. Evaluation of the Stress Equilibrium Condition in Axially Constrained Triaxial SHPB Tests. Exp Mech 2018:1–5. doi:10.1007/s11340-017-0344-5.

[133] Bulk Modulus and Fluid Elasticity - Kerosene. WwwEngineeringToolBoxcom n.d. https://www.engineeringtoolbox.com/bulk-modulus-elasticity-d_585.html (accessed April 30, 2020).

[134] Binder E, Reihsner R, Yuan Y, Mang HA, Pichler BLA. High-dynamic compressive and tensile strength of specimens made of cementitious materials. Cement and Concrete Research 2020;129:105890. doi:10.1016/j.cemconres.2019.105890.

[135] Zang ZX. Rock fracture and blasting 2016.